ADVISORY COMMITTEE

EDITORIAL BOARD

ARCHIVES
OF CIVIL AND MECHANICAL
ENGINEERING

Contents

Spis treści

Abrasive grains distribution in high-pressure abrasive-water jet used for surface treatment

P. BORKOWSKI

Koszalin University of Technology, Unconventional HydroJetting Technology Center, Raclawicka 15–17, 75-620 Koszalin, Poland

The paper presents properties and operational conditions for a high-pressure hydro-abrasive jet used for surface treatment. Methods of the assessment of abrasive grain distribution in such a high-pressure jet are discussed in. Basing on experiments and analytical consideration, dependences occurring between grain's traces distribution after hitting the surface and grains distribution inside such a jet were evaluated. Formulas derived on that let to calculate grains number and their distribution in a jet basing on their traces left inside the surface after single jet spray passage upon treated material. The present findings illustrate conditions necessary to form the hydro-abrasive jet with the most favourable distribution of abrasive grains conditioning the efficiency of surface treatment.

Keywords: *high-pressure abrasive-water jet, grains distribution, surface treatment*

1. Introduction

The abrasive-water jet cleaning finds its application almost to all fields of technology and economy. Such variety of abrasive-water jet applications requires also enormous diversification of its quality and configuration. Since the quality of the highly efficient fluid jet as an erosive tool is the decisive factor in selecting the conditions and parameters of such treatment and its efficiency [10, 11]. The steadiness in hydrodynamic parameters and properties of a high-pressure water jet is crucial from the viewpoint of surface cleaning stability. Especially, the structure of abrasive grains distribution is of great significance for efficient erosive treatment of work material [1, 17]. The practicability of the high-pressure abrasive-water jet is conditioned mainly on the method and conditions of shaping the water jet, its properties [3], flowing rate and methods for abrasive grains supplying and their doping as well [5, 7], because all the above exerts the fundamental effects on the performance of the cleaning process applied to work surface and the service life of elements of a sprinkler [6, 18].

The abrasive-water jet erosiveness depends mainly on the abrasive grains distribution in its cross section. Therefore, it is important to have knowledge of these relations. It creates the basis for the relevant studies on the structure of abrasive grains distribution in the cross section of the high-pressure abrasive-water jet.

2. Abrasive-water jet characteristic

Generally, the mechanism of deposits removal from the surface of work material using the high-pressure abrasive-water jet is very complicated [11]. This mechanism is commensurate with the one, which occurs while cutting materials with such jet [10, 12]. However, it should be taken into account that in the course of cutting using abrasive-water jet, only the front layer of the jet plays an active part. The most of it does not take part in the process of splitting the material but passively flows between the walls of the slot being cut. Due to this fact as much as 60–70% of energy is lost unproductively [16] in the process of cutting. On the other hand, the losses incurred by way of above occurring while surface treatment are significantly lower, because this process involves almost the whole cross-section of the abrasive-water jet.

It is important for the process understanding to analyze the effects of abrasive grains impinge on work material. The behaviour of the abrasive-water jet just from its outlet from the sprinkler should be taken into consideration as well. This device decides the usability of the abrasive-water jet for the treatment and therefore the constant progress in its design has been observed [14, 18]. To carry out the present own studies, the sprinkler of optimal design was applied where the abrasive-water jet in concentric multi-hole nozzle was created [7]. A schematic diagram of this sprinkler with the jet formed in it is illustrated in Figure 1. However, the correct configuration of the abrasive-water jet and the structure of abrasive grains distribution in this jet are of the greatest significance [4, 17].
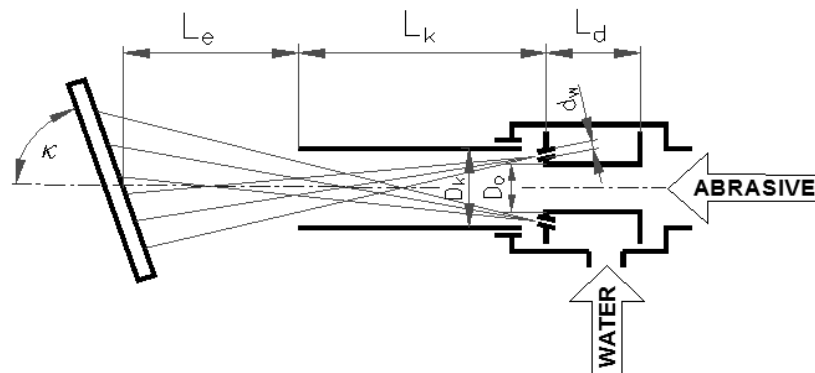
Fig. 1. Characteristic dimensions of the sprinkler and the abrasive-water jet

The distribution of abrasive grains plays a significant part for the properties of the abrasive-water jet. Since, depending on the structure of the abrasive grains distribution the erosive properties of the jet may undergo changes within the very wide range [13, 15]. The structure of such the distribution is determined by the number of abrasive grains in concentric annular layers of the jet. The number of these grains is determined by the number of their imprints left on the surface of work material [8, 17].

3. Abrasive grains distribution methodology

The abrasive grains distribution in the abrasive-water jet was determined indirectly by analysis of imprints made by the jet directed perpendicular to the surface of soft work material (plate made of lead, aluminium or copper). The grains being sprayed by the high-pressure jet impinging the surface of such plates leave imprints in this soft material. Assuming the uniformity of the grains distribution in individual conical layers of the jet [8, 17], it is possible to determine the number of abrasive grains in these layers on the basis of the number of their imprints. The assumptions for this method of determining the abrasive grains distribution are presented in Figure 2.

Calculating the density of imprints left on the surface of the plate impinged by the grains, let to evaluate their distribution in direction perpendicular to the jet flow. It was the basis to determine the intensity of abrasive grains distribution in individual conical layers of the abrasive-water jet. It allows the number of grains (n_k) in the respective k-th layer of the jet to be determined as the difference between the number of grain imprints (N_k) in the analogous field k on the surface of work material and the total number of grains occurring in these layers of the jet which had passed earlier over the considered field (k) of the specimen.

Respective geometrical quantities of such the imprint of the abrasive-water jet are shown on the right-hand side in Figure 2. Its lower part illustrates respective "horizontal" layers, i.e. parallel to the direction of imprint advance, while the upper part illustrates the surfaces of elementary "cells" of the jet and the radii of distribution of theses annular layers.
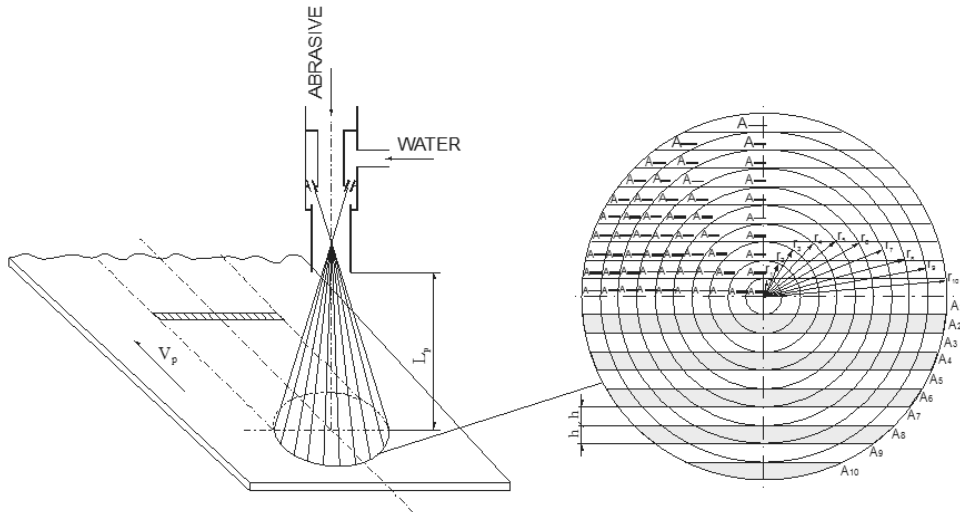
Fig. 2. Schema of methodic of abrasive grains distribution structure and elementary cells
situated in the abrasive-water jet also horizontal layers of treatment imprints

In order to determine the surfaces of respective "horizontal" layers of the jet and their elementary "cells", the following calculation procedure should be applied.

The surface of consecutive semi-layers presented in Figure 2 is described according to the expression in the following form:

$$A_i = \frac{r_m^2}{2} \frac{\pi}{90^o} \left\{ \left[arc\cos\frac{r_m - (m-i+1)h}{r_m} - arc\cos\frac{r_m - (m-i)h}{r_m} \right] + \right.$$
$$\left. - \left[\sin 2arc\cos\frac{r_m - (m-i+1)h}{r_m} - \sin 2arc\cos\frac{r_m - (m-i)h}{r_m} \right] \right\},$$

(1)

where:

m – number of annual conical coatings of the jet (radius $r_m = r_{10}$),

i – number of considered horizontal layer of the jet characterized by different coating dimensions.

The above equation is valid for each semi-layer including A_{10}, because then the second term of these equation shall be reset.

Next, the surface of mono-nominal, i.e. central elementary cells (here half-rounds) marked in the upper parts in Figure 2, is described according to the following relation in a generalized form:

$$A_{i.i} = \frac{r_i^2}{4} \left(\frac{\pi}{90^o} arc\cos\frac{r_i - h}{r_i} - \sin 2arc\cos\frac{r_i - h}{r_i} \right).$$

(2)

Whereas, the surface of multi-nominal elementary cells shown in Figure 2 is characterized with the following relations:

$$\left. \begin{aligned} & A_{10.9} = \frac{1}{2} A_9 - A_{99} \\ & A_{10.8} = \frac{1}{2} A_8 - (A_{99} + A_{98} + A_{88}) + A_{99} \\ & A_{9.8} = \frac{1}{2} A_8 - (A_{108} + A_{88}) \\ & A_{10.7} = \frac{1}{2} A_7 - (A_{97} + A_{87} + A_{77} + A_{98} + A_{88} + A_{99}) + (A_{98} + A_{88} + A_{99}) \\ & A_{9.7} = \cdots\cdots\cdots\cdots\cdots\cdots\cdots\cdots\cdots\cdots\cdots\cdots\cdots\cdots\cdots\cdots\cdots\cdots \\ & \cdots\cdots\cdots\cdots\cdots\cdots\cdots\cdots\cdots\cdots\cdots\cdots\cdots\cdots\cdots\cdots\cdots\cdots\cdots \end{aligned} \right\}.$$

(3)

Detailed notations of these equations, mostly in a very complicated form, were presented earlier [7, 9].

On the other hand, in order to determine the number of grains occurring in individual elementary cells of the jet, the following calculation procedure should be applied. In an external layer (A_{10} in area) the number of impinged grains imprints (N_{10}) responds to the number of grains (n_{10}), which specific intensity is equal to:

$$n_{j10} = \frac{n_{10}}{A_{10}} = \frac{N_{10}}{2A_{10,10}}.$$ (4)

The same intensity of impinged grains imprints occurs in the whole circular coating of the jet. Considering the above statement one can determine the number of grains occurring in individual "cells" of the external circular coating as equal to, respectively:

$$\left.\begin{array}{l} n_{10.10} = A_{10.10} \cdot n_{j10} = \dfrac{N_{10}}{2}\dfrac{A_{10.10}}{A_{10.10}} \\[2mm] n_{10.9} = A_{10.9} \cdot n_{j10} = \dfrac{N_{10}}{2}\dfrac{A_{10.9}}{A_{10.10}} \\[2mm] n_{10.8} = A_{10.8} \cdot n_{j10} = \dfrac{N_{10}}{2}\dfrac{A_{10.8}}{A_{10.10}} \\[2mm] \dots\dots\dots\dots\dots\dots\dots\dots\dots \\ \dots\dots\dots\dots\dots\dots\dots\dots\dots \\ n_{10.1} = A_{10.1} \cdot n_{j10} = \dfrac{N_{10}}{2}\dfrac{A_{10.1}}{A_{10.10}} \end{array}\right\}.$$ (5)

Similar procedure is applied to consecutive conical coatings of the abrasive-water jet and the layers, which includes the impinged grains imprints. It allows the number of grains occurring in respective elementary "cells" of the jet to be determined, as it was presented thoroughly earlier [2, 9]. At the same time, as the results of such calculations were increasing in number, the number of components representing the number of grains occurring in individual elementary "cells" subtracted from the total number of grain imprints was increasing as well. The most intensity of this calculation procedure was applied to the central "cell" of the jet core:

$$n_{1.1} = \frac{N_1}{2} - (n_{2.1} + n_{3.1} + n_{4.1} + n_{5.1} + n_{6.1} + n_{7.1} + n_{8.1} + n_{9.1} + n_{10.1}).$$ (6)

Considering above relations relative values of respective elementary "cells" of the jet trace can be define that are referred to their standard size $2.5 \times 2.5 = 6.25$ mm^2). Results of such calculations are illustrated in the form of spatial graph presented in Figure 3. As it is shown, cells presented in the central layers of the trace are close to standard value while outer ones (e.g. layer no. 10) are approximately three times larger.
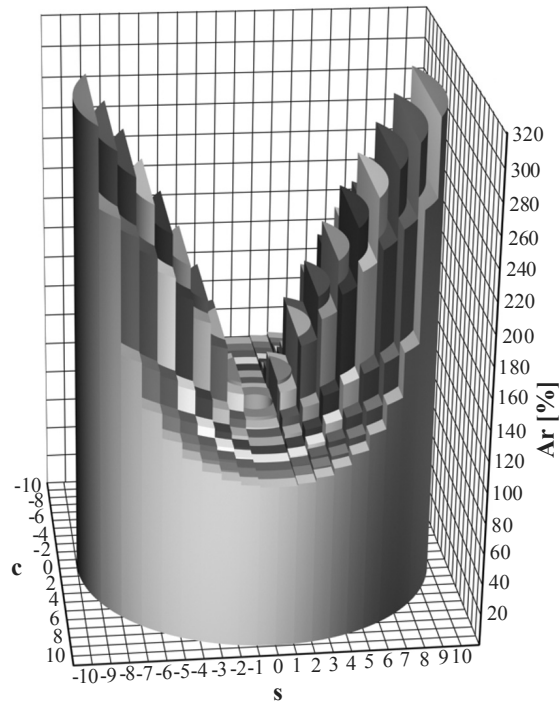
Fig. 3. Relative surface values of respective elementary "cells" of the jet trace

nr. kwadratu	Nk1	nk1	Nk2	nk2	Nk3	nk3	Nk4	nk4	Nk5	nk5	Nk6	nk6	Nk7	nk7	Nkśr.	nkśr.
-10	5	7	7	4	6	5	7	5	4	4	4	4	3	3	5	5
-9	11	6	11	8	12	7	13	7	13	6	11	9	12	7	12	7
-8	15	4	17	4	19	6	16	6	16	6	18	4	19	5	17	5
-7	23	6	26	8	22	7	27	9	28	7	25	8	24	9	25	8
-6	36	10	32	12	41	11	38	13	37	13	38	11	39	12	37	12
-5	38	7	42	9	50	8	49	9	47	8	46	7	45	9	45	8
-4	52	11	57	11	49	10	59	9	60	9	50	10	58	12	55	10
-3	67	14	74	16	70	15	74	18	69	17	75	15	69	17	71	16
-2	80	11	71	10	84	13	90	13	88	11	87	12	82	13	83	12
-1	87	8	94	9	100	10	93	10	99	12	89	11	90	12	93	10
1	89	10	93	9	97	10	101	6	95	10	94	9	91	11	94	9
2	85	9	88	10	70	12	91	11	84	14	87	14	88	13	85	12
3	63	14	68	14	76	16	83	15	82	15	74	17	65	14	73	15
4	50	10	57	10	59	10	58	11	63	12	62	15	57	12	58	11
5	47	10	42	11	52	11	54	10	50	8	43	9	41	11	47	10
6	36	9	30	12	41	13	40	13	38	12	31	13	41	10	37	12
7	22	10	21	11	26	9	25	7	29	10	28	8	25	9	25	9
8	15	5	14	4	16	5	15	3	18	4	18	6	17	7	16	5
9	10	7	10	6	9	7	13	7	13	8	12	7	11	8	11	7
10	2	1	3	4	5	6	4	5	4	6	5	5	5	3	4	4

Fig. 4a. The procedure of abrasive grains traces (N_k) distribution in the treated surface
and abrasive grains (n_k) in the abrasive-water jet (nozzle type TO 6 × 1.2 mm; $\varepsilon =$ 5º30′;
L_k = 200 mm; p = 20 MPa; SiO_2 #36) – experimental data

b)

c)

d)
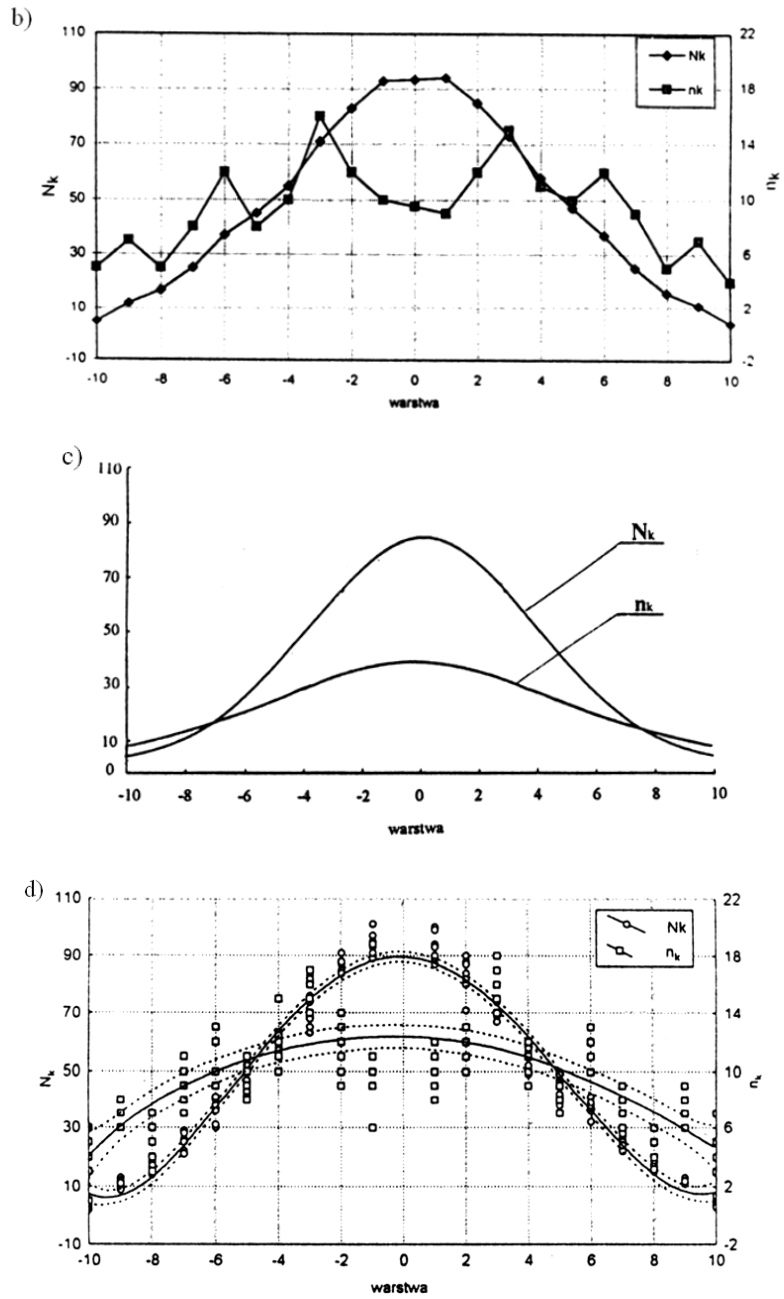

Fig. 4. The procedure of abrasive grains traces (N_k) distribution in the treated surface and abrasive grains (n_k) in the abrasive-water jet (nozzle type TO 6 × 1.2 mm; $\varepsilon = 5°30'$; $L_k = 200$ mm; $p = 20$ MPa; SiO_2 #36): b – average values distribution, c – statistic values distribution, d – normal values distribution

Examples of practical usage of model consideration for abrasive grains trace distribution estimation in a jet are presented basing on a series numerical results and consequently on their graphical illustrations shown in Figure 4.

Counting abrasive grains imprints (N_k) in respective elementary areas of the jet trace (left in soft lead material), the number of abrasive grains was calculated in respective concentric layers of abrasive-water jet cross-section. Such information is presented in the tabular form in Figure 4a. Basing on it, the mean values of grains traces ($\overline{N_k}$) and grains ($\overline{n_k}$) were calculated (Figure 4b) as well as empirical grain imprints ($\overline{N_k}$) and grains ($\overline{n_k}$) distributions was evaluated too (Figure 4c). As it turns out, irrespectively of above distribution polynomial description accuracy, such plot courses are normal distributions, what is shown in Figure 4d. Significantly different values of standard deviations speaks well of their distributions differences. Abrasive grains imprints distribution usually characterizes standard deviation at the level of at least 30 grains ($S_N = 30.4$) while regular grains distribution in a jet characterizes usually insignificant standard deviation at the level of $S_n = 3.31$.

4. Grains distribution in a jet

The abrasive grains distribution in high-pressure abrasive-water jet reflects the processes involved in mixing the abrasive grains with water jet, their accelerating connected with disintegrating [6, 16]. Such structures, especially the distribution of specific grain density in jet are the most important factors determining the suitability of the abrasive-water jet for surface treatment.

However in practice, beside the grain distribution in individual elementary "cells" of the jet, the knowledge of specific density of grain packing fractions (adequate to 1 mm^2) is also of great importance. Such the individual grain concentration is calculated as the number of grains included in "cells" in the central layer of the surface subject to treatment related to the surface of these "cells".

The plots of Figure 5 illustrate the typical examples of the abrasive grain distribution in individual elementary "cells" of high-pressure abrasive-water jet and the specific grain density distribution in conical coatings of this jet formed in the concentric nozzle with four water outlets arranged helically. It appears to be a clear indication that the elementary "cells" of central jet layer comprises relatively the smallest number of abrasive grains, whereas the external layers of jet includes several times more. It shall become obvious if one takes into consideration the much more extensive areas of these external "cells" at statistically homogeneous density of abrasive-grain concentration in the annular layer of abrasive-water jet. Then, the distribution of specific abrasive-grain concentration (Figure 5b) presented in the form of histogram of grain distribution is arranged according to the normal distribution marked with a full line.

In accordance with theoretical premises, the analogous distributions of abrasive grains in the abrasive-water jet obtained from a similar six-outlet nozzle (Figure 6) are

in a more concentrated form than before. Similar relations also take place in case of using the hydro-abrasive jet created in a similar eight-outlet nozzle (Figure 7).

a)

b)

Fig. 5. Distributions of: a – abrasive grains in particular elementary cells, b – unit concentration of abrasive grains in annual layers of abrasive-water jet, created in the sprinkler equipped with 4 outlet concentric nozzle type T0 4 × 1.2 mm, $\varepsilon_1 = \varepsilon_2 = 5°30'$, sprinkler tube no. 1, $p = 20$ MPa, abrasive material SiO_2 #36

a)

b)

Fig. 6. Distributions of: a – abrasive grains in particular elementary cells, b – unit concentration of abrasive grains in annual layers of abrasive-water jet, created in the sprinkler equipped with 6 outlet concentric nozzle type T0 6 × 1.2 mm, $\varepsilon_1 = \varepsilon_2 = 5°30'$, sprinkler tube no. 1, $p = 20$ MPa, abrasive material SiO_2 #36
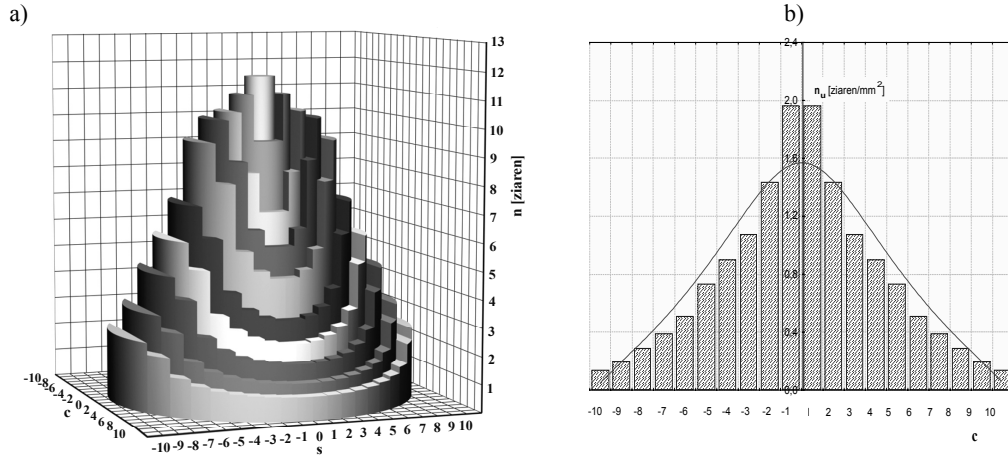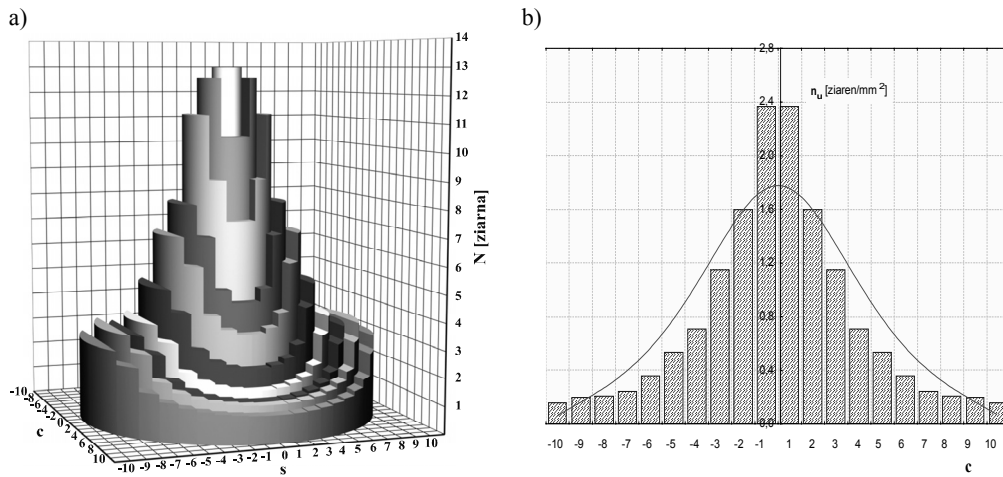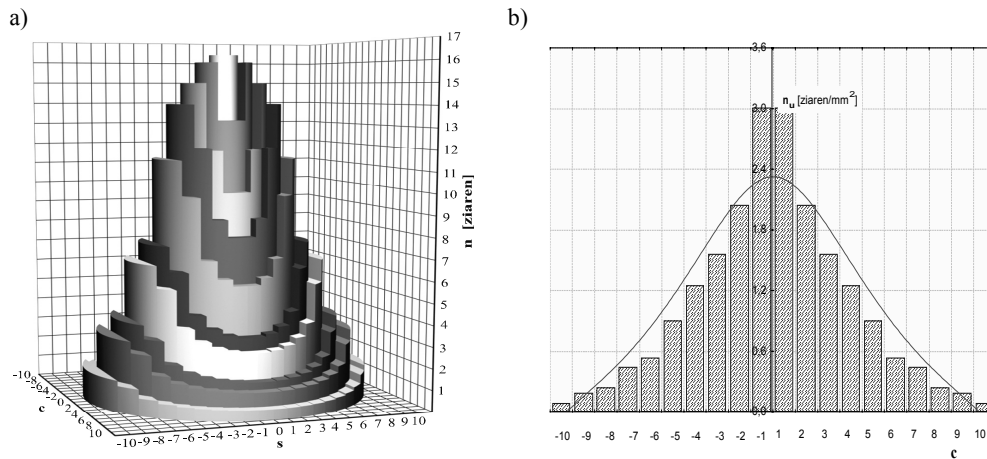
a)

b)

Fig. 7. Distributions of: a – abrasive grains in particular elementary cells, b – unit concentration
of abrasive grains in annual layers of abrasive-water jet, created in the sprinkler equipped
with 8 outlet concentric nozzle type T0 8×1.2 mm, $\varepsilon_1 = \varepsilon_2 = 5°30'$, sprinkler tube no. 1,
$p = 20$ MPa, abrasive material SiO_2 #36

It results from the plots being analyzed here that the highest concentration of abrasive grains occurs in the abrasive-water jet axis where the lowest total pressure prevails. While as the distance from the hydro-abrasive jet axis was increasing the flow rate of grains was decreasing. The smallest number of grains occurs in external layers of jet where the highest pressure prevails.

Thus, it is generally best to state that concentric jets with water outlets arranged helically play a significant part in forming the high-pressure abrasive-water jet. It allows the favourable structure of abrasive-grain distribution in the form of normal distribution to be obtained. It was also found that the most favourable, flattened grain distribution was obtained due to the application of sprinkles with a four-outlet nozzle. While the increased number of water outlets in a nozzle flange contributes to a usually highly expensive increase in abrasive-grain rate and is conductive to their higher concentration in jet and consequently makes it difficult to obtain the uniformly treated surface.

5. Summary

Experimental results obtained from the analysis of abrasive-grain distribution structure in the high-pressure abrasive-water jet allowed the following conclusions more general in character to be drawn:

• The sprinkler furnished with the concentric nozzle with water outlets arranged helically plays a very important part in forming the high-pressure abrasive-water jet providing the good surface-treatment properties.

- The abrasive-grain distribution structure in the jet formed in such the sprinkler is normal in character which is very favourable from the viewpoint of suitability of the abrasive-water jet as a tool for treating and cleaning the surface because this jet enables to obtain the uniformly treated surface at relatively high rate of surface treatment.

- The most favourable, flattened abrasive-grain distribution is obtained due to the application of the sprinkler with a four-outlet concentric nozzle. The increased number of water outlets in such the nozzle is usually conductive to the higher concentration of abrasive grains in jet and the abrasive grains rate, which involve the higher costs of surface treatment.

References

[1] Abudaka M., Crofton P.S.J.: *Theoretical analysis and preliminary experimental results for an abrasive water jet cutting head*, 5th American Water Jet Conference, Toronto, 1989, pp. 79–88.

[2] Borkowski P.: *Abrasive grains distribution in high-pressure abrasive-water jet used for surface treatment*, International Symposium on Unconventional HydroJetting Technologies, Koszalin, 2007, pp. 29–38.

[3] Borkowski P.: *High-pressure hybrid jet structure*, Journal of Jet Flow Engineering, Vol. 21, No. 3, 2004, pp. 11–15.

[4] Borkowski P.: *Properties of high-pressure hybrid jet for surface treatment*, 17th International Conference on Water Jetting, Mainz, 2004, pp. 161–169.

[5] Borkowski P.: *Physical basis of high-pressure hybrid water-abrasive-ice jet application for surface treatment*, 2003 WJTA American Waterjet Conference, Houston, 2003, Paper 4-A, pp. 15.

[6] Borkowski P.: *Fundamentals of surface treatment with high-pressure abrasive-water jet*, 7th Pacific Rim International Conference on Water Jetting Technology, Jeju, 2003, pp. 321–330.

[7] Borkowski P.: *Obróbka powierzchni wysokociśnieniową strugą wodno-ścierną*, Centrum Technik Proekologicznych, Koszalin, 2002.

[8] Borkowski P.: *Rozkład ziaren ściernych w strudze wodno-ściernej kreowanej w tryskaczu z koncentryczną dyszą wielootworową*, XXIII Naukowa Szkoła Obróbki Ściernej: Obróbka ścierna. Podstawy i technika, Rzeszów, 2000, pp. 503–510.

[9] Borkowski P., Mazurkiewicz M.: *Abrasive grains distribution in high-pressure hydro-abrasive jet used for surface treatment*, Advances in Manufacturing Science and Technology, Vol. 28, No. 2, 2004, pp. 61–70.

[10] Capello E., Groppetti R.: *On an energetic semi-empirical model of hydro-abrasive jet material removal mechanism for control and optimization*, 11th Int. Symp. Jet Cutting Technology, Proc. Kluwer Academic Publ., Dordrecht–Boston–London, 1992, pp.101–120.

[11] Faber K., Oweinah H.: *Influence of process parameters on blasting performance with the abrasive-jet*, 10th Int. Symp. Jet Cutting Technology, Proc. Elsevier Sci. Publ. London-New York, Chapter 25, 1991, pp. 365–38.

[12] Hashish M.: *On the modelling of abrasive-waterjet cutting*, 7th Int. Symp. Jet Cutting Technology, Ottawa, Paper E1, 1984, pp. 249–265.

[13] Isobe T., Yoshida H., Nishi K.: *Distribution of abrasive particles in abrasive water jet and acceleration mechanism*, 9th Int. Symp. on Jet Cutting Technology, Sendai, Paper E2, 1988, pp. 217–238.

[14] Liu B.: *The rotated injection abrasive jet rust cleaning system*, 10th Int. Symp. Jet Cutting Technology, Proc. Elsevier Sci. Publ. Ltd., London–New York, Chapter 14, 1991, pp. 221–233.

[15] Mazurkiewicz M.: *Material removal by hydro-abrasive high-pressure jet mechanism study*, SME Conf.: Non-Traditional Machining, Orlando, Paper MS89-811, 1989, pp. 15.

[16] Mazurkiewicz M.: *Single abrasive particle and high pressure hydro-abrasive jet performance study*, 1989 SME Int. Conference and Exposition, Detroit, Paper MR89-442, 1989, pp. 15.

[17] Mazurkiewicz M., Olko P., Jordan R.: *Abrasive particle distribution in a high pressure hydroabrasive jet*, Int Waterjet Symp Beijing, 1987, pp. 4.1–10.

[18] Takei M., Hashimoto B., Hori K., Kataoka I., Ito H., Yoshida H., Kim T.J.: *Performance evaluation of spiral water jet cutting system*, 12th Int. Symp. Jet Cutting Technology, Rouen, 1994, pp. 16.

Rozkłady ziaren ściernych w wysokociśnieniowej strudze wodno-ściernej używanej do obróbki powierzchni

W artykule omówiono właściwości oraz uwarunkowania pracy wysokociśnieniowej strugi wodno-ściernej stosowanej do obróbki powierzchni. Zaprezentowano metodykę oceny rozmieszczenia ziaren ściernych wewnątrz takiej wysokociśnieniowej strugi. Na podstawie eksperymentów i rozważań analitycznych określono zależności występujące pomiędzy rozkładami śladów uderzeń ziaren o powierzchnię obrabianą a rozmieszczeniem ziaren wewnątrz takiej strugi wodno-ściernej. Wyprowadzone wzory pozwalają na obliczenie zawartości i rozkładów ziaren ściernych w takiej strudze na podstawie analizy śladu pozostawianego po jej jednorazowym natrysku na powierzchnię obrabianego materiału. Przedstawione wyniki badań ilustrują warunki tworzenia strugi wodno-ściernej o najkorzystniejszych rozkładach cząstek ściernych, determinujących skuteczność operacji obróbki powierzchniowej.

Methods of risk evaluation in manufacturing systems

A. BURDUK, E. CHLEBUS

Wrocław University of Technology, Wybrzeże Wyspiańskiego 25, 50-370 Wrocław, Poland

The production system was defined with regard to system theory. The risk concept was treated as synonym of unreliability. This kind of approach enabled decomposition of the production system into several areas and determination of reliability structure. The paper presents method of the risk value evaluation for serial-production structures and conceptions of weight coefficients in the method. The proposed method of risk evaluation may be helpful to determine the risk level in chosen production line and eventually for the whole enterprise manufacturing systems. The method was verified in a production enterprise, where there are manufacture cart frame for wagons, carriages and engines.

Keywords: *production system, simulation model, risk evaluation*

1. "Risk" term characteristic

Environment and enterprises themselves become more and more dynamic and complex. Consequently all necessary decisions are made under higher uncertainty and risk. The decisions influence the company's situation not only at the moment they are made but also have an effect on the future. Hence each decision which is significant for enterprise operations have to be preceded by analysis, planning and risk evaluation.

Although the risk of economic activities is equally high on production, service and financial market, there is a difference in the amount of literature, trainings and scientific conferences as far as each of those areas are concerned. That situation results in poorly developed methods of planning, analysis and risk evaluation in the production area, where planning and assessment of risk is considered as unimportant. On the other hand there are plenty of materials on management, analysis and assessment of credit, insurance, trade, information risk.

Risk term ambiguity and lack of a consistent definition is a reason why in the literature can be found different approaches to this concept. However, the most popular are German and American approach.

The German approach limits the term of "risk" to gaining a negative outcome of the decision which was made and treats risk as "the danger of unfulfilled aim assigned at the moment of making the decision" [1]. The unfulfilled aim means losses as well as a result which is smaller than the assigned. In this paper there is used a German approach. The American approach is wider than the German as it treats the concept of risk not only in terms of losses but also possible profit. Figure 1 presents the both of them.
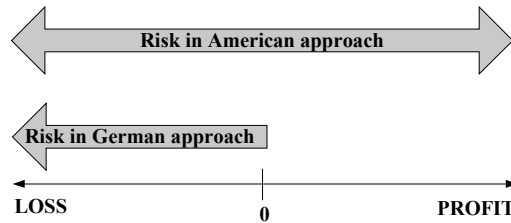
Fig. 1. The concept of risk according to American and German approaches

Large number of risk's concepts makes that in the literature can be found various definitions of risk. Risk can be understood and determined as [1]0, [7]: possibility and probability of loss, discrepancy between real and required result, probability of result different then required, possibility of unrequired events, conditions, at which there is a possibility of loss, uncertainty, danger, possibility of missing a target.

As risk is a common phenomenon it occurs in all areas of life and reveals interdisciplinary character. There are number of scientific disciplines that deal with risk analysis, e.g. probability calculus, statistics, econometrics, image recognition theory, reliability theory, operational research, theory of organization and management, psychology, sociology, philosophy, etc.

2. Quantitative methods of analysis and risk evaluation

In literature there is mentioned a lot of methods designed for analysis and evaluation of risk in an enterprise. As it was mentioned in the previous part of the paper, risk is defined in various ways and appears in different economic areas, and consequently methods of risk assessment are rooted in a variety of scientific disciplines. Authors of publications classify individual methods of analysis and risk evaluation in different way (compare [1]0, [7]), however, two classes are mentioned the most often:

1. Class of verbal methods, called also descriptive or general, which allow to get acquainted with the nature of appearing risk in organization for example: operational level methods, descriptive risk evaluation, profile analysis, early warning systems, and risk compensation methods.

2. Class of quantitative methods, which make use of numerical data and allow estimate the magnitude of risk, for example: strategic level methods, operational methods, financial methods.

As production process management is considered as an operational issue and its control requires making use of detailed numerical data, the subject of further analysis will be only quantitative methods of operational level. Generally, on the operational level there can be applied statistical and operational research methods. Figure 2 shows all groups of quantitative methods for analysis and risk evaluation with a special consideration of operational level methods.
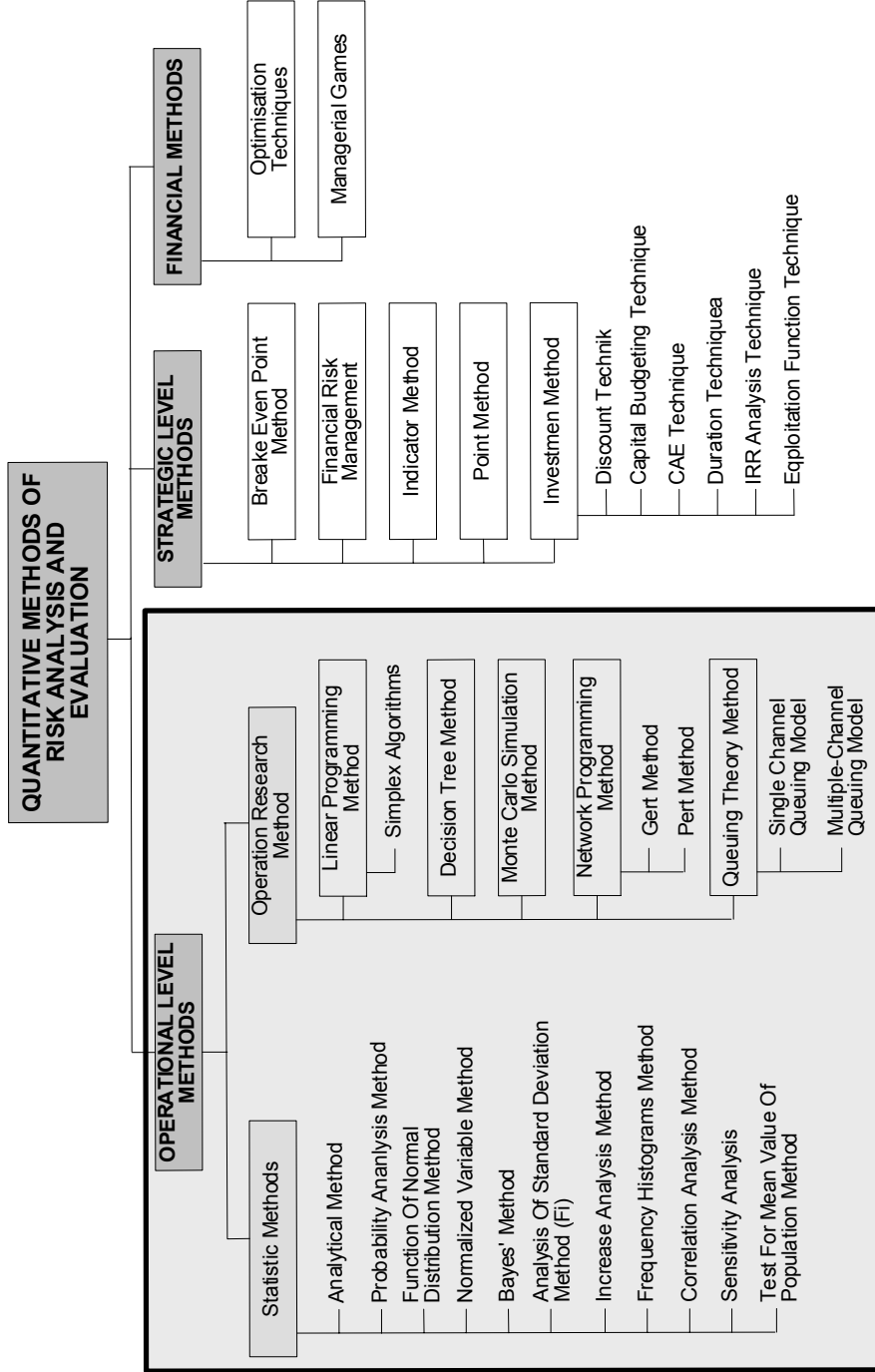
Fig. 1. Quantitative methods of risk analysis and evaluation

Proposed in literature quantitative methods of risk analysis and evaluation treat single issues, assuming certain factors and conditions as well as impose constraints. Hence in order to asses risk of production process in its real environment, the problem should be simplified and adjust to a certain method. Taking into consideration the complexity of modern production systems as well as a number of influencing them external, random factors, this kind of approach seems to be unsuitable. Results of such analysis may contain a considerable mistake.

Table 1 presents the comparison of the most popular quantitative methods of risk analysis and evaluation. Comparative criteria were chosen in a way to show usefulness of the methods in practical problems solving.

Table 1. Comparison of quantitative methods of risk analysis and evaluation

METHOD	KNOWLEADGE ON DISTRIBUTION	NUMBER OF INPUT DATA	SEQUENCY	GRAPHIC METHOD?	COMPLICATED?
STATISTIC METHODS					
Analytical method	○	○	○	◉	○
Probability analysis method	○	◉	○	◉	○
Function of normal distribution method	●	○	○	◉	○
Normalized variable method	●	○	○	◉	○
Bayes' method	○	◉	○	○	◉
Analysis of standard deviation method (fi)	○	◉	○	○	○
Increase analysis method	○	◉	○	◉	◉
Frequency histograms method	○	○	○	●	○
Correlation analysis method	○	◉	○	◉	◉
Sensitivity analysis	○	○	○	○	○
Test for mean value of population method	◉	○	○	◉	◉
Operation research methods					
Simplex algorithms	○	●	●	◉	●
Decision tree method	○	◉	◉	●	○
Monte carlo simulation method	●	●	●	○	●
Gert method	●	●	●	●	●
Pert method	●	●	●	●	●
Queuing theory method	○	○	○	○	●
LEGEND					
● – many/yes	◉ – average/some		○ – few/no		

Following the comparison presented in Table 1 it is essential to adjust the above methods to current level of techniques and technologies development in production processes.

3. Production systems reliability

Implementation of reliability theory to production systems could result in many advantages for planning and risk evaluation in production systems. However this action requires definition of certain approaches to production process as well as reliability.

Reliability theory considers in principle 0/1 states, which means operation or lack of operation. This approach considers technical objects but unfortunately it is inappropriate to represent biotechnical objects, exploitation systems as well as production systems (processes). This inability resulted in foundation of "general reliability method" concept which can be found in [1], [5].

Peculiarity of modern production systems and especially their complexity let treat them as exploitation systems so then reliability is one of their feature and is measured as a degree of realization assigned indicators, parameters and characteristics. On the other hand production systems have to operate in environment which all the time influence the system and generates disturbances. This makes reliability to reveal a random nature in real conditions.

The reliability of production systems can be evaluated in a very flexible way assuming that, depending on analysis purpose, "operations following subject's intentions" are a value of any indicator characterizing the process, according to the subject. The most often analysed indicators of production process are process duration (t), efficiency (W), productivity (P) [5]:

The probability that the analysed parameter is not smaller than the planned one, that is production process reliability, can be calculated similarly, as follows [5]:

$$N = P(t_{pl} \leq t_{rz}), \tag{1}$$

$$N = P(W_{pl} \leq W_{rz}), \tag{2}$$

$$N = P(P_{pl} \leq P_{rz}), \tag{3}$$

where:

W_{pl} – planned value of analysed indicator,
W_{rzecz} – real value of analysed indicator.

3.1. Relationship between reliability and risk

The issue of the reliability is traditionally connected with operations and functioning of technical objects and this term very rarely relates to an economic systems. In economic literature, on the other hand, there is a great interest in the idea of risk. As according to the system theory both technical as well as economic objects can be treaded like a system, it seems to be justified to transfer the general reliability theory

and its application in risk planning and evaluation to the area of the economy. Especially susceptible to this transfer seems to be production systems for which the specific technology makes it impossible to treat the risk according to the American approach. The risk in this kind of systems can be considered only as a possibility of gaining effects (profits) smaller than the expected (so-called the German approach).

The transfer of the general reliability theory into the area of production systems can be accomplished if unreliability (Z) – the reliability opposition – is treated as a synonym of the risk (R) [1]:

$$R = Z. \tag{4}$$

The risk (unreliability) of the system (e.g. production system) interpreted in that way is a probability of the situation that the system will be unable to fulfil its functions, for which it was designed, or it will represent the probability of losses in that system. For this interpretation the following equation should be valid:

$$N + Z = 1. \tag{5}$$

The above equation represents that the probability of a situation when the system is reliable or unreliable is equal to 1. For this reason it is also true, that:

$$R = N - 1. \tag{6}$$

Hence the risk analysis and evaluation will allow to specify unreliability of system functioning and inversely. Unreliable approach to risk planning and evaluation, although it delivers more possibilities, does not locate risk factors in a system. Thus in the process of risk evaluation it is necessary to take into consideration the unreliability structure of the production system.

3.2. Reliability structure of the system

The unreliability (risk) or reliability of the system is also influenced by its structure. Because the considered system can be a simple or a complex composition, its reliability is influenced by the reliability structure determining the connection of the system reliability state with the system's objects reliability state.

Depending on relations and feedbacks between objects in the system (also production systems) there can be distinguished various kinds of structures. The way in which the individual objects of the systems function operate and are controlled is highly dependent on the structure type. Analysis of the reliable structure of the system should be carried out through the system separation into individual components, which is called – system decomposition. The result of the system decomposition should be extraction of statistically independent and possibly the biggest elements representing logical relationships in the system [1]. Depending on the type of the feedback relations

between the system objects there can be pointed out three generic reliability structures: serial, parallel and serial-parallel [1].

As in the later part of the article there will be presented a method of risk evaluation for real production system being an example of the serial structure, only this type of the reliability structure will be elaborated.

4. Method of risk evaluation in serial structure production systems

The system reveals the serial structure if for its proper operations functioning of all its objects/areas of production system is required. It means that the system operates correctly only if all its components also operate correctly and in the case any object/ areas of production system breakdowns the whole system collapses as well [1], [6]. As far as the serial structure is concerned the relationship between two objects/areas of production system consists in transformation of the output vector of the first object/ areas of production system into the input vector of the second object/areas of production system. However it is not required all components of the output vector of the first object/ areas of production system become the components of the input vector of the second object/ areas of production system. The example of the serial reliability structure for n objects is presented in Figure 3.
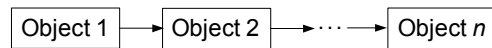

Fig. 2. The example of the serial reliability structure for n areas

For this kind of structures the system reliability is a product of reliability of all system's objects. Hence along with the increase of the number of objects within the system the reliability of the whole system decreases.

The reliability of the system revealing the serial structure (N_S) is described as [6]:

$$N_S = N_1 N_2 \ldots N_n,$$ (7)

where:
N_1, N_2, N_S – reliability of individual system's objects.
Using Equations (6) and (7) the total risk (R_C) of the system will be equal to:

$$R_C = 1 - [(1 - R_1)(1 - R_2)\ldots(1 - R_n)],$$ (8)

where:
R_1, R_2, R_S – the risk individual areas of production system/objects of the system.
For individual areas the risk (R_i) is calculated as follows:

$$R_1 = \frac{S_1}{W_{\text{theoret}}}, \quad R_2 = \frac{S_2}{W_{\text{theoret}} - S_1}, \quad R_n = \frac{S_n}{W_{\text{theoret}} - S_1 - \ldots - S_{n-1}},$$ (9)

where:

S_i – determines the loss in an i object due to risk factors r_i appearing in that object,

W_{theoret} – specifies a certain level of analyzed in the production system indicator (e.g. productivity) which value is theoretically possible to reach in the production system.

The losses S_i in particular objects are dependent on time losses made by time of production processes extension due to risk factors present in those areas. In other words, the production system will reach the defined target however more time will be required in order to fulfil all requirements. Then the losses in a measurable target in the production system, caused by risk fractions in particular areas, can be presented as follows:

$$S_n = W_{\text{theoret}} \frac{\Delta t_n}{T},$$ (10)

where:

Δt_i – time losses in particular areas caused by risk factors,

T – describes unit of time or period, for which there was determined realization of the target by the production system.

Hence, the total risk R_C of the system consisting of n areas and revealing the serial structure will be equal to:

$$R_c = 1 - \left[\left(1 - \frac{\Delta t_1}{T} \right) \left(1 - \frac{\Delta t_2}{T - \Delta t_1} \right) \cdots \left(1 - \frac{\Delta t_n}{T - \Delta t_1 - \ldots - \Delta t_{n-1}} \right) \right].$$ (11)

5. Consideration of weight coefficients in the method

The described above risk evaluation method for production systems revealing the serial structure can be used to determine risk in individual areas of production system as well as in the whole production system.

Sometimes the production process organisation can cause that the evaluated magnitude of risk is not adequate to real size of disturbances in the production system, however. An example can be a delay of elements delivery that is the risk factor, which on the other hand is decreased by warehouse inventory. Thus the real impact of the delivery delay on the production system is smaller than it follows the registered delivery times. Hence, it is proposed to apply to the method of risk evaluation the weight coefficients, the construction of which enables the assessment of the real risk level in the system.

The application of the weight coefficients gives also the opportunity to determine in what way the organizational change introduced to the production system will influence a decrease of the system risk level. For instance there can be estimated for what

security inventory level the risk level will be satisfactory reduced. There is proposed the following construction of the weight coefficient:

$$w_i = \frac{\Delta t_i^r}{\Delta t_i}, \tag{12}$$

where:

Δt_i^r – the real time of production process lengthen made by appearance of i risk factor,

Δt_i – time losses in particular areas of production system made by risk factors.

This kind of weight construction declines the risk size for areas where the production process organization reduces the influence of the real level of disturbances. Thus the presented above equation of total risk in the system revealing the serial structure will be as follows:

$$R_C = 1 - \left[\left(1 - \frac{\Delta t_1}{T} w_1 \right) \left(1 - \frac{\Delta t_2}{T - \Delta t_1 w_1} w_2 \right) ... \left(1 - \frac{\Delta t_n}{T - \Delta t_1 w_1 - ... - \Delta t_{n-1} w_{n-1}} w_n \right) \right]. \tag{13}$$

6. Overview of manufacturing system

Described company manufactures freight and passenger trains as well as complete transportation systems. Wroclaw plant of the company consists of three divisions: Locomotives, Bogies, Service. The project presented in this paper was conducted in Bogies Division, where bogies frames for locomotives and for passenger trains are produced.

Manufacturing of individual frame types is executed on separated production lines. With respect to specialised tooling and sizes of assembly stands, retooling of the line is a very time-consuming process. The manufacturing process is mainly composed of welding operations of individual components that make the product structure.

Production is controlled by the so-called kits, i.e. ready sets of components supplied from the warehouse to separate places in the production shop. The number of kits differs, depending on a product complexity level. Material flow in the production shop is performed by overhead cranes and outside the shop – by trucks. During the manufacturing process, the components are several times taken away from the shop to be subjected to external operations at subcontractors and for quality inspection.

The program of the company reorganisation and adaptation requirements required switching from bogie production to bogie frame production and increasing the production capacities. A complex analysis of the problem was necessary with the use of computer tools, especially software for computer simulation and optimisation of manufacturing systems.

6.1. The background of the test case and the problem to be solved

Hence to meet the required production capacity the company had to expand the plant, build additional new production lines, optimise the layout and machine stock, as well as evaluate risk of production program. As the large quantity of date had to be analysed the project was conducted in the following stages 0:

1. Building the production line layout model for a selected product and its optimisation with respect to length of transport routes and productivities. For analysis, a representative product and production volume was defined as 400 pieces.

2. Building the layout model and its optimisation with respect to length of transport routes considering total material flow inside and outside the plant. This stage was performed using conversion factors calculated on the ground of technological probability of products and labour consumption compared to the product analysed in stage 1.

3. Determination the risk and reliability of the production program realisation for individual products. The stages 1 and 2 included the technological and organisational data only, so the real risk factors existing on production lines with their occurrence probability were used to determine the risk and reliability.

In the paper were presented only chosen results of 1 and 3 stage of the project.

6.2. Results of stage 1

The research involved building several versions of layout models for the selected product (using ProModel 2002 simulation package), their simulations and analysis of the obtained results. In all models, the following was considered: position of construction supports, real dimensions of the production shop and workplaces.

Analyses of the simulation results made it possible to determine, among others, a complete frame production time with the attainable productivities and the flow time for the first piece of the new product. Results of the analysis also permitted determination of loads of the work-stands that appeared to be bottlenecks precluding fulfilment of the sales plan. In order to carry out the sales plan, it was necessary to reach the assumed productivity of 1 piece of product per shift, and twice as much for the parts of the product structure, i.e. 2 pieces per shift. Productivity of eight work-stands of the seventeen ones present in the line was high enough. Simulation of the production line revealed also the problem of too long and crossing transport routes in the production shop and too low capacity factor of overhead cranes belonging to the vertical transport.

To eliminate the bottlenecks, organisational changes were suggested, consisting of different assignment of operations to work-stands, introduction of a third shift, employing of a new worker or purchase of one more work-stand, depending of the expected investment costs. New distribution of operations between the work-stands was also introduced and quality inspection was removed from the stand in the main production line. The productivity comparison of selected workplaces before and after changes is shown on Figure 4.
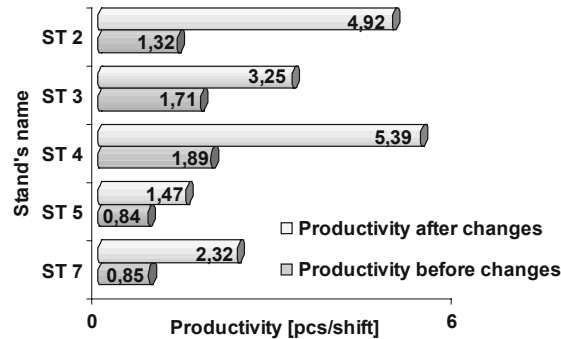
Fig. 4. The productivity of selected workstations before and after changes [3]

6.3. Results of stage 3

The objective of this stage was to determine the influence degree of individual risk factors on selected parameters of the production process.

7 simulation models were used for risk evaluation. Each of the subsequent models was built by introducing next risk factors to the base model, with their probability of occurrence. This was aimed at demonstration of growing effect of disturbances on the production process. The following models for risk evaluation were created:

1. Base model – that considers the suggested changes accepted in the stage 1 of the project but does not include any risk factors;

2. DB model – for analysis of disturbances caused by specific customer's requirements;

3. Delivery model – that includes real delays and shortages of the sheets deliveries;

4. Co-operation model – that analyses risk factors for missing deliveries and defective components from co-operating parties;

5. Production model – with real operation times (different from the technological times);

6. Failure model – with statistical down-times of the production line caused by the equipment failures;

7. QI model – that considers statistical production rejects and technological times of their correction, as well as the risk related to planning of quality inspection;

Losses of time (Δt_i) in individual models caused by risk factors are shown in Figure 5.

Using Equation (10) we may calculate losses in individual areas of production system (simulation models) that are caused by risk factors appearing in those areas. Those losses for $W_{theoret} = 138$ pieces per 12 weeks and are shown in Table 2.

Table 2. The losses in individual models [pieces per 12 weeks]

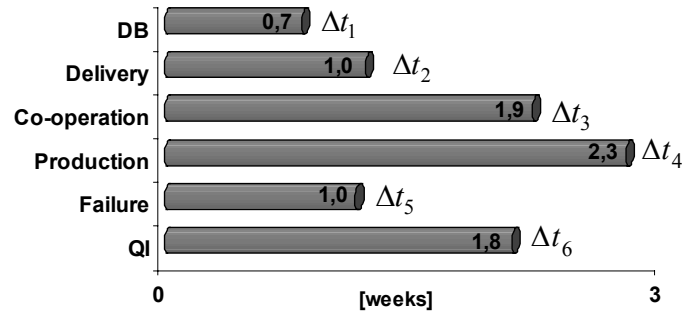| S_1	S_2	S_3	S_4	S_5	S_6
8.05	11.5	21.85	26.45	11.5	20.7

Fig. 5. Losses of time in individual models

For known quantity of losses in individual areas of production system there can be calculated the quantity of risk in individual areas of this production system (the Equation (9)).

The individual areas the risk R_i is calculated and shown in Table 3.

Table 3. The risk individual areas of analysed production system

R_1	R_2	R_3	R_4	R_5	R_6
0.06	0.09	0.18	0.27	0.16	0.35

In the next step, using Equation (11), the total risk (R_C) for the representative product in the analyzed production system can be calculated – $R_c = 0.73$.

The received value of the total risk (R_C) means that with the probability of 0.73 it is not possible to reach the determined goal in the production system, which is production of 138 pieces per 12 weeks. Figure 6 presents the increases of risk's level in individual simulations models. The level of the risk regarding the QI model is equivalent with the total risk (R_C) of the whole production system, as it includes all risk factors.
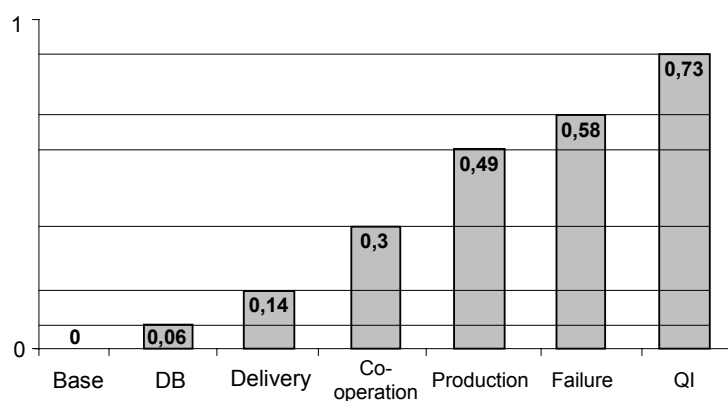

Fig. 3. The increases of risk's level in individual simulations models

The risk's increases analyzed in simulation models prove that the highest increase of risk is caused by risk factors appearing in production, co-operation and quality control areas.

In order to minimize the total risk level (R_C) it is advisable to undertake the effort of the risk reduction in the mentioned above three areas.

The application of the weight coefficients in the described method delivers the possibility to determine the real level of the risk in the system independently from the organizational level of the production system.

The analysed industrial enterprise keeps the security stock of metal sheets and components which covers 3 days of production. Hence the change of time Δt_i for the area of the metal sheets delivery as well as cooperation is as follows:
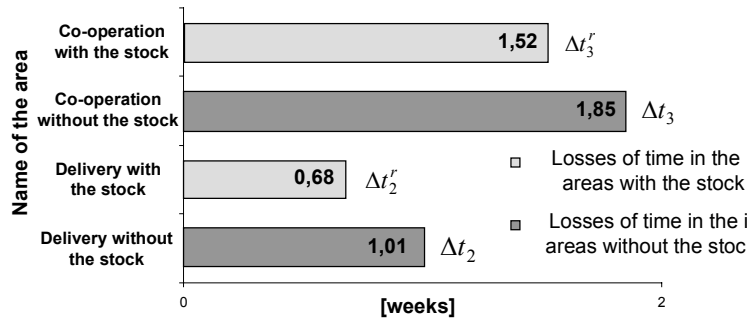

Fig. 7. Variation of time in selected areas of the production system with and without the security stock 0

Figure 7 presents only areas of the production system for which the organizational changes were applied. In other areas Δt_i are as in the Figure 7. The time changes in the areas with the security stocks, specified as Δt_2^r and Δt_3^r, determine the real extension time of the production process. Those periods are proportionally shorter because the security stock decreases the negative influence of risk factors in these areas.

Taking into consideration the data presented in Figure 7 there can be calculated values of the weight coefficients in the area of metal sheet delivery and cooperation according to Equation (12):

$$w_2 = \frac{\Delta t_2^r}{\Delta t_2} = 0.67 \text{ , and } w_3 = \frac{\Delta t_3^r}{\Delta t_3} = 0.82.$$

The values of both weight coefficients can be used in Equation (13). The total risk R_C for the representative product is equal to:

$$R_c = 1 - \left[\left(1 - \frac{\Delta t_1}{T} w_1 \right) \left(1 - \frac{\Delta t_2}{T - \Delta t_1 w_1} w_2 \right) \dots \left(1 - \frac{\Delta t_n}{T - \Delta t_1 w_1 - \dots - \Delta t_{n-1} w_{n-1}} w_n \right) \right] = 0.69$$

According to the above calculations the implementation into the production system the security stock that covers 3 days production decrease the risk level of the representative product by 0.04.

References

[1] Bizon-Górecka J.: *Engineering of reliability and risk in enterprise management* [in Polish], Printing House of the Organisation Development Centre, Bydgoszcz, 2001.
[2] Bubnicki Z.: *The basics of computer systems management* [in Polish], Printing House of the Wroclaw University of Technology, Wroclaw, 1993.
[3] Burduk A.: *Methodology for applications of simulation models in planning and risk evaluation of production processes realization* [in Polish], PhD thesis, Wroclaw, 2004.
[4] Drucker P.F.: *The emergency theory of manufacturing*, Harvard Business Review, No. 3, 1990.
[5] Durlik I.: *Engineering of management. Strategy and design of production systems* [in Polish], Printing House Placet, Warszawa, 1995.
[6] Migdalski J.: *Reliability engineering* [in Polish], Printing House ZETOM, Warszawa, 1992.
[7] Ostrowska E.: *Risk of investment projects* [in Polish], PWE, Warszawa, 2002.
[8] Wilimowska Z., Wilimowski M.: *Art of finance management* [in Polish], Printing House of Organisation Development Centre, Bydgoszcz, 2001.

Metody wyznaczania ryzyka w systemach produkcyjnych

W artykule zdefiniowano system produkcyjny zgodnie z teorią systemów, natomiast ryzyko potraktowano jako synonim zawodności. Takie podejście umożliwiło dekompozycję systemu produkcyjnego na obszary i wyznaczenie struktury niezawodnościowej. W artykule przedstawiono metodę wyznaczania ryzyka dla szeregowej struktury produkcyjnej i koncepcję współczynników wagowych uniezależniających poziom ryzyka od poziomu organizacyjnego systemu produkcyjnego. Proponowana metoda wyznaczania ryzyka może być stosowana zarówno przy obliczaniu ryzyka poszczególnych linii produkcyjnych, jak i dla całego przedsiębiorstwa. Metoda została zweryfikowana w przedsiębiorstwie produkującym ramy wózków do wagonów kolejowych i lokomotyw.

Spectral density of the bridge beam response with uncertain parameters under a random train of moving forces

M. GŁADYSZ, P. ŚNIADY

Wroclaw University of Technology, Wybrzeże Wyspiańskiego 27, 50-370 Wrocław, Poland

The paper presents the spectral analysis of the beam's vibration with uncertain parameters under a random train of moving forces which forms a filtered Poisson process. It is assumed that natural frequencies of the bridge beam are uncertain and are modelled by fuzzy numbers, random variables or fuzzy random variables. In order to obtain general solutions for the spectral density function of the beam's response the normal mode dynamic influence function has been introduced. As an example the spectral density functions of a bridge modelled as a simple supported beam are determined.

Keywords: *vibration, random moving forces, Poisson process, spectral analysis, uncertain parameters*

1. Introduction

Many authors have considered the problem of vibrations in structural engineering, resulting from the moving load, because it has a significant importance for practice, for example in bridge designing and also is interesting from theoretical point of view. Vibrations of that kind have been the subject of studies for many years and there exists an extensive literature e.g. see Fryba [1]. In many papers the problem has been studied in the deterministic manner. However, due to many reasons the moving forces acting on highway bridges (vehicle axle pressures) are of random magnitude. Moreover, they arrive at the span at random times. Consequently, the traffic load on a bridge is a random process. Tung [2–4] was probably the first author to publish papers on the stochastic vibrations and reliability of a bridge beam subjected to a random train of moving point forces. In the papers by Śniady and co-authors [5–9] the analysis of the beam's vibrations, the estimation of the beam's reliability and fatigue modelled as the first crossing problem have been presented. The vibrations of a beam with various boundary conditions due to a train of random forces moving along the beam with a constant speed and in the same direction have been analysed by Zibdeh and Rackwitz [10, 11].

The problem of vibration of a suspension bridge under a random train of moving load has been discussed by Bryja and Śniady [12–14]. In all those afore-mentioned papers the random train of moving forces has been assumed to be a Poissonian moving load process which is an analogue to the Poissonian pulse process, see also Lin [15], Roberts [16, 17], Śniady [18], Mazur-Śniady and Śniady [19], Gładysz and Śniady [20]. A different approach to this problem has been shown by Paola and Riccardi [21], Riccardi [22]. In the paper [23] some aspects of a dynamics response of an infinite

beam and a plate resting on a two-parametric foundation to the passage of a train of random forces have been studied. In all cases it is assumed that parameters of the structure are deterministic.

On the other hand, the beam's parameters like geometry characteristics, material and damping properties might be uncertain to some extent. Their uncertainty may have a strong influence on the reliability of a structure in the dynamic context. Dynamic analysis of bridge beam under traffic flow often involves two kinds of uncertainty. One of them is randomness (stochastic variability) and the other is fuzziness which describe imprecision (vagueness). The random variability is described by use of probability theory and the imprecision by use of fuzzy sets introduced by Zadech [24]. Very often sufficient statistical data are not available. In this case a fuzzy function (fuzzy process) or fuzzy random variable (fuzzy stochastic process) is possible to employ for modelling purposes. The concept of fuzzy random variables was introduced by Kwarkernaak [25], Puri and Ralescu [26] combine both randomness and imprecision. The definition of the variance of fuzzy random variables can be found in the papers [27–29].

The theory of fuzzy stochastic differential systems has been presented in the paper [30]. Application the uncertain forecasting in engineering basing on fuzzy stochastic processes is presented in the monograph [31].

The loading of highway bridges is characterized by the occurrence of millions of repetitive random load events. This type of load causes material fatigue and leads to an ultimate damage of structure. Narrow-band stochastic vibration, where one frequency is dominating, is one of the factors which cause the acceleration of fatigue in bridge structures. In the problem of beam's vibrations under a random train of moving forces we want to determine the velocity of these forces for which the response of the beam is a narrow-band stochastic process. Spectral analysis of deterministic linear system under Poisson driven pulses and bridge beam under a random train of moving forces have been considered in [32] and [33], respectively. Spectral stochastic analysis of structures with random parameters has been presented in [34].

The paper presents the spectral analysis of the beam's vibration with uncertain parameters under a random train of moving forces which forms a filtered Poisson process. Very often we do not know the exact value of the first natural frequency of the bridge beam which has strong influence on spectral analysis. For this reason it is assumed that the uncertainty of the natural frequency is described by fuzzy number, random variable and fuzzy random variable. The introduction of the dynamic influence function allows the authors to obtain the spectral density function of the normal response. The derived expressions have been used to analyse the influence of the velocity of moving forces on spectral density function of the simply supported beam.

2. Statement of the problem – general solution

Let us consider vibrations of a beam of finite length L which is a linear, elastic structure. Vibrations are caused by a train of forces moving in the same direction, all

with equal, constant speed v (Figure 1). The forces arrive at the beam at random times t_k which constitute a Poisson process $N(t)$ with the parameter λ. The Poisson process $N(t)$ and its increment $dN(t)$ give the number of forces arriving in the time interval $(0, t)$ and $(t, t + dt)$ respectively $E[\cdot]$ denotes the expected value of the quantity in the brackets.
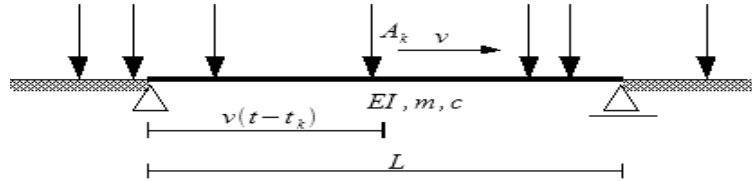

Fig. 1. Load pattern of bridge

Vibrations of the beam due to this train of forces are described by the following equation of motion:

$$EIw^{IV}(x, t) + c\dot{w}(x, t) + m\ddot{w}(x, t) = \sum_{k=1}^{N(t)} A_k \delta[x - v(t - t_k)], \tag{1}$$

where:
EI denotes the flexural rigidity of the beam,
c and m denotes the damping coefficient and the mass per-unit-length of the beam, respectively,
$\delta(\cdot)$ denotes the Dirac delta function, Roman numeral superscripts denote differentiation with respect to the spatial co-ordinate and superscript dots denote differentiation with respect to time.

In the loading process the amplitudes A_k are random variables, which are mutually independent and also independent on the times t_k and their expected values $E[A_k] = E[A]$, $E[A_k^2] = E[A^2]$ are known.

It is assumed that the deflection $w(x, t)$ of the beam has the form of the eigenfunction series:

$$w(x, t) = \sum_{n}^{\infty} y_n(t) W_n(x). \tag{2}$$

The eigenfunctions satisfy the equation:

$$W_n^{IV}(x) - \lambda_n^4 W_n(x) = 0, \quad (n = 1, 2, ...) \tag{3}$$

and appropriate boundary conditions. The symbol λ_n ($n = 1, 2, ...$) denotes the eigenvalue.

After substituting expression (2) into Equation (1) one obtains the set of uncoupled equations:

$$\ddot{y}_n(t) + 2\eta\dot{y}_n(t) + \omega_n^2 y_n(t) = \frac{1}{m\gamma_n^2}\sum_{k=1}^{N(t)} A_k W_n[v(t-t_k)]\left[H_T(t-t_k) - H_T\left(t-t_k-\frac{L}{v}\right)\right], \qquad (4)$$

where:

$$2\eta = \frac{c}{m}, \ \omega_n^2 = \lambda_n^4\frac{EJ}{m}, \quad \gamma_n^2 = \int_0^L W_n^2(x)dx, \quad H_T(t-t_k) = \begin{cases} 1 \text{ for } t_k \le t \le t_k + \dfrac{L}{v} \\ 0 \text{ for } t < t_k, t > t_k + \dfrac{L}{v} \end{cases} \quad \text{and}$$

$T = \dfrac{L}{v}$ is the time of force passage along the beam.

The steady-state solution of the Equation (4) can be obtained in the form of Stieltjes stochastic integral with respect to the Poisson process $N(t)$ as [5, 18]:

$$y_n(t) = \frac{1}{m\gamma_n^2}\int_{-\infty}^{t}\int_{\tau}^{z} A(\tau)h_n(t-\xi)W_n[v(\xi-\tau)]d\xi\, dN(\tau), \qquad (5)$$

where $z = \min\left(t, \tau+\dfrac{L}{v}\right)$, $h_n(t-\xi) = \Omega^{-1}\exp[-\eta(t-\xi)]\sin\Omega_n(t-\xi)$ is the impulse response function and $\Omega_n^2 = \omega_n^2 - \eta^2$ is the damped natural frequency.

After taking into account that the increments $dN(t)$ of the Poisson process satisfy relations [15]:

$$E\left[dN^k(t)\right] = \lambda\, dt \quad \text{for } k = 1, 2, \dots \qquad (6)$$

and

$$E\left[dN(t_1)\, dN(t_2)\right] = \lambda^2 dt_1\, dt_2 \quad \text{for } t_1 \ne t_2, \qquad (7)$$

the expected value and covariance function of the normal mode response $y_n(t)$ can be obtained from the expressions:

$$E[y_n(t)] = \frac{E[A]\lambda}{m\gamma_n^2}\int_{-\infty}^{t}\int_{\tau}^{z} h_n(t-\xi)W_n[v(\xi-\tau)]d\xi\, d,\tau \qquad (8)$$

and

$$C_{y_k y_n}(t_1, t_2) = \frac{E[A^2]\lambda}{m^2 \gamma_k^2 \gamma_n^2} \int_{-\infty}^{t} \int_{\tau}^{z_1} \int_{\tau}^{z_2} h_k(t_1 - \xi_1) h_n(t_2 - \xi_2) W_k[v(\xi_1 - \tau)]$$

$$W_n[v(\xi_2 - \tau)] d\xi_1 d\xi_2 d\tau \tag{9}$$

where:

$t = \min(t_1, t_2)$.

Now, our aim is to find the expression for spectral density function $\Phi_{y_n y_n}(\omega)$ using the covariance function given by Equation (9).

Notice that in the case of the Equation (4) it is not possible to find the spectral density in a simple algebraic form analogous to by a weakly stationary stochastic process [15, 35] because the response of the system is a filtered Poisson process. The covariance function (9) has a more complex form than when the dynamic system is excited by a weakly stationary stochastic process. To overcome this difficulty let us introduce the dynamic influence function $G_n(t)$ which is the beam's normal mode response at time t to the force $A_k = 1$ moving with the velocity v. The function $G_n(t)$ can be obtained from the integral [18]:

$$G_n(t-\tau) = \begin{cases} G_n^{(1)}(t-\tau) = \dfrac{1}{m\gamma_n^2} \displaystyle\int_{\tau}^{t} h_n(t-\xi) W_n[v(\xi-\tau)] d\xi \\[4pt] \text{for } t - \dfrac{L}{v} \leq \tau \leq t, \\[8pt] G_n^{(2)}(t-\tau) = \dfrac{1}{m\gamma_n^2} \displaystyle\int_{\tau}^{\tau+\frac{L}{v}} h_n(t-\xi) W_n[v(\xi-\tau)] d\xi \\[4pt] \text{for } 0 \leq \tau \leq t - \dfrac{L}{v} \text{ and } t \geq \dfrac{L}{v}. \end{cases} \tag{10}$$

The function $G_n^{(1)}(t-\tau)$ is the normal mode response at time t to the moving force $A_k = 1$, the arrival time is $\tau \in \left(t - \dfrac{L}{v}, t\right)$ and the force is acting on the beam (force vibration) whereas the function $G_n^{(2)}(t-\tau)$ is the normal mode response to the force that left the beam i.e. $\tau \in \left(0, t - \dfrac{L}{v}\right)$ (free vibration). Now, using the normal mode dynamic influence function the covariance function for steady-state normal mode response has the form:

$$C_{y_k y_n}(t_1, t_2) = E\left[A^2\right]\lambda \int\limits_{-\infty}^{t} G_k(t_1 - \tau)G_n(t_2 - \tau)d\tau =$$

$$= E\left[A^2\right]\lambda \int\limits_{0}^{\infty} G_k(\xi)G_n(t_2 - t_1 + \xi)d\xi = C_{y_k y_n}(t_2 - t_1). \tag{11}$$

As can be seen from the Equation (11) normal mode response $y_n(t)$ in the case under consideration is a weakly stationary stochastic process. The expression (11) can be presented in a double integral form:

$$C_{y_k y_n}(t) = E\left[A^2\right]\lambda \int\limits_{-\infty}^{t_1}\int\limits_{-\infty}^{t_2} G_k(t_1 - \xi_1)\,G_n(t_2 - \xi_2)\,\delta(\xi_1 - \xi_2)\,d\xi_1\,d\xi_2 =$$

$$= E\left[A^2\right]\lambda \int\limits_{0}^{\infty}\int\limits_{0}^{\infty} G_k(\tau_1)\,G_n(\tau_2)\,\delta(t + \tau_2 - \tau_1)\,d\tau_1\,d\tau_2, \tag{12}$$

where $t = t_2 - t_1$.

The relation (12) can be used to find the cross-spectral density function $\Phi_{y_k y_n}(\omega)$ of the normal modes responses $y_k(t)$ and $y_n(t)$. Taking into account the Equation (12) and the relationships between the covariance function and the cross-spectral density function [15, 35] we obtain:

$$\Phi_{y_k y_n}(\omega) = \frac{1}{2\pi}\int\limits_{-\infty}^{\infty} C_{y_k y_n}(t)\,e^{-i\omega t}dt =$$

$$= \frac{1}{2\pi}E\left[A^2\right]\lambda \int\limits_{-\infty}^{\infty}\int\limits_{0}^{\infty}\int\limits_{0}^{\infty} G_k(\tau_1)\,G_n(\tau_2)\,\delta(t + \tau_2 - \tau_1)\,e^{-i\omega t}d\tau_1\,d\tau_2\,dt =$$

$$= \frac{1}{2\pi}E\left[A^2\right]\lambda \int\limits_{0}^{\infty} G_k(\tau_1)\,e^{-i\omega\tau_1}d\tau_1 \int\limits_{0}^{\infty} G_n(\tau_2)\,e^{i\omega\tau_2}d\tau_2 \int\limits_{-\infty}^{\infty} e^{-i\omega t}\delta(t)dt. \tag{13}$$

The expression (13) can be presented in a short form:

$$\Phi_{y_k y_n}(\omega) = \Phi_{y_k y_n}(\omega_k, \omega_n, \omega) = \frac{E\left[A^2\right]\lambda}{2\pi} J_k(\omega) J_n^*(\omega)$$

$$= \frac{E\left[A^2\right]\lambda}{2\pi} J_k(\omega_k, \omega) J_n^*(\omega_n, \omega). \tag{14}$$

where:

$$J_n(\omega) = \int\limits_0^\infty G_n(\tau) e^{-i\omega\tau} d\tau = \int\limits_0^{\frac{L}{v}} G_n^{(1)}(\tau) e^{-i\omega\tau} d\tau + \int\limits_{\frac{L}{v}}^\infty G_n^{(2)}(\tau) e^{-i\omega\tau} d\tau,$$ (15)

and the superscript * indicates the complex conjugate.

The function $J_n(\omega)$ represents the Fourier transformation of the normal mode dynamic influence function $G_n(t)$. Equation (14) may be regarded as an analogy to weakly stationary stochastic process for a random train of moving forces and when the response of the linear system is a filtered Poisson process.

Let the assumed parameters of the beam be random and independent since the load process. The Equation (5) using the normal mode random dynamic function $G_n(t - \tau)$ has a form:

$$y_n(t) = \int\limits_{-\infty}^t A(\tau) G_n(t - \tau) dN(\tau).$$ (16)

Thus, in order to determine the probabilistic characteristics of the normal mode response (generalized coordinates) of the beam, one can apply the expectancy operator to Equation (16) and consequently obtain the expected value:

$$E[y_n(t)] = E[A]\lambda \int\limits_{-\infty}^t E[G_n(t - \tau)] d\tau = E[A]\lambda \int\limits_{t-\frac{L}{v}}^t E\left[G_n^{(1)}(t - \tau)\right] d\tau$$

$$+ E[A]\lambda \int\limits_{-\infty}^{t-\frac{L}{v}} E\left[G_n^{(2)}(t - \tau)\right] d\tau =$$

$$= E[A]\lambda \int\limits_0^\infty E[G(\xi)] d\xi = \lambda E[A]\int\limits_0^{\frac{L}{v}} E\left[G_n^{(1)}(\xi)\right] d\xi + E[A]\lambda \int\limits_{\frac{L}{v}}^\infty E\left[G_n^{(2)}(\xi)\right] d\xi$$ (17)

and the covariance of the normal modes:

$$C_{y_k y_n}(t_1, t_2) = E[A^2]\lambda \int\limits_{-\infty}^t E[G_k(t_1 - \tau) G_n(t_2 - \tau)] d\tau$$

$$+ E^2[A]\lambda^2 \int\limits_{-\infty}^{t_1} \int\limits_{-\infty}^{t_2} C_{G_k G_n}(t_1 - \tau_1, t_2 - \tau_2) d\tau_1 d\tau_2,$$ (18)

where:

$$C_{G_kG_n}(t_1 - \tau_1, t_2 - \tau_2) = E\left[G_k(t_1 - \tau_1)G_n(t_2 - \tau_2)\right] - E\left[G_k(t_1 - \tau_1)\right]E\left[G_n(t_2 - \tau_2)\right],$$

$t = \min(t_1, t_2)$.

The Equation (18) can be presented in the form:

$$C_{y_ky_n}(t_1, t_2) = C_{y_ky_n}(t_2 - t_1) = C_{y_ky_n}(t) =$$

$$E[A^2]\lambda \int\limits_0^\infty E[G_k(\xi)G_n(t_2 - t_1 + \xi)]d\xi + E^2[A]\lambda^2 \int\limits_0^\infty\int\limits_0^\infty C_{G_kG_n}(\xi_1, \xi_2)d\xi_1 d\xi_2. \tag{19}$$

In similar way like Equation (12) the above expression can be presented in a double integral form:

$$C_{y_ky_n}(t_1, t_2) = C_{y_ky_n}(t_2 - t_1) =$$

$$E[A^2]\lambda \int\limits_0^\infty\int\limits_0^\infty E[G_k(\xi_1)G_n(\xi_2)]\delta(\xi_2 - \xi_1 + t)d\xi_1 d\xi_2$$

$$+E^2[A]\lambda^2 \int\limits_0^\infty\int\limits_0^\infty C_{G_kG_n}(\xi_1, \xi_2)d\xi_1 d\xi_2 = C_{y_ky_n}(t). \tag{20}$$

Using the well-known relationship between the cross-spectral density function $\Phi_{y_ky_n}(\omega)$ and the covariance function $C_{y_ky_n}(t)$ of the weakly stationary process [15, 35] since Equation (20) we have:

$$\Phi_{y_ky_n}(\omega) = \frac{1}{2\pi}\int\limits_{-\infty}^\infty C_{y_ky_n}(t)e^{-i\omega t}dt =$$

$$\frac{1}{2\pi}E[A^2]\lambda \int\limits_{-\infty}^\infty\int\limits_0^\infty\int\limits_0^\infty E[G_k(\xi_1)G_n(\xi_2)]\delta(t + \xi_2 - \xi_1)e^{-i\omega t}d\xi_1 d\xi_2 dt$$

$$+\frac{1}{2\pi}E^2[A]\lambda^2 \int\limits_{-\infty}^\infty\int\limits_0^\infty\int\limits_0^\infty C_{G_kG_n}(\xi_1, \xi_2)e^{-i\omega t}d\xi_1 d\xi_2 dt, \tag{21}$$

and lastly after some algebra we can obtain the cross-spectral density function of the normal mode response of the beam which reads

$$\Phi_{y_ky_n}(\omega) = \left[\frac{E[A^2]\lambda}{2\pi} + E[A^2]\lambda^2\delta(\omega)\right]\int\limits_0^\infty\int\limits_0^\infty E[G_k(\xi_1)G_n(\xi_2)]e^{-i\omega\xi_1}e^{i\omega\xi_2}d\xi_2 d\xi_1$$

$$-E^2[A]\lambda^2\delta(\omega)\int\limits_0^\infty\int\limits_0^\infty E[G_k(\xi_1)e^{-i\omega\xi_1}]E[G_n(\xi_2)e^{i\omega\xi_2}]d\xi_2 d\xi_1. \tag{22}$$

Finally, the relationship for the cross-spectra density function of the modal response can be presented in the concise form

$$\Phi_{y_k y_n}(\omega) = \left\{ \frac{E[A^2]\lambda}{2\pi} + E^2[A]\lambda^2 \delta(\omega) \right\} E\left[J_k(\omega) J_n^*(\omega) \right]$$

$$- E^2[A]\lambda^2 \delta(\omega) E\left[J_k(\omega) \right] E\left[J_n^*(\omega) \right]. \tag{23}$$

The probabilistic moments $E[J_n(\omega)]$ and $E[J_k(\omega) J_n^*(\omega)]$ can be found using the perturbation method, the Monte Carlo Method or the method of many realizations.

Both of the bending rigidity EI of the beam and its mass m are not always uniquely determined. These quantities determine the natural frequencies $\omega_n^2 = \lambda_n^4 \dfrac{EI}{m}$ of the beam therefore the latter natural frequencies are not uniquely determined as well.

Let us consider different type natural frequencies uncertain:
- the natural frequencies are fuzzy numbers,
- the natural frequencies are random variables,
- the natural frequencies are fuzzy random variables.

Let a fuzzy set A is defined in the space R, $A \in R$. The fuzzy set A is described by membership function $\mu_A(x)$ which maps the space R to the interval $[0, 1]$ (see Figure 2). From the fuzzy sets the crisp sets $A_\alpha = \{x \in R | \mu_A(x) \geq \alpha\}$ are called α-level sets. Let $x_{\alpha l}, x_{\alpha r}$ are the lower and upper endpoints of $x_\alpha = [x_{\alpha l}, x_{\alpha r}]$.

Let us consider the natural frequencies as fuzzy numbers $\omega_n = \omega_{n\alpha} = [\omega_{n\alpha l}, \omega_{n\alpha r}]$. The fuzzy cross-spectral density function is fuzzy and the Equation (14) is modified to the form:

$$\Phi_{y_k y_n \alpha}(\omega) = \Phi_{y_k y_n}(\omega_{k\alpha}, \omega_{n\alpha}, \omega) = \frac{E[A^2]\lambda}{2\pi} J_{k\alpha}(\omega) J_{n\alpha}^*(\omega)$$

$$= \frac{E[A^2]\lambda}{2\pi} J_k(\omega_{k\alpha}, \omega) J_n^*(\omega_{n\alpha}, \omega), \tag{24}$$

The Equation (24) describes the bunch cross-spectral density function $\Phi_{y_k y_n \alpha}(\omega)$ for parameters $\alpha \in [0, 1]$.

In the case if the natural frequencies are random variables we use the Equation (23).

Assuming that the natural frequencies are fuzzy random variables since the Equation (23) we have:

$$\Phi_{y_k y_n \alpha}(\omega) = \left[\frac{E[A^2]\lambda}{2\pi} + E^2[A]\lambda^2 \delta(\omega) \right] E[J_{k\alpha}(\omega) J_{n\alpha}^*(\omega)]$$

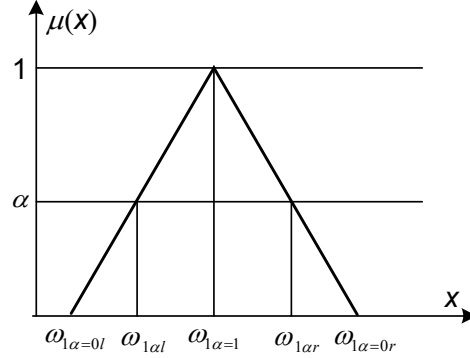$$- E^2[A]\lambda^2 \delta(\omega) E[J_{k\alpha}(\omega)] E[J_{n\alpha}^*(\omega)], \tag{25}$$

Fig. 2. Membership function of the first natural frequency $\omega_{1\alpha}$

Using α-level optimization procedure [31] for arbitrary $\alpha = \alpha_k \in [0, 1]$ we can find the smallest cross-spectral density function $\Phi_{y_k y_n \alpha\, l}(\omega)$ and the largest cross-spectral density function $\Phi_{y_k y_n \alpha\, r}(\omega)$. The real valued the cross-spectral density function can be defined as

$$\Phi_{y_k y_n}(\omega) = \frac{1}{2} \int_0^1 [\Phi_{y_k y_n \alpha l}(\omega) + \Phi_{y_k y_n \alpha r}(\omega)] d\alpha. \tag{26}$$

The definition of the real value cross-spectral density function (26) is based on definition of covariance function given in [27].

Remark

It would be relatively easy to generalize the above solution to the case when the load is a fuzzy filtered Poisson process, i.e. when the parameters λ and amplitudes A_k are fuzzy. In the numerical analysis we considered only the fuzziness of the moving forces velocity.

3. Particular solution and numerical results

As an example, the steady-state response of a simply supported beam is determined. For a simply supported beam the eigenvalues λ_n, the natural frequencies and the eigenfunctions are equal to:

$$\lambda_n = \frac{n\pi}{L}, \quad \omega_n = \left(\frac{n\pi}{L}\right)^2 \sqrt{\frac{EI}{m}}, \quad W_n(x) = \sin\frac{n\pi x}{L}. \tag{27}$$

The normal mode dynamic influence functions are obtained as:

$$G_n^{(1)}(t-\tau) = \frac{2}{mLM_n}$$
$$\left\{a_{1n}\sin\beta_n(t-\tau) + a_{2n}\cos\beta_n(t-\tau) + e^{-\eta(t-\tau)}\left[a_{3n}\sin\Omega_n(t-\tau) - a_{2n}\cos\Omega_n(t-\tau)\right]\right\}, \quad (28)$$

$$G_n^{(2)}(t-\tau) = \frac{2}{mLM_n}e^{-\eta\left(t-\tau-\frac{L}{v}\right)}\left[b_{1n}\sin\Omega_n\left(t-\tau-\frac{L}{v}\right) + b_{2n}\cos\Omega_n\left(t-\tau-\frac{L}{v}\right)\right], \quad (29)$$

where:

$$\beta_n = \frac{n\pi v}{L},$$
$$\Omega_n^2 = \omega_n^2 - \eta^2,$$
$$M_n = \left(\omega_n^2 - \beta_n^2\right) + 4\eta^2\beta_n^2,$$
$$a_{1n} = \omega_n^2 - \beta_n^2,$$
$$a_{2n} = -2\eta\beta_n,$$
$$a_{3n} = \frac{\beta_n}{\Omega_n}\left[2\eta^2 - \left(\omega_n^2 - \beta_n^2\right)\right],$$
$$b_{1n} = \frac{(-1)^n}{\Omega_n}\left(a_{1n}\beta_n + a_{2n}\eta\right) + e^{-\eta\frac{L}{v}}\left[a_{3n}\cos\Omega_n\frac{L}{v} + a_{2n}\sin\Omega_n\frac{L}{v}\right],$$
$$b_{2n} = (-1)^n a_{2n} + e^{-\eta\frac{L}{v}}\left(a_{3n}\sin\Omega_n\frac{L}{v} - a_{2n}\cos\Omega_n\frac{L}{v}\right).$$

The Fourier transformation of the normal mode dynamic influence function for simply supported beam has a form:

$$J_n(\omega) = \frac{1}{mLM_n}\left\{\frac{a_{1n} + ia_{2n}}{\beta_n - \omega}\left[1 - e^{-i(\beta_n - \omega)\frac{L}{v}}\right] + \frac{a_{1n} - ia_{2n}}{\beta_n + \omega}\left[1 - e^{-i(\beta_n + \omega)\frac{L}{v}}\right]\right.$$

$$+ \frac{a_{3n}(-\omega + \Omega_n - i\eta) + a_{2n}[i(\omega - \Omega_n - i\eta)]}{(\Omega_n + \omega)^2 + \eta^2}\left[1 - e^{-[i(\omega - \Omega_n) + \eta]\frac{L}{v}}\right]$$

$$+ \frac{a_{3n}(-\omega + \Omega_n - i\eta) + a_{2n}[i(\omega + \Omega_n - \eta)]}{(\Omega_n + \omega)^2 + \eta^2}\left[1 - e^{-[i(\omega + \Omega_n) + \eta]\frac{L}{v}}\right]$$

$$+ e^{-i\omega\frac{L}{v}}\left[\frac{b_{1n}(-\omega + \Omega_n - i\eta) + b_{2n}[i(-\omega + \Omega_n) + \eta]}{(\Omega_n - \omega)^2 + \eta^2}\right.$$

$$\left.\left. + \frac{b_{1n}(\omega + \Omega_n + i\eta) + b_{2n}[i(-\omega - \Omega_n) + \eta]}{(\Omega_n + \omega)^2 + \eta^2}\right]\right\}. \quad (30)$$

The expressions (14, 24–25) have been used to analyse the influence of moving forces velocity v on the spectral density function of a simply supported beam. The analysis has been done for the first natural frequency of the beam; i.e., $k = n = 1$ ($\omega_k = \omega_n = \omega_1$).

It has been assumed that the parameters of the beam are as follows: the span $L = 20$ m, the damping ratio $\xi = 0.02$, where $\eta = 0.5 \, c/m = \xi\omega_1$. Let the first natural frequency $\omega_{1\alpha}$, be fuzzy numbers with triangular membership function, as depicted in Figure 2. In this case we have $\omega_{1\alpha} = [\omega_{1\alpha l}, \omega_{1\alpha r}] = [(1 - \alpha)\omega_{1\alpha=0l} + \alpha\omega_{1\alpha=1}, (1 - \alpha)\omega_{1\alpha=0r} + \alpha\omega_{1\alpha=1}]$. The velocities of the moving forces are crisp number and given by formulae

$$v = \frac{L}{2\pi a}\omega_{1\alpha=1} = \frac{L}{aT_{1\alpha=1}} \text{ or fuzzy number and equal } v_\alpha = \frac{L}{2\pi a}\omega_{1\alpha} = \frac{L}{aT_{1\alpha}}, \text{ where } a = 0.5$$

or $a = 1$. It is assumed that $\omega_{1\alpha=0l} = 5.0 \text{ s}^{-1}$, $\omega_{1\alpha=1} = 5.3 \text{ s}^{-1}$, $\omega_{1\alpha=0r} = 5.6 \text{ s}^{-1}$. The value $\omega_{1\alpha=1} = 5.3 \text{ s}^{-1}$ was calculated for the steel simply supported beam. The following assumptions were made: the length of the beam $L = 20$ m, the moment of inertia equal to $I = 0.0007 \text{ m}^4$, the mass-per-unit-length equal to $m = 3000$ kg/m and Young's modulus $E = 200$ GPa ($2 \times 10^8 \text{ kN/m}^2$). The spectral density functions in the case of a fuzzy set of the natural frequencies for selected values of the parameter "a" are presented in Figure 3.

The Figure 4 show the graphs of the spectral density function $\Phi_{y_n y_n}(\omega)$ for fixed value $\omega_1 = 5.3 \text{ s}^{-1}$ and different values of parameter a. From these figures one can see that the beam response process is a narrow-band process with a clear peak for $\omega_n = \omega_1$. The velocity of the moving forces increases together with the growth of ω_1. That allows us to estimate the value of the velocity v dangerous for the structure.
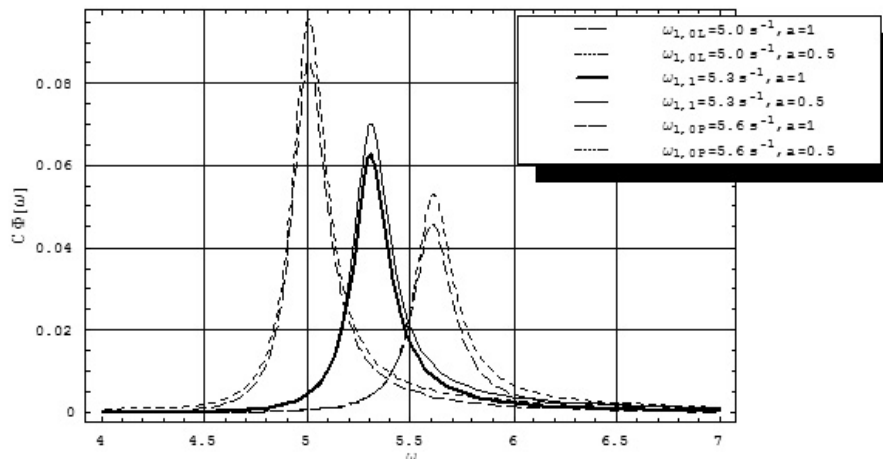

Fig. 3. The spectral density function in the case of a fuzzy set of the natural frequencies
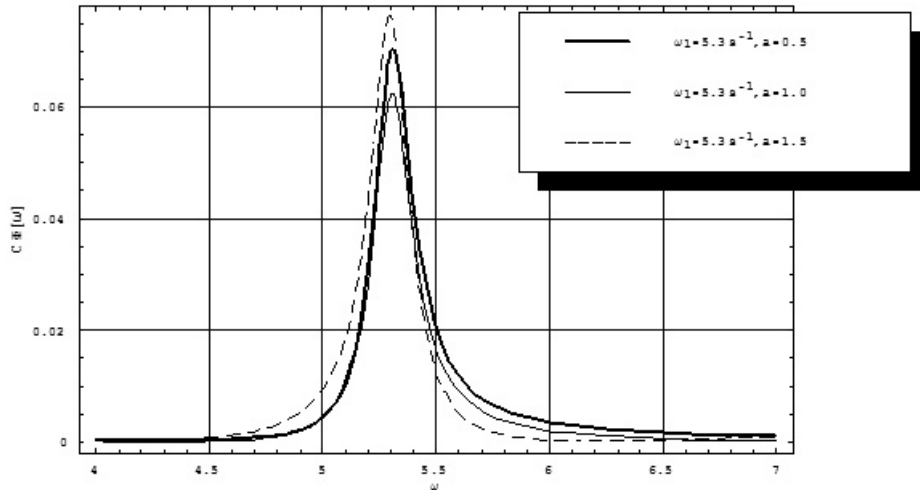for selected values of the parameter "a"

Fig. 4. The spectral density function for fixed value ω = 5.3 s^{-1} and different values of the parameter "*a*"

Results presented in Figure 5 are calculated for the case where the natural frequencies are fuzzy random variables. The results obtained by the method of many realizations, assuming expected value of the natural frequency equal $E[\omega_1]$ = 5.3 s^{-1}. The natural frequency has been assumed to be the random variables with uniform distribution and variation coefficient equal to 0.1.
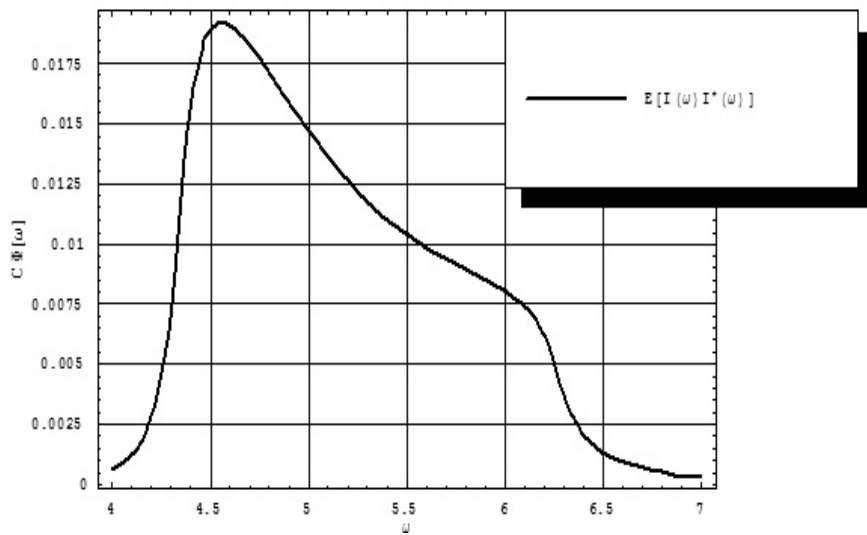
Fig. 5. The probabilistic moment $E[I(\omega)I^*(\omega)]$ found by the method of many realizations

The space illustration of the spectral density function as the function of the fuzzy natural frequencies is presented in Figure 6. We observe (see Figure 7) that peaks of the spectral density function decrease together with increase of the natural frequencies.
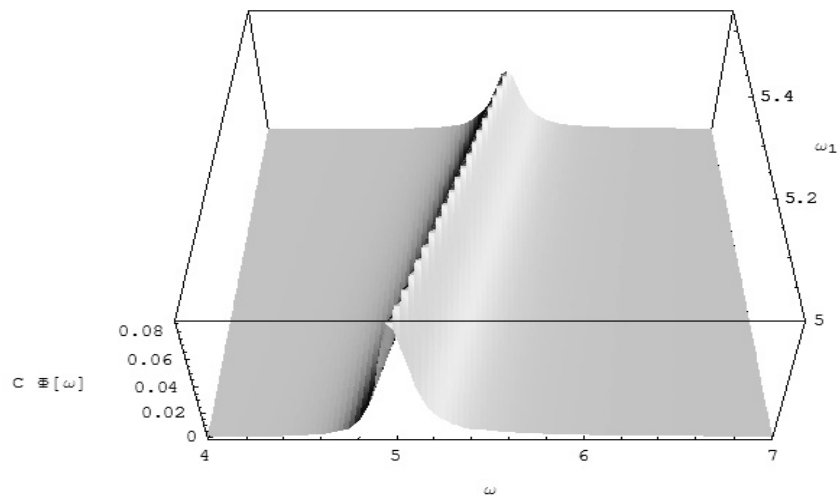
Fig. 6. The space illustration of the spectral density function as the function
of the fuzzy natural frequencies
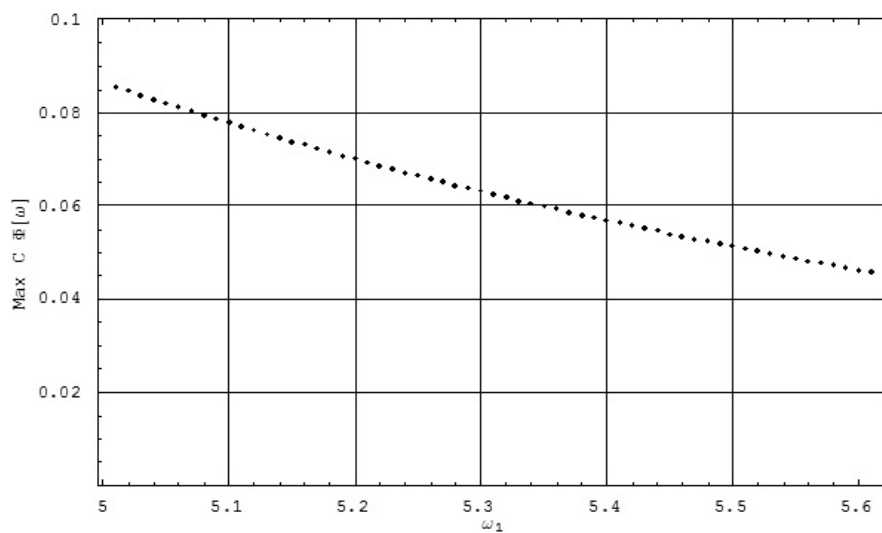
Fig. 7. The graph of the maximums of the spectral density function for the fuzzy natural frequencies

The constant C in Figures 3–7 takes the shape of $C = \dfrac{E[A^2]\lambda}{mL^2}$.

4. Conclusions

The paper presents the spectral analysis of beam's vibration with uncertain parameters under a random train of moving forces which forms a filtered Poisson process. It has been assumed that the uncertainty of natural frequencies is modelled by the fuzzy numbers, random variables or fuzzy random variables. In this case it is impossible to obtain a solution for the spectral density function of system response in the classical way like for excitation by a weakly stationary stochastic process. To overcome these difficulties the random dynamic moving influence function and the fuzzy random dynamic moving influence function have been introduced, which allows to obtain the spectral density function of the normal mode response of the beam. Presented solutions allow to analyse the influence of different type of uncertainty (randomness and imprecision) of the bridge's beam on the spectral density function of the response. To find probabilistic moments in the expressions for the spectral density function it is convenient to use the method of many realizations then for example perturbation method. Verification of results is possible also by means of Monte Carlo Method.

In presented example it has been assumed that natural frequencies are random variables with uniform distribution. It is possible to assume other distributions, based on results of statistical analyses, for example Gaussian distribution. Usually the randomness of constructions parameters is relatively low, therefore on presented analysis the variation coefficient value 0.1 has been assumed. For higher values of variation coefficient influence of the structure parameters randomness on the probabilistic characteristics response of the structure is more significant.

References

[1] Fryba L.: *Vibration of solids and structures under moving loads*, Academia, Prague, 1972.
[2] Tung C.C.: *Random response of highway bridges to vehicle loads*, Proceedings of the American Society of Civil Engineers, Journal of the Engineering Mechanics Division 93, 1967, pp. 73–94.
[3] Tung C.C.: *Response of highway bridges to renewal traffic loads*, Proceedings of the American Society of Civil Engineers, Journal of the Engineering Mechanics Division 95, 1969, pp. 41–57.
[4] Tung C.C.: *Life expectancy of highway bridges to vehicle loads*, Proceedings of the American Society of Civil Engineers, Journal of the Engineering Mechanics Division 95, 1969, pp. 1417–1428.
[5] Iwankiewicz R., Śniady P.: *Vibration of a beam under a random stream of moving forces*, Journal of Structural Mechanics, Vol. 12, 1984, pp. 13–26.
[6] Śniady P.: *Vibration of a beam due to a random stream of moving forces with random velocity*, Journal of Sound and Vibration, Vol. 97, 1984, pp. 23–33.
[7] Sieniawska R., Śniady P.: *First passage problem of the beam under a random stream of moving forces*, Journal of Sound and Vibration, Vol. 136, 1990, pp. 177–185.

[8] Sieniawska R., Śniady P.: *Life expectancy of highway bridges due to traffic load*, Journal of Sound and Vibration, Vol. 140, 1990, pp. 31–38.

[9] Śniady P., Biernat S., Sieniawska R., Żukowski S.: *Vibrations of the beam due to a load moving with stochastic velocity*, Probabilistic Engineering Mechanics 16, 2001, pp. 53–59.

[10] Zibdeh H.S., Rackwitz R.: *Response moments of an elastic beam subjected to Poissonian moving loads*, Journal of Sound and Vibration, Vol. 188, 1995, pp. 479–495.

[11] Zibdeh H.S., Rackwitz R., *Moving loads on beams with general boundary conditions*, Journal of Sound and Vibration, Vol. 195, 1996, pp. 85–102.

[12] Bryja D., Śniady P.: *Random vibration of a suspension bridge due to highway traffic*, Journal of Sound and Vibration, Vol. 125, 1988, pp. 379–387.

[13] Bryja D., Śniady P.: *Spatially coupled vibrations of a suspension bridge under random highway traffic*, Earthquake Engineering and Structural Dynamics, Vol. 20, 1991, pp. 999–1010.

[14] Bryja D., Śniady P.: *Stochastic non-linear vibrations of highway suspension bridge under inertial sprung moving load*, Journal of Sound and Vibration, Vol. 216, 1998, pp. 507–519.

[15] Lin Y.K., Cai G.Q.: *Probabilistic structural dynamics*, Advanced theory and applications, McGraw-Hill, New York, 1995.

[16] Roberts J.B.: *The response of linear vibratory systems to random impulses*, Journal of Sound and Vibration, Vol. 2, 1965, pp. 375–390.

[17] Roberts J.B.: *System response to random impulses*, Journal of Sound and Vibration, Vol. 24, 1972, pp. 23–34.

[18] Śniady P.: *Dynamic response of linear structures to a random stream of pulses*, Journal of Sound and Vibration, Vol. 131, 1989, pp. 91–102.

[19] Mazur-Śniady K., Śniady P.: *Dynamic response of linear structures to a random stream of arbitrary impulses in time and space*, Journal of Sound and Vibration, Vol. 110, 1986, pp. 59–68.

[20] Gładysz M., Śniady P.: *Random vibrations of a discrete system under a series of loads constituting a Poisson process* (in Polish), Archives of Civil Engineering XXX, Vol. 1, 1984, pp. 37–51.

[21] Paola M.D., Ricciardi G.: *Vibration of a bridge under a random train of moving loads*, Proceeding of the 6th Special Conference of Probabilistic Mechanics and Structural and Geotechnical Reliability, 1992, pp. 136–139.

[22] Riccardi G.: *Random vibration of beam under moving loads*, Journal of Engineering Mechanics, Vol. 120, 1994, pp. 2361–2380.

[23] Rystwej A., Śniady P.: *Dynamic response of an infinite beam and plate to a stochastic train of moving forces*, Journal of Sound and Vibration, Vol. 299, 2007, pp. 1033–1048.

[24] Zadeh L.A.: *Fuzzy sets*, Information Control, Vol. 8, 1965, pp. 338–353.

[25] Kwarkernaak H.: *Fuzzy random variables (I)*, Information Sciences, Vol. 15, 1978, pp. 1–29.

[26] Puri M.I., Ralescu D.A.: *Fuzzy random variables*, Journal of Mathematical Analysis and Application, Vol. 114, 1986, pp. 409–422.

[27] Körner R.: *On the variance of fuzzy random variables*, Fuzzy Sets and Systems, Vol. 92, 1997, pp. 83–93.

[28] Feng Y., Hu L., Shu H.: *The variance and covariance of fuzzy random variables and their applications*, Fuzzy Sets and Systems, Vol. 120, 2001, pp. 487–497.

[29] Hu L., Wu R., Shao S.: *Analysis of dynamical systems whose inputs are fuzzy stochastic processes*, Fuzzy Sets and Systems, Vol. 129, 2002, pp. 111–118.

[30] Feng Y.: *The solutions of linear fuzzy stochastic differential systems*, Fuzzy Sets and Systems, Vol. 140, 2003, pp. 541–554.

[31] Möller B., Beer M.: *Fuzzy Randomness, Uncertainty in Civil Engineering and Computational Mechanics*, Springer, 2004.

[32] Gładysz M., Śniady P.: *Spectral response of linear system under Poisson driven pulses*, Archives of Civil and Mechanical Engineering, Vol. V, No. 3, 2005, pp. 15–30.

[33] Gładysz M., Śniady P.: *The spectral analysis of a beam under a random train of moving forces*, Studia Geotechnica et Mechanica, Vol. XXIX, No. 3–4, 2007, pp. 45–56.

[34] Śniady P., Adamowski R., Kogut G., Zielichowski-Haber W.: *Spectral stochastic analysis of structures with uncertain parameters*, Probabilistic Engineering Mechanics, Vol. 23, 2008, pp. 76–83.

[35] Soong T.T., Grigoriu M.: *Random vibration of mechanical and structural systems*, PTR Prentice Hall Englewood Cliffs, 1993.

Gęstość widmowa drgań belki mostowej o niepewnych parametrach poddanej działaniu losowej serii sił ruchomych

W pracy zaprezentowano analizę widmową drgań belki o niepewnych parametrach, poddanej działaniu losowej serii ruchomych sił. Siły te tworzą proces Poissona. W analizie przyjęto, że niepewność wielkości częstości własnych można uwzględnić, uznając je za liczby rozmyte, zmienne losowe lub rozmyte zmienne losowe. Wprowadzono dynamiczną funkcję wpływu o charakterze losowo-rozmytym, dzięki której można otrzymać wygodne dla dalszych rozważań i obliczeń numerycznych związki, które określają funkcję gęstości widmowej drgań belki.

The influence of hot-working conditions on a structure of high-manganese steel

A. GRAJCAR, M. OPIELA, G. FOJT-DYMARA

Silesian University of Technology, Konarskiego 18a, 44-100 Gliwice, Poland

The high-manganese steels with the austenitic structure belong to a group of modern steels predicted to use in the automotive industry. The chemical composition of the steel containing 25% Mn, solution hardened by Si and Al was developed. Microadditions of Nb and Ti introduced into the steel creating stable nitrides and carbides should act by precipitation hardening and inhibit a grain growth of recrystallized austenite. The aim of the work was to determine the influence of various hot-working conditions on a structure of the investigated steel. The processes controlling work-hardening and removing strengthening after finishing the hot-working were identified. The preliminary upset forging by the use of eccentric press with a degree of deformation in a range of 20 to 60% and at temperatures of 850 and 1000 °C was carried out. On the basis of determined conditions the multi-stage axial compression tests ensuring the fine-grained austenite structure were performed.

Keywords: *hot-working, high-manganese steel, TRIP effect, dynamic recrystallization, microalloying*

1. Introduction

Automotive industry is one of the most dynamically developing branches of the global market. Strong competition in the field of automotive market and expansion of new materials with low density, based on aluminium, magnesium as well as polymer composite materials, in last twenty years have led to great activity of steel concerns which had to meet the challenges of the beginning of XXI century. A new look at the role of individual elements generally used for steels and the possibility of new metallurgical technologies application have led to development of steels with a wide range of mechanical properties and formability used in automotive industry. These are IF – (Interstitial Free), BH – (Bake Hardening), IS – (Isotropic), DP – (Dual Phase), TRIP – (TRansformation Induced Plasticity), CP – (Complex Phase) and TMS – (Martensitic) steels [1, 2].

New possibilities appeared at the beginning of this century, when the effect of strain-induced martensitic transformation of γ phase was attempted to be applied in austenitic steels. This effect was used many years ago but for expensive Cr-Ni steels [3]. Nowadays, new group of high-manganese austenitic steels with variable concentration of Mn, Al and Si was proposed showing high potential for their application in automotive industry. These steels meet the needs of automotive industry in a very wide range, concerning optimization of vehicles' mass and fuel consumption, safety of passengers and limiting the pollution of environment caused by motorization [4–6].

In case of manganese concentration below 25% it's possible to use TRIP effect (Transformation Induced Plasticity) consisting in steel hardening in the consequence of $\gamma_{A1} \to \varepsilon_{A3}$ or $\gamma_{A1} \to \varepsilon_{A3} \to \alpha'_{A2}$ martensitic transformation occurring during cold forming [4]. Martensite ε with A3 hexagonal lattice is formed only when stacking fault energy SFE of austenite is lower than 20 mJ/m^2 [5, 7]. Addition of Al into steel increases SFE and austenite stability which leads to suppressed influence on martensitic transformation. While the addition of Si decreases SFE and allows occurring of $\gamma \to \varepsilon$ transformation. In case when Mn concentration in the steel exceeds 25%, the stability of austenite during plastic deformation is maintained enhancing mechanical properties due to mechanical twinning – TWIP effect (TWinnig Induced Plasticity) [4, 8].

In contradistinction to numerous researches performed to determine the behaviour of high-manganese steels in the conditions of cold plastic deformation, not many works devote attention to hot-working of this group of steels. In order to develop the manufacturing methods, it is important to determine the flow behaviour of steels under hot-working conditions. Several works concern the behaviour of Fe-Cr-Mn, Fe-Mn and Fe-Mn-Al steels in the hot-working conditions [8, 9]. However, there are only a few papers on high-manganese steels containing silicon and microadditions [10–12]. Their application can contribute to mechanical properties increase of this group of steels, likewise in case of steels with A2 lattice matrix [13, 14].

2. Experimental procedure

The investigations were carried out on high-manganese steel with 0.054% C, 24.4% Mn, 3.5% Si, 1.6% Al, 0.0039% N, 0.029% Nb and 0.075% Ti. The melt was done in Balzers VSG-50 vacuum induction furnace. Liquid metal was cast into moulds in argon shield. Obtained 25 kg ingots were subjected to open die forging to 220 mm wide and 20 mm thick flats, from which cylindrical $\varnothing\ 10 \times 12$ mm samples were made. Preliminary tests consisted in solutioning of the steel from a temperature range of 800–1100 °C. The specimens were subjected to hot upsetting in 850 and 1000 °C with 20, 40 and 60% reduction. Part of samples deformed in 1000 °C with 40% reduction was isothermally held for 0 to 64 s. Upsetting was conducted using PMS 50 eccentric press with strain rate around 30 s^{-1}.

According to preliminary tests the conditions of hot-working ensuring fine-grained microstructure of the steel were selected. Annealing temperature of samples and a range of temperature of hot-working were chosen according to the kinetics of interstitial phases' precipitation in the steel. In this case the dependence (1) was implemented:

$$\log [M] [X] = B - A/T \tag{1}$$

where:

[M] and [X] – mass fractions of Nb and Ti as well as N and C dissolved in the solid solution at the T temperature (in K),

A and *B* – constants dependent on the phase kind [15].

Hot-working was realized in several-stage axisymmetrical compression test by the use of Gleeble 3800 thermo-mechanical simulator in the Institute for Ferrous Metallurgy in Gliwice. The parameters of carried out thermo-mechanical processing are shown in Figure 1. The specimens were inserted in a vacuum chamber, where they were resistance-heated. Tantalum foils were used to prevent sticking and graphite foils as a lubricant.
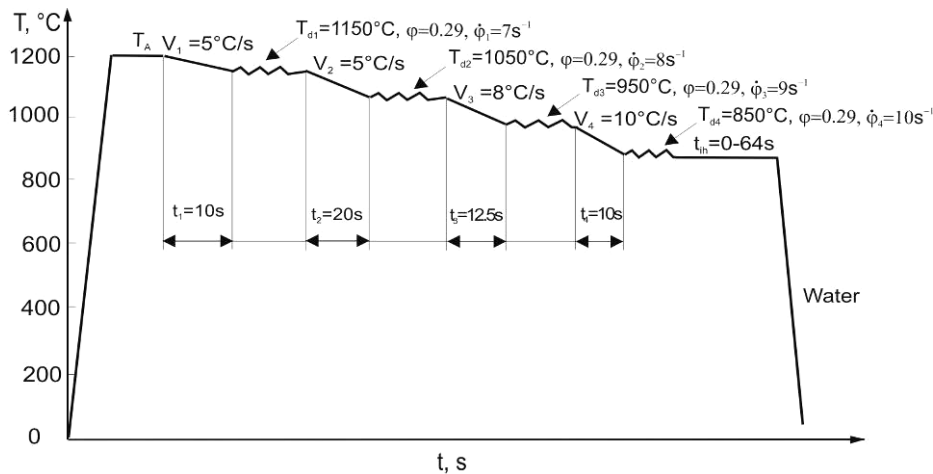

Fig. 1. Scheme of the several-stage axisymmetrical compression test

Metallographic tests of samples along with the determination of grain size and portion of recrystallized austenite were performed on LEICA MEF4A optical microscope. The fraction of recrystallized austenite was metallographically defined in the distance of 1/3 of radius from a centre of the sample. In order to reveal the austenitic structure, samples were etched in an aqueous solution of nitric and hydrochloric acids. The identification of phase composition of the steel in the initial state and after thermo-mechanical processing was achieved by using X-ray qualitative phase analysis with help of X'Pert PRO diffractometer and X'Celerator strip detector. The lamp with Co anode working at 40 kV voltage and 30 mA current was used.

3. Results and discussion

In contradistinction to steel with similar chemical composition [16], elaborated steel has a $\gamma + \varepsilon$ microstructure in the initial state (Figure 2). The presence of ε martensite can be a result of increased concentration of Si in relation to Al, oppositely influencing SFE of austenite. Martensite lamellas ε are present also after solutioning from a 800–1100 °C temperature range. Up to 1000 °C steel still keeps its diphase fine-grained microstructure (Figure 3). After solutioning from 1100 °C the grain size of austenite increases (Figure 4). Numerous annealing twins can be observed.
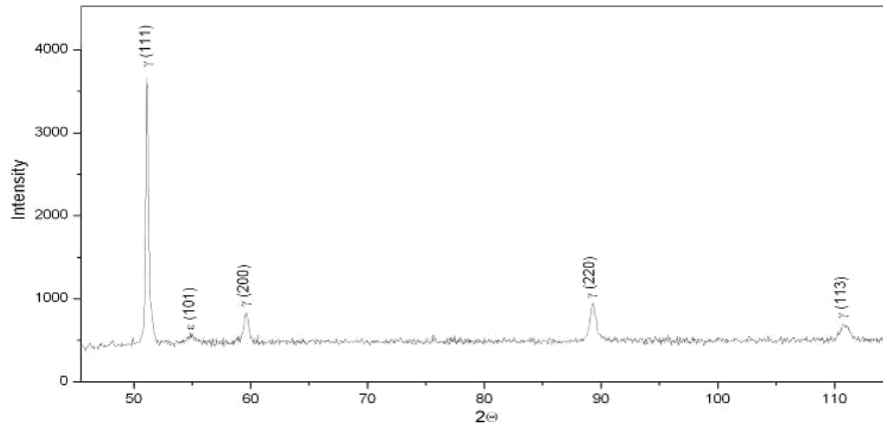
Fig. 2. X-ray diffraction pattern of the investigated steel in the initial state
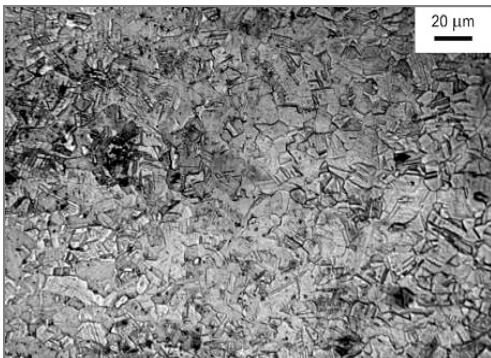

Fig. 3. Fine-grained structure of the steel solution heat-treated from a temperature of 1000 °C
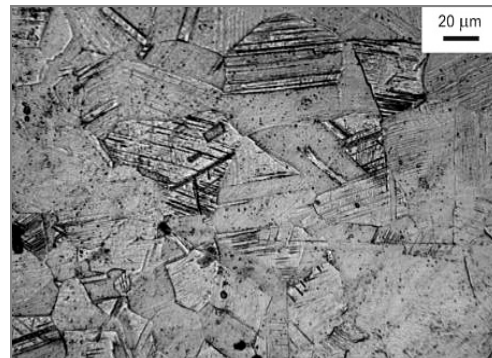

Fig. 4. Coarse-grained structure of the steel solution heat-treated from a temperature of 1100 °C

The change of grain size in function of annealing temperature is shown in Figure 5. Up to 900 °C steel possesses fine-grained microstructure with grain sizes equal around 12 μm. In the temperature of 1000 °C grain size slightly increases to 18 μm, and successively, more intense increase of austenite grain size occurs. This behaviour is connected to the temperature stability of MX-type interstitial phases.

Basing on calculations deriving from the dependence (1), it can be stated that the first phase precipitating in the austenite in dendritic spaces will be TiN, independent on the constants A and B given in [15]. Taking into account atomic weights for Ti and N, it is possible to calculate the concentration of titanium needed for fixing the total nitrogen concentration. Concentration of titanium fixing nitrogen equals: 3.4x %wt. N = 0.013% Ti. Subtracting this value from the concentration of Ti in the steel we have: 0.075% – 0.013% = 0.063%wt. Ti, what means the titanium concentration to be used for fixing C in a lower temperature range.
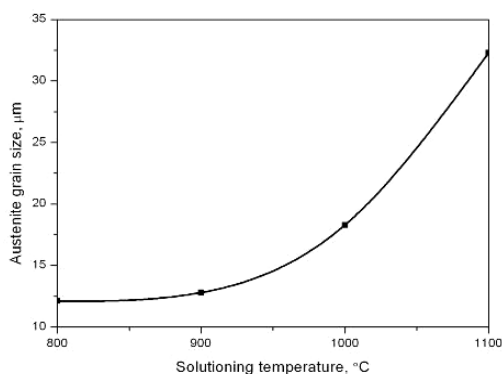
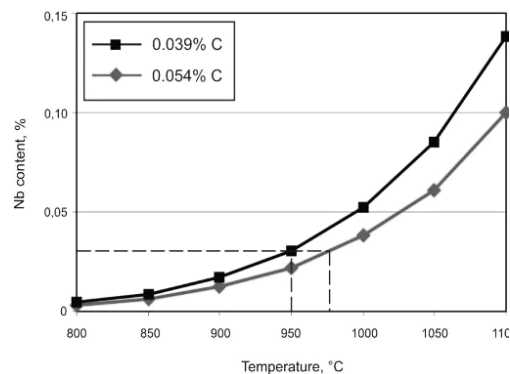Fig. 5. Influence of the solutioning temperature on a grain size of austenite

Fig. 6. Solubility curves of NbC for carbon content of 0.054% and 0.039% (A = 7290, B = 3.04)

Titanium will precipitate in a form of TiC, and what is more probable, as Ti (C, N), what was observed in [13, 15]. In order to calculate the weight percentage of carbon needed for fixing the remaining titanium concentration we have to take into account atomic weight for Ti and C and also that for TiC one titanium atom is fixed by one carbon atom. Therefore wt.% C fixed by Ti into TiC = 0.063wt.%/4 = 0.015wt.% C. Hence, the carbon content combined in TiC is equal around 0.015%. According to that, solubility curves of NbC for 0.054% of carbon concentration in the steel and reduced by concentration needed for titanium combining (0.054% − 0.015% = 0.039%) were determined (Figure 6). The values of $A = 7290$ and $B = 3.04$ given in [17] were used. Constants A and B are connected with the free energy of compound formation and also depend on a method of their determination (sedimentary precipitation, gas equilibrium, thermodynamic calculations). Hence, in the literature different values can be found [15, 18]. A result of the substituting the carbon concentration into the Equation (1) for various temperatures is the concentration of Nb dissolved in solid solution. After taking into account the total niobium concentration in the investigated steel, it arises from the Figure 6 that the temperature range of NbC dissolution is from about 975 to 850 °C. The calculations carried out for different values of A and B give very comparable results. The dissolution of NbC explains more meaningful grain growth of the steel after increasing temperature to above 1000 °C (Figure 5).

The influence of microadditions explains also indirect the presence of ε martensite in microstructure of the steel. Because of full nitrogen concentration and high concentration of carbon bounding into stable interstitial phases, these elements lead to decrease of SFE and decreasing austenite stability during cooling. However, it should be pointed out that also different view on the role of Nb influence in high-manganese steels can be found [16].

Fig. 7. Structure of the steel solution heat-treated
from 850 °C after 40% deformation

Fig. 8. Structure of the steel solution heat-treated
from 1000 °C after 40% deformation

Fig. 9. Metadynamically recrystallized structure of
steel solution heat-treated from 1000 °C after 40%
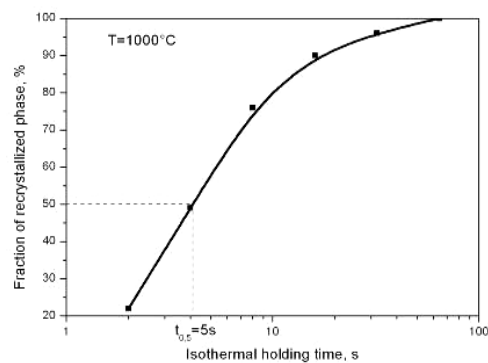deformation and isothermal holding for 4 s

Fig. 10. Evolution of the fraction of metadynamically
recrystallized grains as a function of isothermal holding
of specimens 40% deformed at 1000 °C

Upsetting tests proved that at 850 °C dynamic recrystallization controls the course of work-hardening after 40% deformation (Figure 7). Similarly, with increasing the deformation temperature to 1000 °C fine dynamically recrystallized grains located on boundaries of elongated dynamically recovered grains can be observed (Figure 8). Isothermal holding leads to microstructure refinement due to metadynamic recrystallization (Figure 9). From Figure 10 arises that at 1000 °C the course of half-recrystallization requires only about 5 s.

The curves of several-stage compression shown in Figure 11 allow identification of processes that control work-hardening of investigated steel in the whole temperature range of hot-working. The values of flow stress successively increase together with the decrease of deformation temperature.
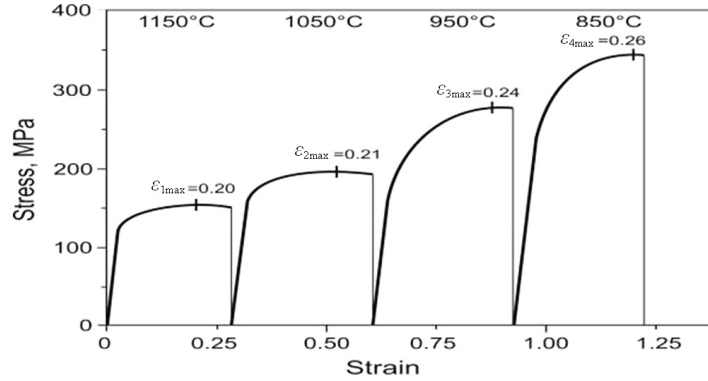
Fig. 11. Stress - strain curves corresponding to the hot-working conditions in Figure 1

Deformation peaks corresponding to the maximal values of flow stress show that during deformation dynamic recrystallization begins. The values of ε_{max} are equal 0.2, 0.21, 0.24 and 0.26, respectively – adequately to 1150, 1050, 950 and 850 °C temperatures. These strain values are possible to achieve during rolling which in a large degree should contribute to obtaining fine-grained microstructure of products. In the intervals between deformations, the metadynamic recrystallization should occur.

Directly after the end of last deformation and water solutioning, steel possesses microstructure with dynamically recovered elongated grains and dynamically recrystallized fine grains (Figure 12). The fraction of ε martensite yielded to a meaningful decrease in relation to the initial state, what is indicated by weak intensity of peaks coming from this phase. The steel holding at 850 °C leads to the microstructure refinement.
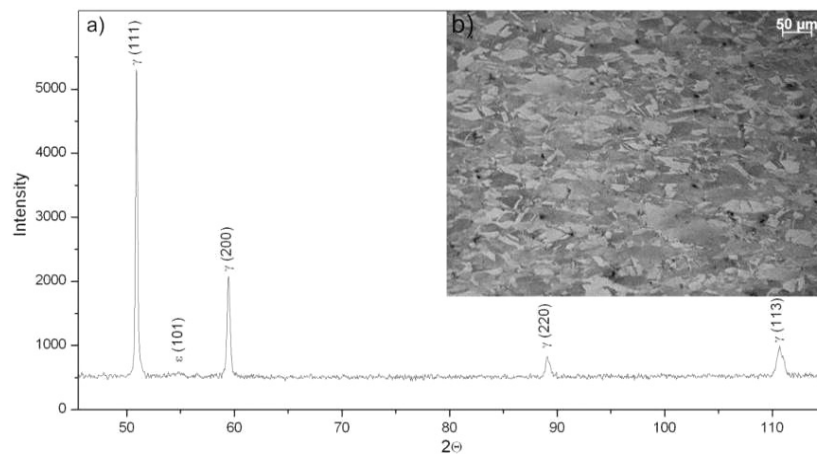

Fig. 12. X-ray diffraction pattern (a) and the structure (b) of the steel solution heat-treated from a temperature of 850 °C directly after the last deformation cycle
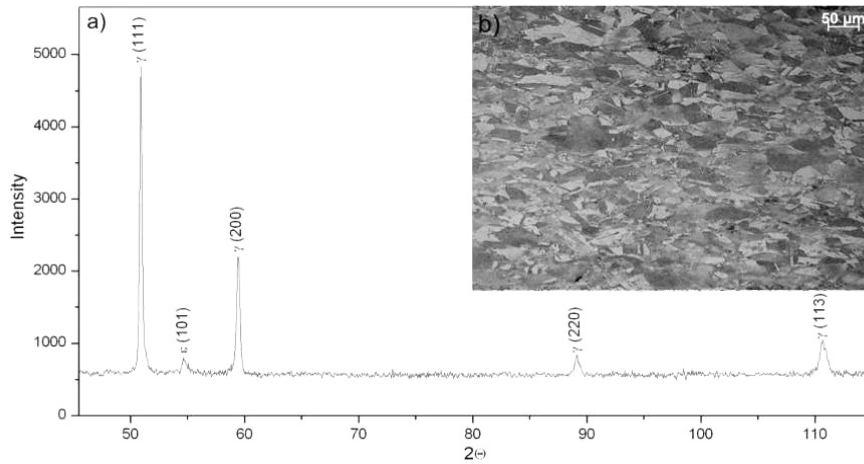
Fig. 13. X-ray diffraction pattern (a) and the structure (b) of the steel solution heat-treated from
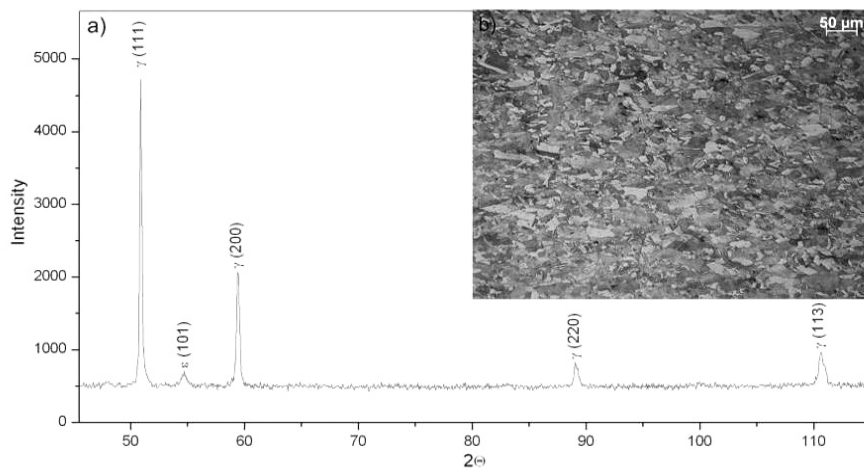a temperature of 850 °C after isothermal holding of the specimen for 32 s

Fig. 14. X-ray diffraction pattern (a) and the structure (b) of the steel solution heat-treated from
a temperature of 850 °C after isothermal holding of the specimen for 64 s

Figure 13 presents the microstructure of steel held in 850 °C for 32 s with fraction of metadynamically recrystallized grains equal around 40%. Slower progress of recrystallization in comparison with the curve of recrystallization kinetics presented in Figure 10 is a result of lower deformation temperature and smaller reduction. Increase of holding time of the steel in 850 °C results with growth of metadynamically recrystallized grains (Figure 14). Whereas dynamically recovered grains haven't yielded to the end of static recrystallization yet. X-ray diffraction patterns in Figures 12a–14a show that the steel maintains its $\gamma + \varepsilon$ microstructure.

4. Conclusions

Developed steel is characterized with $\gamma + \varepsilon$ diphase microstructure. Essential influence on the presence of ε martensite have Nb and Ti microadditions causing decrease of stacking fault energy of γ phase, fixing nitrogen and carbon. The calculations concerning the dissolution kinetics of NbC and TiN as a function of temperature indicate on hampering influence of these particles on a grain growth of the steel during its austenitizing and hot-working. It is confirmed by a fine-grained structure of the specimen solution heat-treated from a temperature of 1000 °C. Upsetting tests proved that after applying 40% reduction at 850 and 1000 °C dynamically recrystallized grains are located on boundaries of elongated dynamically recovered grains. Application of 25% reduction during the several-stage axisymmetrical compression test causes that dynamic recrystallization is the process controlling strain hardening in the whole applied temperature range of deformation. Isothermal holding of the steel in 850 °C after the end of deformation creates a possibility of further microstructure refinement through metadynamic and static recrystallization. The time of half-recrystallization of austenite in this temperature is equal around 35 s.

References

[1] Hadasik E. (red.): *Przetwórstwo metali. Plastyczność a struktura*, Wydawnictwo Politechniki Śląskiej, Gliwice, 2006.

[2] Ehrhardt B., Berger T., Hofmann H., Schaumann T.W.: *Property related design of advanced cold rolled steels with induced plasticity*, Steel Grips, Vol. 2, No. 4, 2004, pp. 247–255.

[3] Zackay V.F., Parker E.A., Fahr D., Busch R.: Trans. ASM, Vol. 60, 1967, pp. 252–259.

[4] Frommeyer G., Brüx U., Neumann P.: *Supra-ductile and high-strength manganese-TRIP/TWIP steels for high energy absorption purposes*, ISIJ International, Vol. 43, No. 3, 2003, pp. 438–446.

[5] Frommeyer G., Drewes E.J., Engl B.: *Physical and mechanical properties of iron-aluminium-(Mn, Si) lightweight steels*, La Revue de Metallurgie, No. 10, 2000, pp. 1245–1253.

[6] Vercammen S., Blanpain B., De Cooman B.C.: *Mechanical behaviour of an austenitic Fe-30Mn-3Al-3Si and importance of deformation twinning*, Acta Materialia, Vol. 52, 2004, pp. 2005–2012.

[7] Allain S., Chateau J.P., Bouaziz O., Migot S., Guelton N.: *Correlations between the calculated stacking fault energy and the plasticity mechanisms in Fe-Mn-C alloys*, Materials Science and Engineering A, Vol. 387–389, 2004, pp. 158–162.

[8] Hamada A.S., Karjalainen L.P., Somani M.C.: *The influence of aluminium on hot deformation behaviour and tensile properties of high-Mn TWIP steels*, Materials Science and Engineering A, Vol. 467, 2007, pp. 114–124.

[9] Niewielski G., Hetmańczyk M., Kuc D.: *Wpływ struktury wyjściowej i warunków odkształcania na właściwości stali austenitycznych odkształcanych na gorąco*, Inżynieria Materiałowa, Vol. 24, No. 6, 2003, pp. 795–798.

[10] Dobrzański L.A., Grajcar A., Borek W.: *Hot-working behaviour of high-manganese austenitic steels*, Journal of Achievements in Materials and Manufacturing Engineering, Vol. 31, No. 1, 2008, pp. 7–14.

[11] Grajcar A., Borek W.: *Thermo-mechanical processing of high-manganese austenitic TWIP-type steels*, Archives of Civil and Mechanical Engineering, Vol. 8, No. 4, 2008, pp. 29–38.

[12] Dobrzański L.A., Grajcar A., Borek W.: *Influence of hot-working conditions on a structure of high-manganese austenitic steels*, Journal of Achievements in Materials and Manufacturing Engineering, Vol. 29, 2008, pp. 139–142.

[13] Adamczyk J., Grajcar A.: *Structure and mechanical properties of DP-type and TRIP-type sheets obtained after the thermo-mechanical processing*, Journal of Materials Processing Technology, Vol. 162–163, 2005, pp. 267–274.

[14] Korchynsky M.: *Advanced metallic structural materials and a new role for microalloyed steels*, Inżynieria Materiałowa, Vol. 140, No. 3, 2004, pp. 152–158.

[15] Gladman T.: *The physical metallurgy of microalloyed steels*, The Institute of Materials, The University Press, Cambridge, 1997.

[16] Huang B.X., Wang X.D., Rong Y.H., Wang L., Jin L.: *Mechanical behaviour and martensitic transformation of an Fe-Mn-Si-Al-Nb alloy*, Materials Science and Engineering A, Vol. 438–440, 2006, pp. 306–311.

[17] Palmiere E.J.: *Precipitation phenomena in microalloyed steels*, Proceedings of the International Conference "Microalloying'95", Pittsburgh, PA, USA, 1995, pp. 307–320.

[18] Adamczyk J.: *Inżynieria wyrobów stalowych*, Wydawnictwo Politechniki Śląskiej, Gliwice, 2000.

Acknowledgement

Wpływ warunków obróbki plastycznej na gorąco na strukturę stali wysokomanganowej

Stale wysokomanganowe o strukturze austenitycznej należą do grupy nowoczesnych stali przewidzianych do zastosowania w przemyśle motoryzacyjnym. Opracowano skład chemiczny stali zawierającej 25% Mn, umacnianej roztworowo przez Si i Al. Mikrododatki Nb i Ti wprowadzone do stali, tworząc stabilne azotki i węgliki powinny powodować umocnienie wydzieleniowe i hamować rozrost ziaren austenitu zrekrystalizowanego. Celem pracy było określenie wpływu zmiennych warunków obróbki plastycznej na gorąco na strukturę badanej stali. Zidentyfikowano procesy kontrolujące umocnienie odkształceniowe i usuwające umocnienie po zakończeniu obróbki plastycznej na gorąco. Przeprowadzono wstępne spęczanie w temperaturach 850 i 1000 °C przy użyciu prasy mimośrodowej, stosując stopień gniotu w zakresie od 20 do 60%. Na podstawie wyznaczonych warunków przeprowadzono kilkustopniowe próby ściskania osiowosymetrycznego zapewniające uzyskanie drobnoziarnistej struktury austenitu.

A study on thermal behaviour of curved steel box girder bridges considering solar radiation

S.-H. KIM, K.-I. CHO, J.-H. WON
Yonsei University, 262 Seonsagnno, Seodaemun-gu, Seoul 120-749, Korea

J.-H. KIM
Seunghwa Engineering & Construction Co., Ltd., Seunghwa Bldg., 41 Machon-Dong, Songpa-Gu, Seoul 138-120, Korea

Solar radiation induces non-uniform temperature distribution in the bridge structure depending on the shape of the structure and shadows cast on it. Especially in the case of curved steel box girder bridges, non-uniform temperature distribution caused by solar radiation may lead to unusual load effects enough to damage the support or even topple the whole curved bridge structure if not designed properly. At present, it is very difficult to design bridges in relation to solar radiation because it is not known exactly how varying temperature distribution affects bridges; at least not specific enough for adoption in design. Standard regulations related to this matter are likewise not complete. In this study, the thermal behavior of curved steel box girder bridges is analyzed while taking the solar radiation effect into consideration. For the analysis, a method of predicting the 3-dimensional temperature distribution of curved bridges is used. It uses a theoretical solar radiation energy equation together with a commercial FEM program. The behavior of the curved steel box girder bridges is examined using the developed method, while taking into consideration the diverse range of bridge azimuth angles and radii. This study also provides reference data for the thermal design of curved steel box girder bridges under solar radiation, which can be used to develop design guidelines.

Keywords: *solar radiation, curved bridge, non-uniform temperature distribution, heat transfer, thermal behaviour*

1. Introduction

Bridges are continuously exposed to varying temperature conditions due to atmospheric temperature changes and solar radiation. Atmospheric temperature changes act upon the entire bridge structure, and are thus, relatively easy to consider in design. Solar radiation, however, causes non-uniform temperature distribution in the bridge structure depending on the shape of the structure and the shadows cast on it. In the cases of the curved steel box girder bridges, non-uniform temperature distribution caused by solar radiation may induce critical conditions when combined with other loads. Although most recent investigations have focused on the behaviours of curved bridges [1–6], theoretical analyses including thermal load are rare in previous literature. This study, therefore, analyzes the thermal behaviour of curved bridges in relation to solar radiation, in order to evaluate its effects and use the results as reference data in developing design guidelines for curved bridges.

In the analysis of the thermal behaviour of curved steel box girder bridges, temperature distribution must be defined through a heat transfer analysis. However, the 3-dimensional heat transfer analysis of a large structure such as a curved steel box girder bridge can be quite complicated, especially when regarding solar radiation. In this study therefore, a simplified method was developed to predict the temperature distribution of curved bridges, using a theoretical solar radiation energy equation combined with a commercial FEM program. Based on the developed temperature predicting method and the chosen solar radiation condition, a 3-D structural analysis is carried out to determine the effects of temperature on the curved bridges. In order to calculate the worst condition that can be brought forth by solar radiation, its most unfavourable condition is examined based on a statistical analysis of the observation data recorded by the Korea Meteorological Administration [7]. Structural responses are evaluated systematically with diverse bridge directions, radii, span lengths and support conditions of curved bridges.
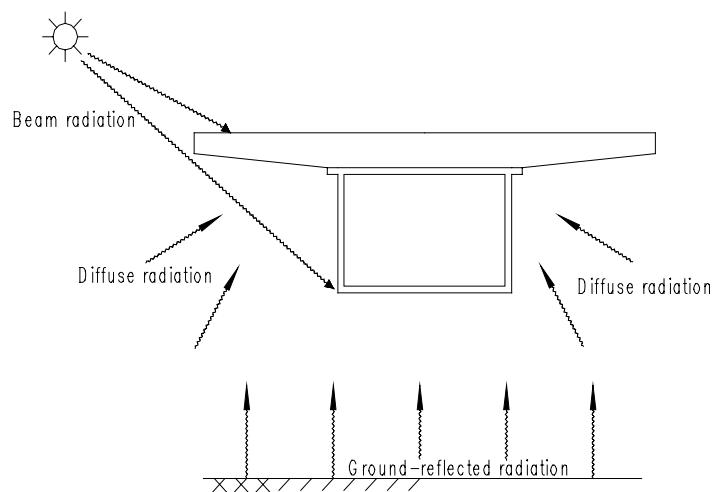

Fig. 1. Solar radiation

2. Calculation of solar radiation energy

Solar radiation is radiant energy emitted by the sun throughout the atmosphere. It can be categorized into three components, namely beam, diffuse and ground-reflected radiation, as shown in Figure 1. Beam radiation, the major component of solar radiation, is the solar radiation received from the sun not scattered by the atmosphere. It is often referred to as direct solar radiation. Diffuse radiation is the solar radiation received from the sun after its direction was changed by the atmosphere through a process of scattering. This makes things, even indoors, visible without direct sunlight. Ground-reflected radiation is radiation reflected from the ground cover and bodies of

water on the surface of the earth. While beam radiation is the major component causing non-uniform temperature distribution in the bridge, diffuse and ground-reflected radiation are not negligible.

An equation has been presented by Duffie and Beckman [8] to calculate the total solar radiation of a tilted surface in terms of beam, diffuse and ground-reflected radiation as follows:

$$I_t = I_b \frac{\cos \theta}{\cos \theta_z} + I_d \left(\frac{1 + \cos \beta}{2} \right) + I\rho \left(\frac{1 - \cos \beta}{2} \right), \tag{1}$$

where:

I_t is the total solar radiation on a tilted surface,

I_b is the beam solar radiation on a horizontal surface,

I_d is the diffuse radiation on a horizontal surface,

I is the horizontal total solar radiation ($I_b + I_d$),

β is the slope, that is, the angle between the plane surface in question and the horizontal,

ρ is the diffuse ground reflection,

θ is the angle of incidence (the angle between the beam radiation on a surface and the normal to that surface),

θ_z is the zenith angle. This study refers to the literature of Duffie and Beckman [8] to decide the diffuse ground reflection ($\rho = 0.2$).
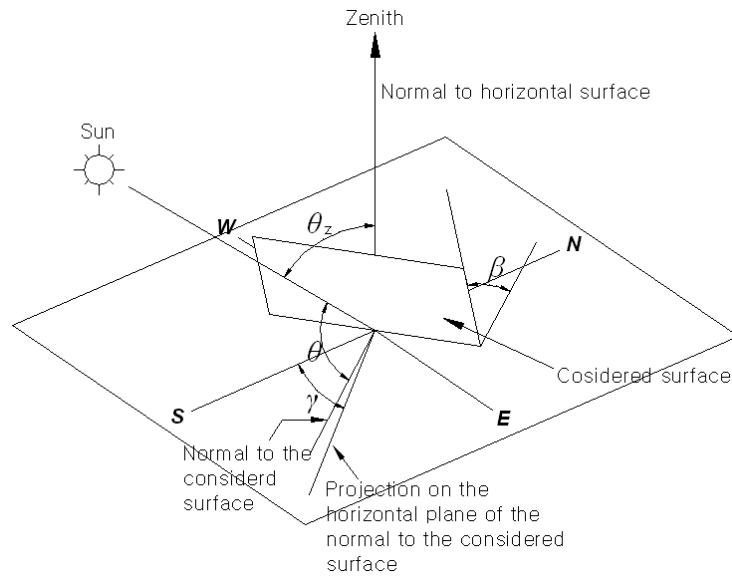

Fig. 2. Relationship between the inclined surface and the zenith angle

An Equation relating the angle of incidence of beam radiation on a surface, θ, to the other angles (Figure 2) is

$$\cos\theta = \sin\delta\sin\phi\cos\beta - \sin\delta\cos\phi\sin\beta\cos\gamma + \cos\delta\cos\phi\cos\beta\cos\omega$$
$$+ \cos\delta\sin\phi\sin\beta\cos\gamma\cos\omega + \cos\delta\sin\beta\sin\gamma\sin\omega, \tag{2}$$

where:

ϕ is the latitude of a surface ($-90^\circ \le \phi \le 90^\circ$),

δ is the declination (the angular position of the sun at solar noon; $-23.45^\circ \le \delta \le 23.45^\circ$),

γ is the surface azimuth angle (the deviation of the projection on a horizontal plane of the normal to the surface from the local meridian, with due south, ease negative, and west positive; $-180^\circ \le \gamma \le 180^\circ$),

ω is the hour angle (the angular displacement of the sun east or west of the local meridian due to rotation of the earth on its axis at 15° per hour, morning negative, afternoon positive). In Equation (2), the declination can be found from the Equation of Cooper [9]:

$$\delta = 23.45\sin\left(360 + \frac{284 + n}{365}\right), \tag{3}$$

where

n is the total date from 1st of January.

To calculate the diffuse radiation in Equation (1), the following Equation can be used [10].

$$\frac{I_d}{I} = \begin{cases} 1.0 - 0.248k_T & \text{for} \quad k_T < 0.35 \\ 1.557 - 1.84k_T & \text{for} \quad 0.35 < k_T < 0.75, \\ 0.177 & \text{for} \quad k_T > 0.75 \end{cases} \tag{4}$$

where:

k_T is the hourly cleaness index. It is can be defined:

$$k_T = \frac{I}{I_0}. \tag{5}$$

The solar radiation I_0 in Equation (5) can be given by following Equation:

$$I_0 = G_{SC}\left(1 + 0.33\cos\frac{360n}{365}\right)\cos\theta_z, \tag{6}$$

where:

G_{SC} is the lolar constant,

n is the day of the year.

Finally, the energy gain of a structure subjected to solar radiation can be calculated as follows:

$$q_s = aI_t, \tag{7}$$

where:

q_s is the energy gain due to solar radiation,

a is the solar radiation absorptivity,

I_t is the total solar radiation on inclined surface calculated by Equation (1). The solar radiation absorptivity, which is a value between 0 and 1, is assumed in this study to be 0.8 for steel box girders and 0.9 for asphalt pavement, according to Dilger et al. [11] and Siegel and Howell [12], respectively.

3. Heat transfer analysis of a curved bridge

The energy gain due to solar radiation on structural members of a straight bridge can easily be calculated using Equation (1–7), since each member keeps the same tilting amount. In the case of curved bridges, however, this process is not applicable since the angle of incidence of the beam radiation and the shadowed area generally cast by the overhang vary from section to section. Thus, it is very difficult, if not impossible, to calculate the exact energy gain for a 3-dimensional heat-transfer analysis.

A simplified method to calculate an approximate 3-dimensional temperature distribution has been developed. It consists of three phases. First, a program entitled SEB (Solar Energy calculating program for Bridge section) was developed for calculating the energy gain for an arbitrary cross section. The SEB is used in this study to prepare the input data for the heat transfer analysis, which will be computed using a commercial FEM program. Second, a 2-dimensional FEM is performed using the input data from the first phase, from which the temperature distribution of a cross section may be acquired. Third, the 2-dimensional temperature distribution is expanded into 3-dimensional temperature distribution by assuming that no heat is transferred longitudinally between neighbouring cross sections. This assumption was made based on the fact that, if the longitudinal distance between the neighbouring cross section is small, then the temperature difference is negligible. If the longitudinal heat transfer can be neglected, the computation of the 3-dimensional temperature distribution becomes a 2-dimensional problem; that is, 3-dimensional temperature distribution can be obtained by interlinking the 2-dimensional heat transfer analysis results of the reference cross sections. The feasibility of this procedure was verified using the monitoring data of an existing bridge and was presented by Cho et al. [13].

3.1. Heat transfer analysis of a cross section

The SEB is based on Equation (1–7), which indicate that variables such as zenith, and incidence angle, etc. need to be inputted. The zenith and incidence angle are considered in order to calculate the magnitude of beam radiation, while the slope of the surface is used to evaluate diffuse and ground-reflected radiation. From the input data, the SEB calculates the solar radiation energy of a cross section, taking into consideration the shaded area and area exposed to direct solar radiation, as illustrated in Figure 3.
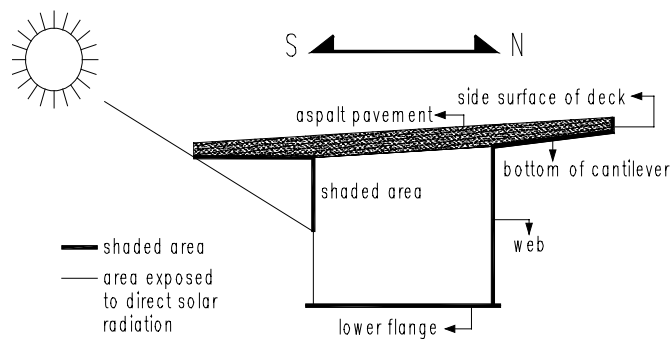
Fig. 3. Classification of faces of a cross section according to solar radiation

$$I_t = I_b \frac{\cos\theta}{\cos\theta_z} + I_d \left(\frac{1+\cos\beta}{2} \right) + I\rho \left(\frac{1-\cos\beta}{2} \right)$$

$$q_s = aI_t$$
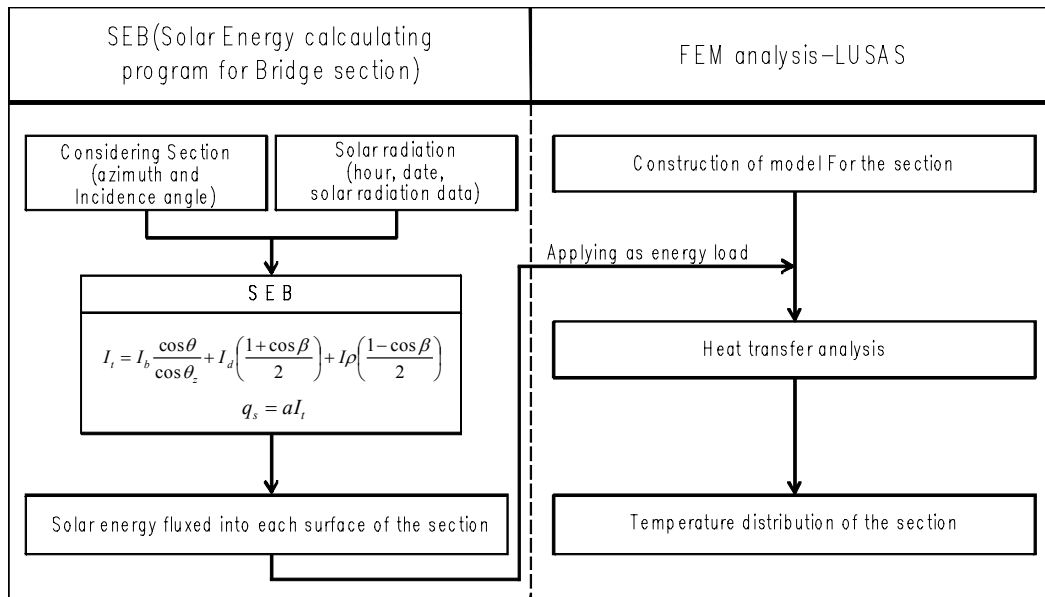
Fig. 4. Flow of calculating solar energy and predicting temperature distribution of the section

The shaded area is only affected by diffuse and ground-reflected radiation. Meanwhile, the area exposed to direct solar radiation is, additionally, affected by beam radiation. In the research of Cho et al. [13], temperature distributions in cross sections of a curved box-girder bridge were recorded for two days, and the data was compared with the temperature distributions calculated with the SEB. The measurement of temperature distributions on the surfaces exposed to the direct solar radiation coincided well with numerical results. In the case of the surfaces merely affected by direct solar radiation, the errors in numerical analyses were observed to be 2~3 °C. As the thermal behaviour of a curved bridge is mainly governed by the web exposed to direct solar radiation, the SEB can be used in the following analysis.
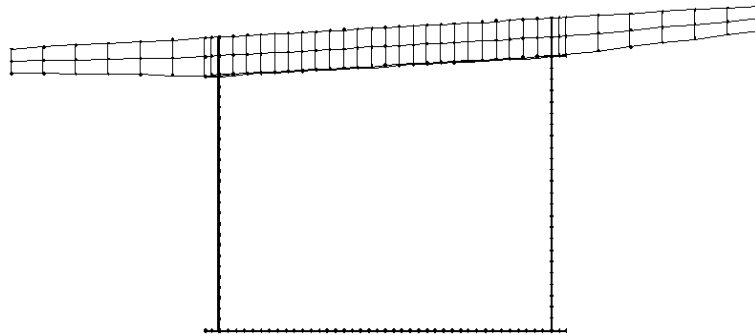
Fig. 5. Example of model of a section
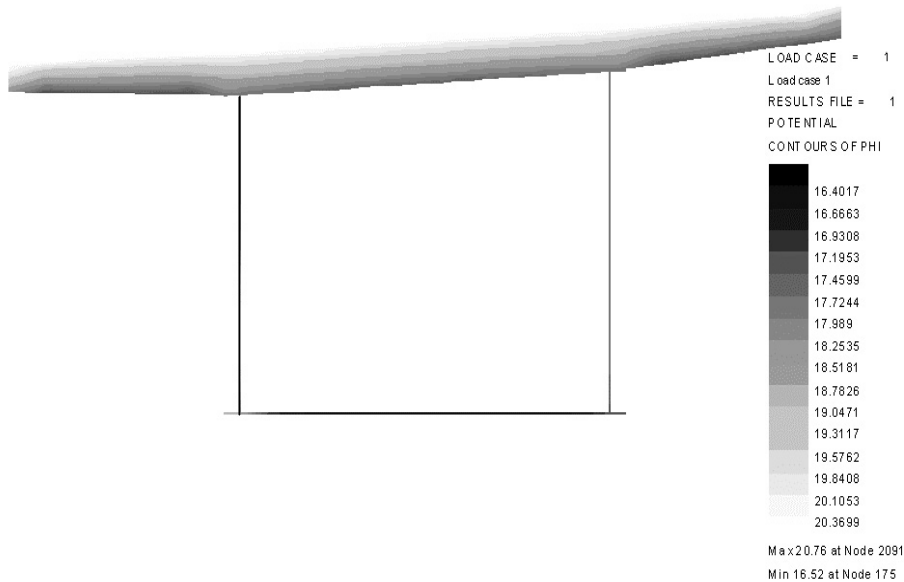
Fig. 6. Example of temperature distribution

The resultant output of the SEB, which is the energy gain due to the solar radiation of each face of the cross section, is then applied to an FEM model of the cross section for a 2-dimensional heat transfer analysis, as shown in Figure 4. A commercial FEM program, LUSAS (v.13.4), is utilized for the heat transfer analysis. The finite element model of a cross section consists of 2-dimensional heat transfer elements, called plane field elements, as illustrated in Figure 5. Figure 6 shows an example of the temperature distribution for the cross section obtained through a heat transfer analysis.

3.2. Computation of the 3-dimensional temperature distribution

Since the computation of a full 3-dimensional temperature distribution for a curved steel box girder bridge is very complicated, the negligible longitudinal heat transfer is ignored and only the 2-dimensional temperature distribution of a cross section is computed. In order to construct a 3-dimensional temperature distribution by interlinking the 2-dimensional temperature distributions of the reference cross sections, the temperature distribution of each reference cross section is required. This may require a large amount of computation. This process, however, can be simplified further by introducing the fact that the temperature distribution of a section is directly proportional to the energy input. If a single heat transfer analysis of a typical cross section has been performed and the energy input of an arbitrary cross section is determined, the temperature distribution of the other section can be obtained through a simple algebraic calculation, without any additional heat transfer analysis. Figure 7 is the 3-dimensional temperature distribution of the web obtained by expanding the 2-dimensional results.
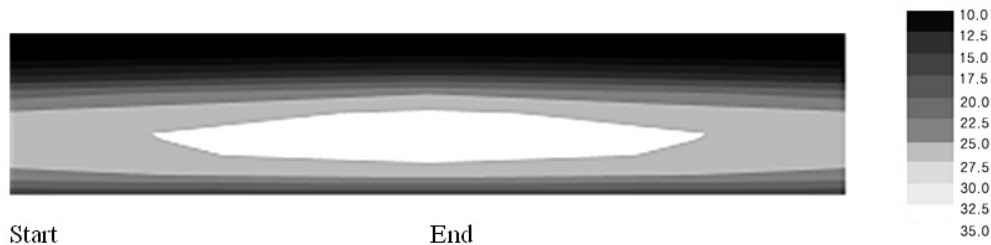

Fig. 7. Example of the temperature distribution on the web in a curved bridge

4. Thermal behaviour analysis for curved bridge

In this section, the thermal responses of the curved bridges exposed to solar radiation at various azimuth angles and radii of the curved bridges are analyzed and compared. Eight cases of azimuth angles were selected by dividing 360° into intervals of 45° as shown in Figure 8, and an analysis of the curved bridge behaviour subjected to solar radiation is performed for each case.

4.1. Solar radiation condition applied to analysis

Prior to analyzing the thermal behaviour of a curved steel box girder bridge in relation to solar radiation, a reasonable level of solar radiation intensity must be determined. First, the solar radiation data of a one-year period recorded by the Korea Meteorological Administration [6] are examined and the data from Mokpo, one of the regions with the most severe solar radiation condition in Korea, is selected. Then, the solar radiation data of Mokpo, recorded for 22 years, is collected for analysis.
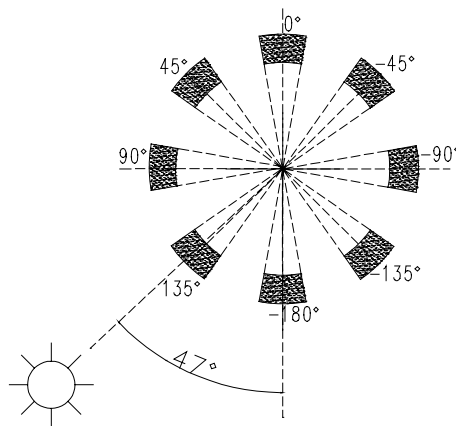
Fig. 8. Azimuth angle of curved bridges

In order to analyze the thermal behaviour of a curved bridge under a certain level of solar radiation, which can represent a state similar to that of a 'design load', the temperature change regulation specified in the Standard Specifications for Highway Bridges (AASHTO, 2002) is used as a reference since there are no specifications regarding solar radiation in any design codes. Since the AASHTO specifies the maximum temperature of a metal structure as 50 °C, the developed method for computing for the temperature distribution of the curved bridges is used to deduce the actual temperature of a general curved bridge section during the one-year period of solar radiation measurement. Based on the results, 24 days are determined to have experienced an average temperature exceeding 50 °C.

In order to acquire a set of solar radiation data with the same level of exceeding probability of the temperature regulation, 24 data sets are chosen, which could induce a severe thermal behaviour of the curved bridge. Through preliminary structural analysis, it is found that the temperature of the web is the dominant factor in thermal behaviour of the curved bridges. Based on such findings, the 24th highest average web temperature during the one-year period is found to be 30 °C. In order to simplify the analysis, the one-year period is divided into 12 periods, as in Figure 9 depending on

the solar altitude angle. The number of days in which the average temperature of the web exceed 30 °C in each period, are presented in Table 1. Finally, the worst solar radiation condition from Table 1, a solar altitude of 38.10°~40.85° and a solar radiation of 2.90 MJ/m^2, is selected for the analysis of the curved bridges exposed to solar radiation.
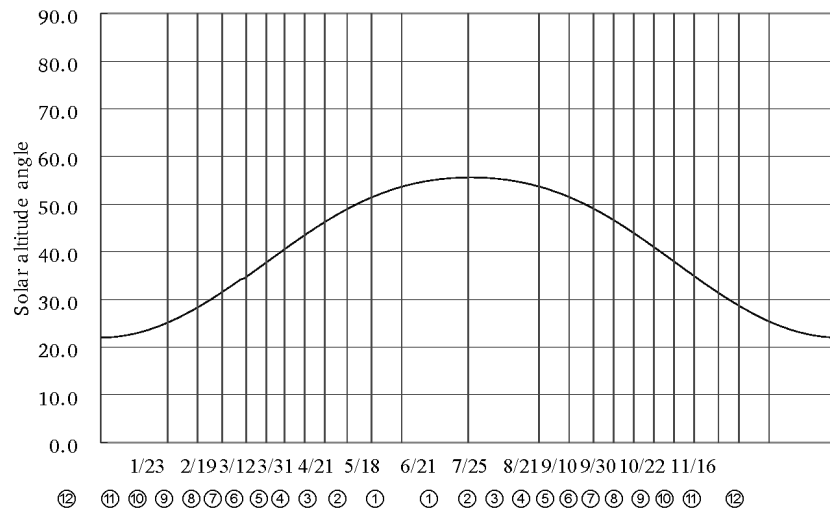

Fig. 9. Variation of solar altitude angle for one year

Table 1. Solar radiation conditions and the number of days in which the average temperature of the web exceeded 30 ºC

No.	Solar altitude angle (degrees)	Solar radiation (MJ/m$^{2)}$)	Days
1	38.10~40.85	2.90	1
2	35.04~38.10	2.53	1
3	31.81~35.04	2.13	3
4	28.61~31.81	1.90	4
5	25.32~28.61	1.68	6
6	22.38~25.32	1.47	9

4.2. Model bridges

Total of ten types of model bridges are made depending on the radius, span length and bearing setup (Table 2). The model bridges are simply supported curved box girder bridges with various span lengths of 40, 50 and 60 m. The width of the slab is 9 m and the height and width of the steel box girder are 2.5 m and 2.2 m, respectively, as shown in Figure 10. The radii of the curved bridges are 100 m, 150 m and 200 m. Two types of bearing setup are considered for each model bridge, tangential and chordal, as illustrated in Figure 11.

Table 2. Model bridges

Span length	Radius	Central angle	Bearing arrangement	Symbol
40 m	150 m	15.3º	Tangential	40-150-tan
			Chordal	40-150-chd
50 m	100 m	28.6º	Tangential	50-100-tan
			Chordal	50-100-chd
50 m	150 m	19.1º	Tangential	50-150-tan
			Chordal	50-150-chd
50 m	200 m	14.3º	Tangential	50-200-tan
			Chordal	50-200-chd
60 m	150 m	22.9º	Tangential	60-150-tan
			Chordal	60-150-chd
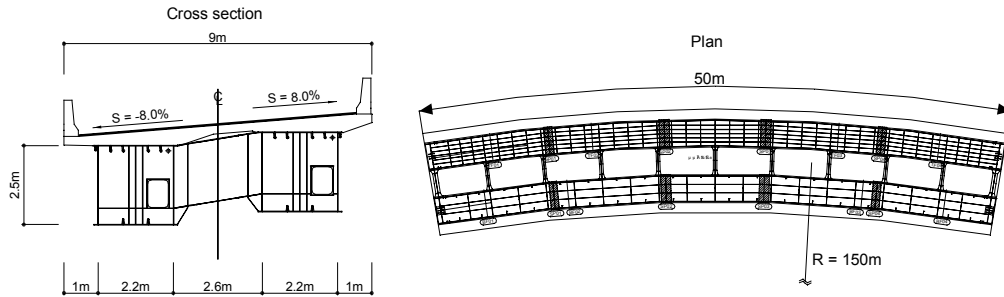
Fig. 10. Details of curved bridge (span length = 50 m, radius = 150 m)
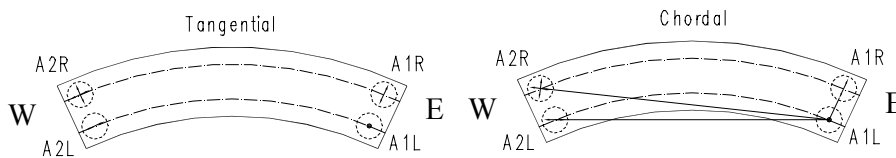
Fig. 11. Orientation of bearing guides

4.3. Thermal behaviour of curved bridges

Since the global behaviour of the curved bridge in relation to solar radiation is a major concern in this study, the reaction forces that represent the global behaviour are analyzed based on the analysis results.

4.3.1. Curved bridges with various radii

Figures 12–15 show the variation of reactions in the eight azimuth angle cases on the six types of model bridges with a span length of 50 m. Overall, the maximum reac-

tion is observed when the azimuth angle is either −45° or 135°, because the area of web subjected to beam radiation is greater than in other cases as the web directly faces the beam radiation.

(a) longitudinal reaction

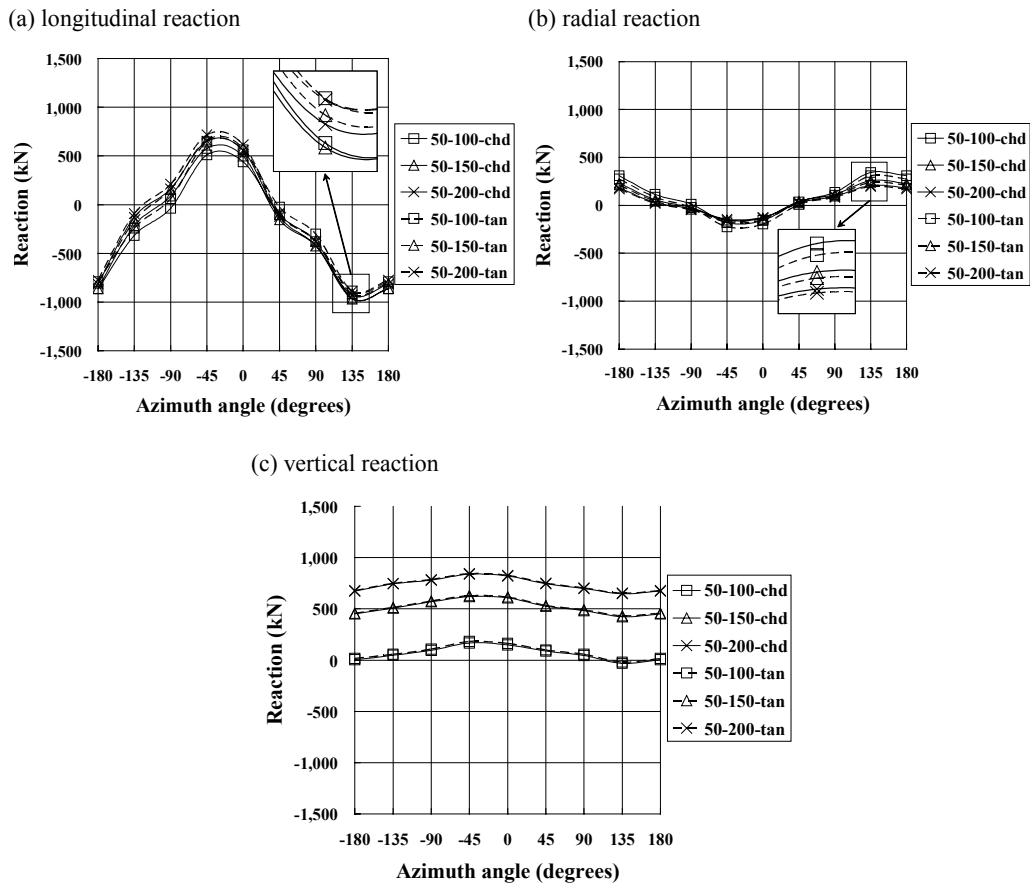(b) radial reaction

(c) vertical reaction

Fig. 12. Variation of reactions at A1L; span length = 50 m

As shown in Figures 12a and 13a, each representing the longitudinal reactions at supports A1L and A1R fixed in longitudinal direction, the maximum reaction of 960.4 kN is observed when the azimuth angle is 135°. In this case, the longitudinal reaction differs by less than 4% according to bridge radius, and 8% according to the types of bearing setup where the chordal bearing setup exhibited larger reaction. In the case where the azimuth angle is −45°, the maximum longitudinal reaction of 715.4 kN is observed, and the tangential bearing setup exhibits 20% larger reaction compared to the chordal bearing setup. Although the differences in reactions do exist due to the types of bearing setup, it is difficult to judge which type would be more advantageous since the re-

sults are dependent on solar radiation direction, etc. Thus, it would be ideal for the designer to decide the bearing setup for a specific curved bridge, considering the azimuth angle and other factors of solar radiation. Since this is a complicated work, further research is planned for the development of a simplified method or procedure that can be used in design with ease.
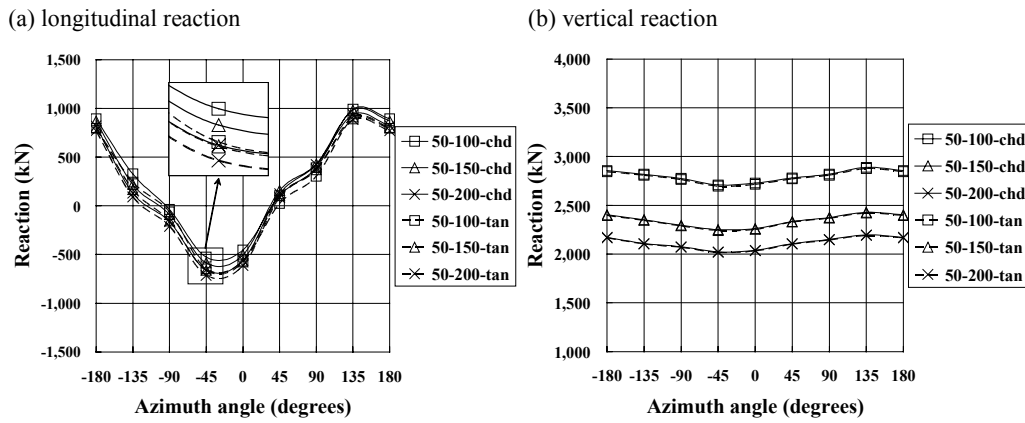
(a) longitudinal reaction

(b) vertical reaction

Fig. 13. Variation of reactions at A1R; span length = 50 m

The variation of radial reactions of A1L, as shown in Figure 12b, shows some differences according to the azimuth angle. It increases as the radius decreases where the maximum difference due to radius is 147.0 kN. On the other hand, the variation of radial reactions of A2L, as shown in Figure 14a, shows smaller differences than the A1L.

(a) radial reaction

(b) vertical reaction
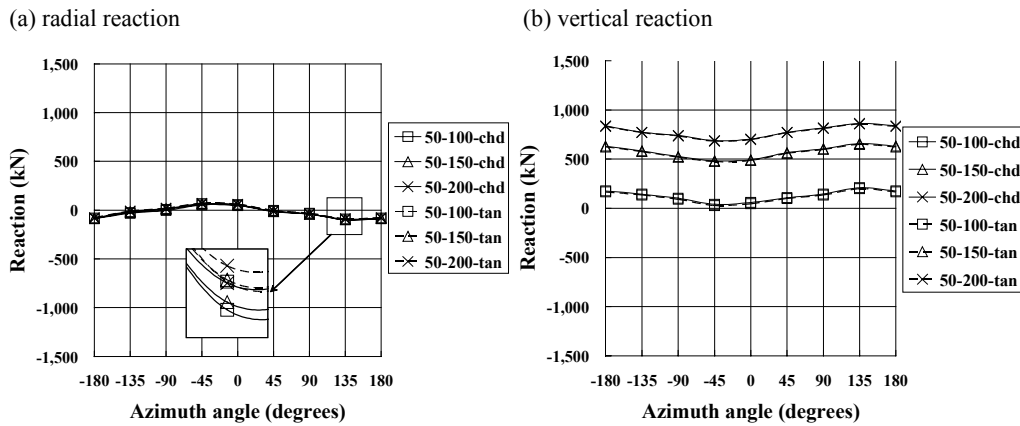
Fig. 14. Variation of reactions at A2L; span length = 50 m

Figures 12c and 14b that represent the vertical reaction of A1L and A2L show the reaction's decrease with smaller radius. As shown in Figure 12c, an uplift force of 34.3 kN develops at the A1L of the curved bridge having radius of 100 m when the azimuth angle is 135°. No uplift force is observed in the case of A2L, but the minimum vertical reaction is very small, that is only 28.4 kN. Since the uplift occurring at the inner-radius supports can cause the entire curved bridge structure to topple over, careful attention must be paid to its uplift as well as the longitudinal reactions at the supports due to the warping of the bridge caused by non-uniform temperature distribution.
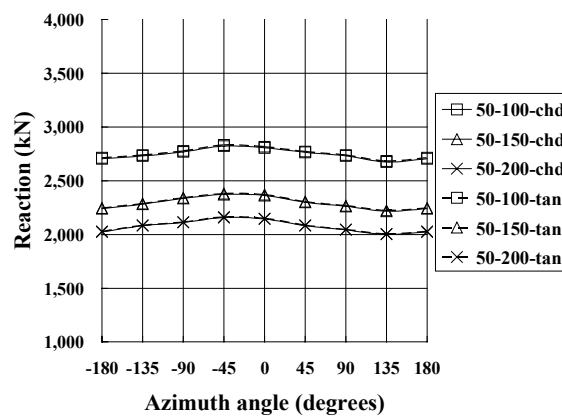
Fig. 15. Variation of vertical reactions at A2R; span length = 50 m

4.3.2. Curved bridges with various span lengths

To investigate the effect of span length to thermal behaviour of curved bridges, the six types of bridges with the same radius of 150 m are analyzed. Figures 16–19 show the variation of reactions on the bridges with the same manner as section 4.3.1. In respect of the azimuth angles, the analysis result shows a similar tendency with that of section 4.3.1, as the maximum reaction is observed when the azimuth angle is either –45° or 135°. Also, the chordal bearing setup exhibits larger reaction than the tangential bearing setup when the azimuth angle is 135° (the outer web faces south direction). On the contrary, the tangential bearing setup causes larger reaction than the chordal bearing setup when the azimuth angle is –45° (the inner web faces south direction). Moreover, the maximum values of the three kinds of reactions appear when the outer web faces south direction.

The maximum reaction of 1094.8 kN is observed when the azimuth angle is 135º at the support A1L, as shown in Figures 16a. In this case, the longitudinal reaction differs by less than 25% according to bridge radius, and 7% according to the types of bearing setup where the chordal bearing setup exhibited larger reaction.
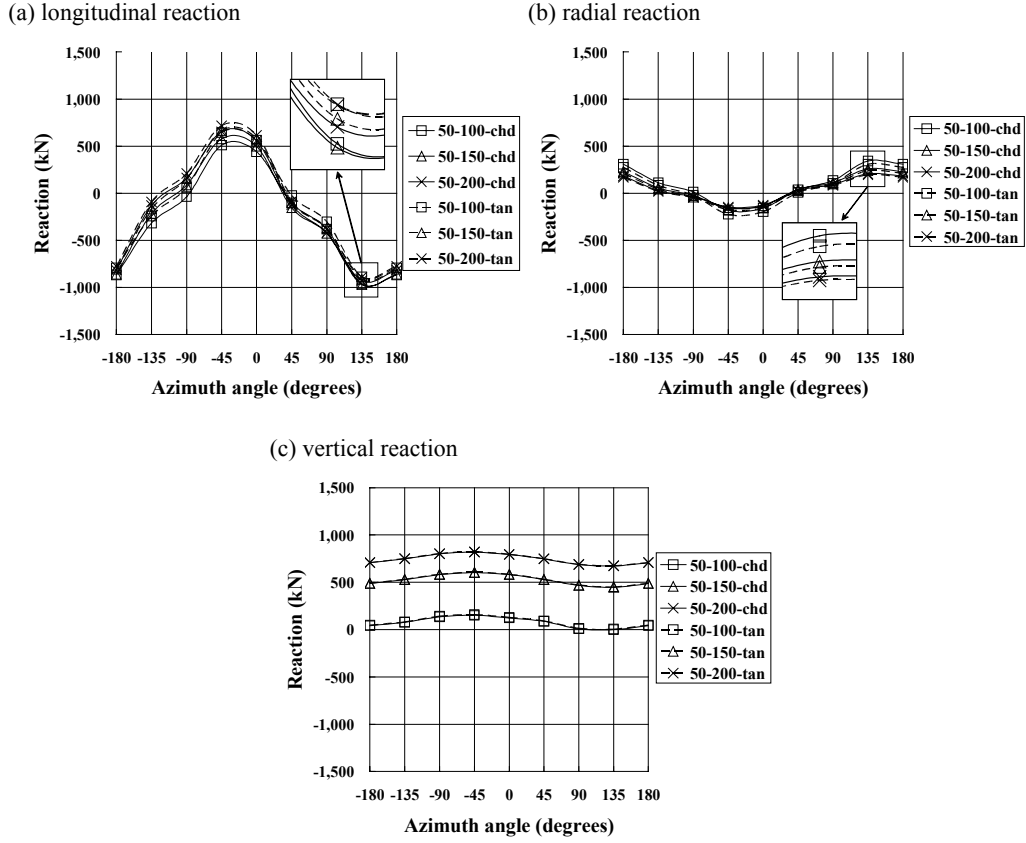
(a) longitudinal reaction

(b) radial reaction

(c) vertical reaction

Fig. 16. Variation of reactions at A1L; radius = 150 m

(a) longitudinal reaction

(b) vertical reaction

Fig. 17. Variation of reactions at A1R; radius = 150 m
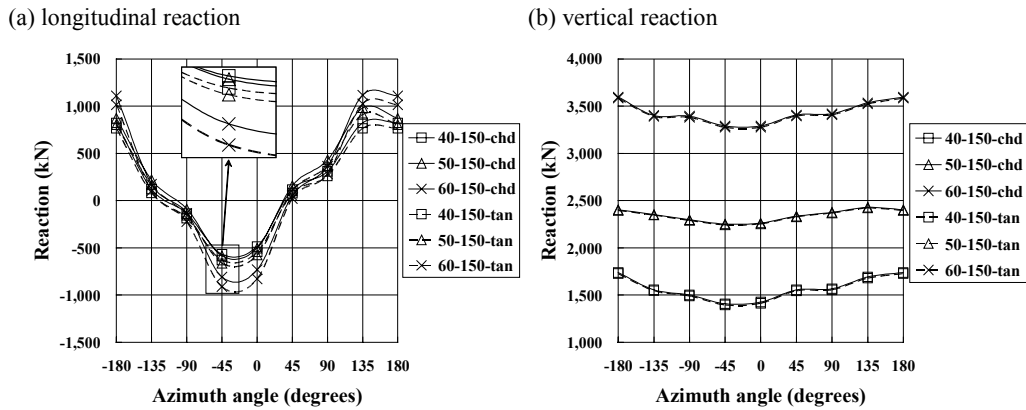
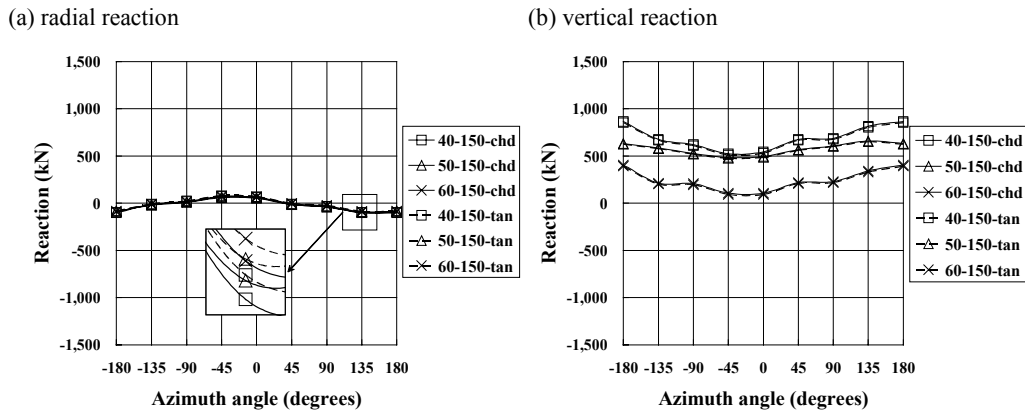(a) radial reaction   (b) vertical reaction

Fig. 18. Variation of reactions at A2L; radius = 150 m

The variation of radial reactions of A1L, as shown in Figures 16b, shows relatively large differences according to the azimuth angle than that of A2L (Figure 18a). It increases as the span length decreases where the maximum difference due to span length is 102.3 kN. The vertical reaction of A1L and A2L represented in Figures 16c and 18c decreases with larger span length. As shown in Figure 16c, an uplift force of 1.1 kN develops at the A1L of the curved bridge having span length of 60 m when the azimuth angle is 135°. Also, the minimum vertical reaction is observed in the case of A2L, which is 9.27 kN.
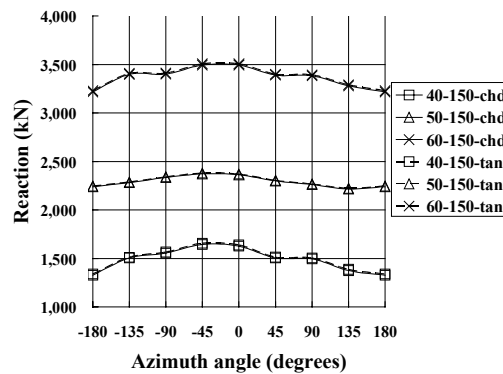

Fig. 19. Variation of vertical reactions at A2R; radius = 150 m

5. Conclusions

In this study, a method for predicting the 3-dimensional temperature distribution of curved bridges under solar radiation is applied, and the unfavourable solar radiation

conditions with lower solar altitudes and intense solar radiation were selected based on a statistical analysis of the observed data. Also, the resulting thermal behaviour of curved steel box girder bridges was analyzed considering a diverse range of bridges' directions, radii, span lengths and bearing setup directions.

1. All the reaction forces of the curved bridges increased as the radius decreased and the span length increased. Also, the chordal bearing setup exhibits larger reaction than the tangential bearing setup when the outer web faces south direction.

2. The longitudinal reaction and the uplift force were greatest in cases when the concave side of the box girder was facing south and the web was subjected to direct solar radiation. Such conditions can damage the bearings or even cause the entire curved bridge structure to topple over if not designed properly. Therefore, it is strongly suggested that the non-uniform temperature distribution brought about by solar radiation should be considered in the design of curved bridges.

Further studies will be made considering other factors and conditions not covered in this study. Three of five span continuous curved bridges will be examined as another parameter. A more detailed investigation on the stresses of local elements of curved bridges can be analyzed. Finally, a design guideline will be developed for curved bridges considering non-uniform temperature distribution of bridges.

References

[1] Siringoringo D.M., Fujino Y.: *Dynamic characteristics of a curved cable-stayed bridge identified from strong motion records*, Engineering Structures, Vol. 29, No. 8, 2007, pp. 2001–2017.

[2] Kim K., Yoo C.H.: *Effects of external bracing on horizontally curved box girder bridges during construction*, Engineering Structures, Vol. 28, No. 12, 2006, pp. 1650–1657.

[3] Kim S.-H., Lee Y.-S., Cho K.-Y.: *Analysis of horizontal reactions due to moving vehicle loads in curved bridges with varied support conditions*, Advances in Structural Engineering, Vol. 8, No. 5, 2005, pp. 529–545.

[4] Park N.-H., Choi Y.-J., Kang Y.-J.: *Spacing of intermediate diaphragms in horizontally curved steel box girder bridges*, Finite Elements in Analysis and Design, Vol. 41, No. 9–10, 2005, pp. 925–943.

[5] Koo M.-H., Lim H.-K., Kim D.-H.: *A Study on the determination of diaphragm spacing of curved steel box girders*, International Journal of Steel Structures, Vol. 4, No. 3, 2004, pp. 157–166.

[6] Maneetes H., Linzell D.G.: *Cross-frame and lateral bracing influence on curved steel bridge free vibration response*, Journal of constructional steel research, Vol. 59, No. 9, 2003, pp. 1101–1117.

[7] Korea Meteorological Administration: *http://www.kma.go.kr/intro.html*

[8] Duffie J.A., Beckman W.A.: *Solar engineering of thermal process*, 2nd Ed., John Wiley & Sons, INC., 1991.

[9] Copper P.I.: *The absorption of solar radiation in solar stills*, Solar Energy, Vol. 12, No. 3, 1969, pp. 333–346.

[10] Orgill J.F., Holland K.G.T.: *Correlation equation for hourly diffuse radiation on a horizontal surface*, Solar Energy, Vol. 19, No. 4, 1977, pp. 357–359.

[11] Dilger W.H., Beauchamp J.C., Cheung, M.S., Hali A.: *Field measurements of Moskva river bridge*, Journal of the Structural Division, Vol. 107, No. ST11, 1981, pp. 2147–2161.

[12] Siegel R., Howell J.R.: *Thermal radiation heat transfer*, 2nd ed. McGraw-Hill, 1981.

[13] Cho K.-I., Won J.-H., Kim S.-H., Lu Y.-C.: *A temperature predicting method for thermal behaviour analysis of curved steel box girder bridges*, Journal of the Korean Society for Civil Engineers, Vol. 28, No. 14, 2008, pp. 105–113 (in Korean).

Badania zachowania termicznego stalowych zakrzywionych mostów skrzynkowych poddanych promieniowaniu słonecznemu

Promieniowanie słoneczne powoduje niejednorodny rozkład temperatury w konstrukcji mostu i zależny od jego kształtu oraz padających cieni. Szczególnie w przypadku mostów zakrzywionych ze stalowych dźwigarów skrzynkowych niejednorodny rozkład temperatur wywołany promieniowaniem słonecznym może prowadzić do powstania wyjątkowych sił wystarczających do zniszczenia podpór lub nawet zniszczenia mostu, o ile jego konstrukcja nośna nie została odpowiednio zaprojektowana. Obecnie projektowanie mostów z uwzględnieniem promieniowania słonecznego jest bardzo trudne, ponieważ wpływ zmiennego rozkładu temperatury na konstrukcję mostu nie jest dokładnie znany, jak również nie jest określony sposób uwzględnienia tych wpływów w projektowaniu. Nie istnieją również żadne normy dotyczące tego zagadnienia. W pracy przedstawiono analizę zachowania mostu uwzględniającą działanie promieniowania słonecznego. Do analizy użyto metodę przewidywania trójwymiarowego rozkłady temperatury w mostach zakrzywionych w planie. W metodzie tej wykorzystane zostało teoretyczne równanie promieniowania słonecznego oraz program do analizy metodą elementów skończonych. Przeprowadzono badania zachowania mostu przy uwzględnieniu różnych zakresów kąta azymutu oraz promieni zakrzywienia mostu. Praca stanowi źródło – możliwych do wykorzystania w projektowaniu – informacji dotyczących zagadnień termicznych w mostach zakrzywionych o przęsłach ze stalowych dźwigarów skrzynkowych pod wpływem promieniowania słonecznego.

Classical inverse and metamodel approach in identification of nanomaterials properties

M. KOPERNIK, A. STANISŁAWCZYK

Akademia Górniczo-Hutnicza, al. Mickiewicza 30, 30-059 Kraków, Poland

System of nanocoatings deposited by using physical vapour deposition is planned to be applied in the artificial heart prosthesis. Material models of these coatings are necessary for numerical design of these products and are crucial for accuracy of simulations. The objective of the present work is identification of parameters of material model of nanocoatings using two methods based on the nanoindentation test data: the classical inverse analysis and the artificial neural network metamodel.

The inverse analysis is preceded by the development of FEM model dedicated to the nanoindentation test for the system of nanocoatings. The parameters of individual coating of the system are evaluated. In the second approach to decrease the computation cost, the metamodel is suggested. The metamodelling method is based on the artificial neural network technique. The achieved results confirm the usefulness of the presented solution in the identification of the material properties for the system of nanocoatings.

Keywords: *inverse analysis, metamodel, artificial neural network (ANN), multilayer perceptron neural network (MLP), finite element method (FEM)*

1. Introduction

Systems of hard nanocoatings exhibit interesting tribological and functional properties, which are difficult to achieve in conventional and homogenous materials. Hard nanocoatings are usually examined in experimental nanoindentation tests, because standard experimental methods performed in macro and micro scales are not suitable for considered example. Analytical methods for nanoindentation tests, which lead to evaluation of mechanical properties, were developed by Oliver and Pharr in [1]. A lot of problems occur in experimental nanoindentation tests. The multistage deformation is required in case of testing the system of nanocoatings. It is needed to eliminate the effect of scatter in results and to create a possibility to achieve the response of bottom coatings during repeated loading and partial unloading cycles. Despite of all these efforts and using the technologically advanced equipment, the nanoindentation test supplies force versus displacement data with meaningful big errors, which may reach 50%.

However, the experimental solutions are dedicated to monolayer materials. Therefore, the Authors of present work have undertaken some attempts towards the FEM modelling of system of nanocoatings in [2]. Their previous research was mainly focused on overcoming various difficulties, which occur in finite element simulations of nanoindentation test for system of nanocoatings. These problems arise from small

thickness of coatings, necessity of remeshing, multimaterial, multistage load/partial unload character of the test. The mentioned difficulties lead to many inconveniences, which are as follows:

I – the necessity of rescaling,

II – long computing time of each simulation,

III – generation of the fine mesh through the thickness for many coatings of the system,

IV – very fine mesh in contact region between small moving tip of indenter and comparatively big specimen.

Accuracy of the FEM simulation of the system of coatings depends on adequate evaluation of the properties of each coating, which is crucial in modelling procedure. As the result of mentioned difficulties the direct numerical model for nanoindentation test is computationally expensive. Additionally, the introduction of the classical inverse method requires numerous simulations of the indentation test. Therefore, development of the alternative, computationally effective method, based on the metamodel principle, is the key objective of the present project.

The first part of work describes the nanoindentation test for system of nanocoatings and specifies how hardness in nanoscale is measured. The next part of the paper is dedicated to the development of the efficient and robust FEM model of nanoindentation test. FEM modelling is preceded by the sensitivity analysis oriented towards the determination of parameters of material model and nanotest settings, which have the biggest influence on a response of generated FEM model.

The main objective of the present work is the inverse analysis, which in classical form allows the identification of material parameters for inner nanocoating in the system. Reaching the conformity between the standard inverse analysis using the simplex method shown in [3] (goal function based on hardness) and the experimental nanoindentation test, is the preliminary task. Previously, the proposed optimization algorithm (goal function based on force) predicted the parameters of material model of C-Mn steel in [4] using the micro-indentation test data. Because the prepared procedure was capable to determine properly material parameters, it is dedicated to the present and much more complicated problems, like identification parameters in system of nanocoatings. Finally, the modified inverse analysis is applied using the fast metamodel to avoid very high computing costs. Artificial neural network in [5] is used as metamodel and the hybrid optimization is performed, in which the genetic algorithm is set first and the Quasi-Newton algorithm in the last stage.

2. Experiment

The first task of the project is investigation of properties for system of nanocoatings, which is composed of TiAlN in [6] and TiN in [7]. These coatings are deposited on the elastic substrate – carbide using PVD (physical vapor deposition) technique. Titanium nitride is used for some particular and the most demanding applications, be-

cause it increases the biocompatibility of the covered substrate. An artificial left blood chamber and its constructional element – an aortic valve, are the examples of predicted biotechnological application in [8] of these materials, especially of TiN. The properties (Martens hardness and Young's modulus) of coatings are studied in the experimental nanoindentation tests.

2.1. Examined material

The specimen (technical material) of titanium nitride basis and mixed elastic and elastic-plastic coatings deposited on elastic substrate is investigated. The material system of seven PVD, coatings on carbide (infinite thickness) is shown in Figure 1. Two different coatings are deposited periodically. Coating 1 (TiAlN, an elastic material) is 400 nm thick and is repeated four times. Coating 2 (TiN, an elastic-plastic material) is 40 nm thick and is repeated three times.
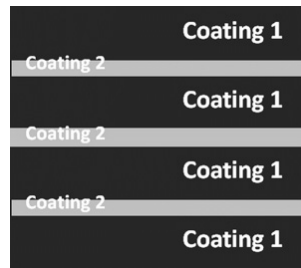

Fig. 1. System of nanocoatings

2.2. Test conditions

The objective of the nanoindentation test is to evaluate the mechanical properties of indented material like Martens hardness and Young's modulus. The experimental nanoindentation test is performed in load or depth controlled mode using a Nano Test System platform described in [9]. For the purpose of present work the 50 experimental tests were carried out, each of them had 20 stages and the final sum of indents was equal to 1000. Diamond, Berkovich pyramid (tip radius $R = 150$ nm and pyramid angle $\alpha = 70.32°$) penetrates into the specimen. The schematic illustration of experiment is shown in Figure 2 and the top view of Berkovich indent is presented in Figure 3.

The multistage process of deformation in nanoindentation test is performed in case of testing the multicoating specimen. This procedure is necessary for system of coatings to eliminate the effect of scatter in results and to create a possibility to achieve the response of bottom coatings during long-term deformation process. The indentation test supplies force versus indentation depth data. The load is the main output from the experiment and the Martens hardness is calculated for deformed material on the basis of force/displacement or depth data.
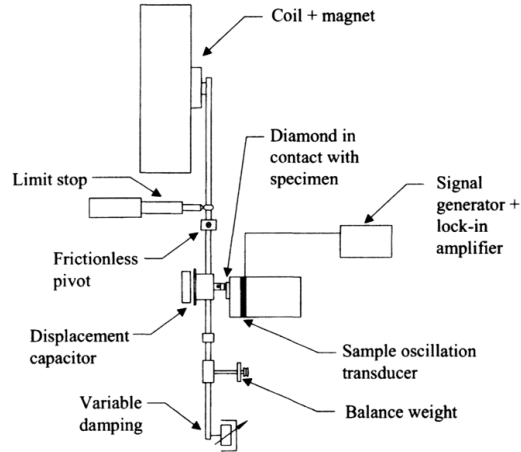
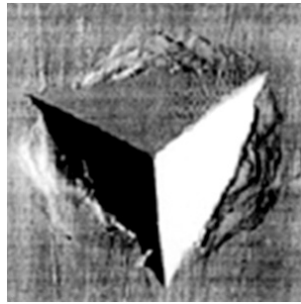Fig. 2. Schematic illustration of nanoindentation test from [9]

Fig. 3. The real view of Berkovich indent

Martens hardness HM_C for deformed single coating is defined as:

$$HM_C = \frac{F}{A_S(d)} = \frac{F}{26.43d^2},$$
(1)

where:

$A_S(d) = \frac{3\sqrt{3\mathrm{tg}\,\alpha}}{\cos\alpha} d^2 = 26.43d^2$ – indent area of Berkovich indenter,

d – depth of indent,

α – Berkovich tip angle,

F – force. Depth of the indent is measured using AFM (atomic force microscope).

Martens hardness HM_S for system of coatings can be calculated using the following Equation:

$$HM_S = \frac{1}{m^2 A_S(h)/h^2} = \frac{1}{26.43m^2},$$
(2)

where:

h – displacement of indenter,

$A_S(h) = 26.43h^2$, $m = \dfrac{h}{\sqrt{F}}$ – slope of force/displacement curve in [9],

α – Berkovich tip angle.

The calculated Martens hardness for system of nanocoatings is 23 GPa and is plotted in Figure 4. Martens hardness obtained for coating 1 is 30 GPa and Young's modulus is equal to 368 GPa.
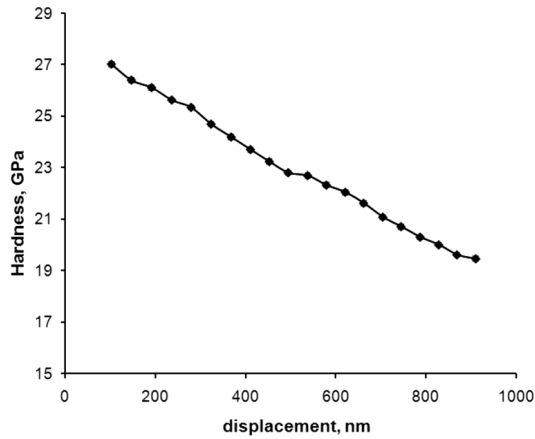

Fig. 4. Martens hardness for system of nanocoatings

3. FEM model

The Authors' research described in [2] was focused on overcoming numerical difficulties occurring in FEM simulation of nanoindentation test for system of hard coatings, which are caused by the thickness of nanocoatings, necessity of remeshing and scaling operations, as well as the multimaterial, multistage character of simulation and efforts to decrease the computing costs.

The first objective of the present work is the development of FEM model of nanoindentation test accounting for different control parameters of the test, like shape of indenter and friction conditions, as well as the sensitivity of response of the specimen with respect to parameters of material model. The selected results, which are crucial for the elaboration of efficient FEM model for nanoindentation test, are presented by the Authors.

To decrease the computing costs, the simplified 2D axisymmetric model of the nanoindentation test is considered and the Berkovich indenter is assumed as a conical one. The proposed simplified 2D model is validated through the full 3D FEM simulation of nanoindentation test in [10] and [11]. The results obtained by comparison of 2D simulation and the full 3D model are shown in Figure 5. They confirm, that simplified 2D model can be used in the further research of the present project, which allows decreasing the computation costs. The velocity of the indenter in experimental nanoindentation test is constant and very small. According to the experimental procedure in [9], the value of the indenter constant velocity does not have an effect on behaviour of specimen's material and is equal to 1 nm s^{-1}.
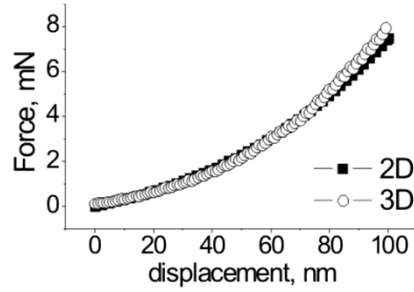

Fig. 5. Force versus depth results for 2D FEM axisymmetric and 3D FEM models

3.1. Sensitivity to shape of indenter, friction and parameters of material model

The design of conditions of an effective nanoindentation test and an adequate choice of the parameters of FEM model, are preceded by the sensitivity analysis introduced in [12]. The suggested approach allows estimation of influence of the individual process parameter on value of the analyzed one. The considered parameter is the total load (force) of the nanoindentation test; therefore, the sensitivity with respect to the process parameters is determined. The sensitivity coefficient φ to the parameter numbered as j at point $\mathbf{p}^*$ is defined:

$$\varphi_{p_j}\Big|_{\mathbf{p}^*} := \frac{p_j^*}{F_{av}(\mathbf{p}^*)} \frac{\partial F_{av}}{\partial p_j}\Big|_{\mathbf{p}^*} \approx \frac{p_j^*}{F_{av}(\mathbf{p}^*)} \frac{F_{av}(\mathbf{p}^* + \Delta p_j \mathbf{e_j}) - F_{av}(\mathbf{p}^*)}{\Delta p_j}, \tag{3}$$

where:

$\mathbf{p}^* = \left(R^*, \alpha^*, \mu^*, E^*, K^*, n^*\right)$ – considered point in the space of parameters,

$\mathbf{e_j}$ – vector of the canonical basis,

Δp_j – variation of the parameter p_j,

F_{av} – average value of the total load, calculated as follows:

$$F_{av} = \frac{1}{t} \int_0^t F(\tau) d\tau, \tag{4}$$

where:

$F(\tau)$ – the load at time τ,

t – total time of the process.

The sensitivities of total load of the nanoindentation test with respect to the parameters (R, α) of shape of indenter, friction coefficient (μ) and parameters of specimen's material (E, K, n) are analyzed. Two different specimens are investigated: an elastic monocoating specimen – 400 nm thick and a specimen composed of 7 hard nanocoatings.

For the first, monocoating specimen, twelve pyramid indenters with four radii equal 100, 110, 150 and 160 nm, as well as three vertex angles: 65.3, 67.5 and 70.32°, all with round tip are examined. The Coulomb friction law is assumed with the following values of friction coefficient: $\mu = 0.1$, 0.15, 0.2 and 0.25. The Poisson's ratio $v = 0.177$ and four elastic moduli: $E = 20$, 22, 28 and 30 GPa are used in the material model defined by Equation:

$$\sigma = E\varepsilon, \tag{5}$$

where:

σ – work-hardening stress,

ε – strain,

E – Young's modulus.

196 FEM simulations are performed. The obtained results of the sensitivity analysis presented in Figure 6 indicate that the nanoindentation test is the most sensitive to the parameters of shape of indenter, especially to the indenter angle. The friction does not require special consideration, because very low values of sensitivity coefficients are observed and, therefore, it can be omitted in future analysis.

The second examined specimen has the following 7 hard nanocoatings: coating 1 (elastic, 400 nm thick) is repeated four times and coating 2 (elastic-plastic, 40 nm thick) is repeated three times. The coating 1 is treated as an elastic material defined by Equation (5) and Poisson coefficient $v = 0.177$. The elastic-plastic material of the coating 2 is described by the Poisson coefficient $v = 0.225$ and the following relationship:

$$\sigma = K\varepsilon^n, \tag{6}$$

where:

σ – work-hardening stress,

ε – strain,

K – hardening coefficient,

n – hardening exponent.
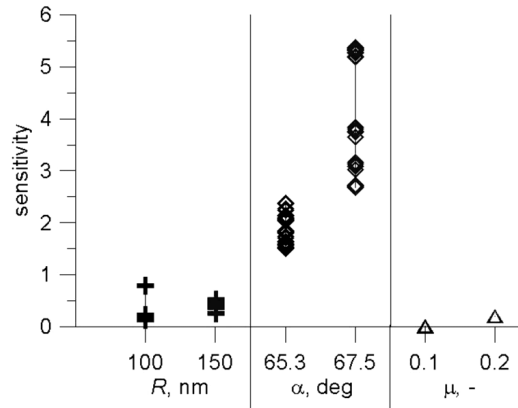
Fig. 6. Sensitivity of the load with respect to the parameters of shape of indenter:
R, α and friction coefficient μ for monocoating specimen

The parameters of material model of coating 1 are selected according to the range of values measured in the nanoindentation test performed in the present work. The considered values of the Young's modulus in the material model (5) of the coating 1 are: $E = 300$, 310, 500, and 510 GPa. The parameters of material model of coating 2 have very wide range of values, which is noted in [13–18]. The selected values of parameters in material model (6) of the coating 2 are: $K = 350$, 360, 450 and 460 MPa, while $n = 0.1$, 0.15, 0.3 and 0.35. Diamond, Berkovich indenter (radius $R = 150$ nm and pyramid angle $\alpha = 70.32°$) penetrates into specimen. The friction coefficient μ is assumed 0. Finally, 64 FEM simulations are generated.
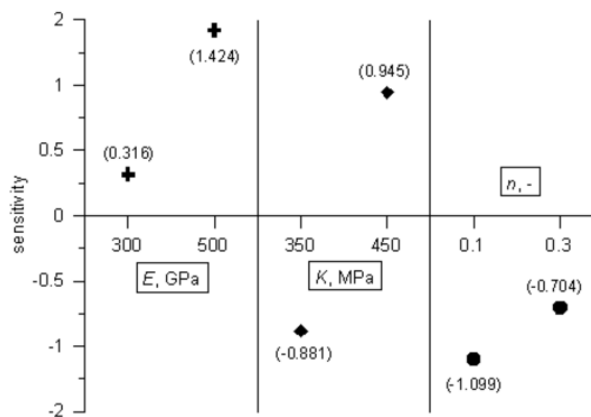

Fig. 7. Sensitivity of the load with respect to the material model parameters E, K and n
for the specimen of 7 hard nanocoatings

The calculated results of sensitivity analysis for the second specimen are plotted in Figure 7. They represent, that for chosen material models (5) and (6), the load is the most sensitive to the parameters E and n, as well as to the parameter K. It is found that each parameter of the material models (5) and (6) is influential and has to be introduced in the FEM models of nanoindentation test.

3.2. The developed FEM model of nanoindentation test

The purpose of study described in the previous subsection is evaluation of influence of the specified parameters of deformation process and parameters of material model on the total load (force), as well as choice of the optimal conditions and input settings in the FEM model of nanoindentation test for system of coatings. The estimated parameters of deformation process and material model used in the final FEM model of nanoindentation test are:

I – the angle of indenter $\alpha = 70.32°$ and tip radius $R = 150$ nm,

II – the velocity of indenter $v = 1$ nm s^{-1} and final displacement $d = 100$ nm,

III – the parameters K, n, E in used material models (5) and (6), which are specified in the last section of the previous subsection and presented in Figure 7,

IV – the specimen has seven coatings with material models described by equations (5) and (6), respectively for elastic coating 1 and elastic-plastic coating 2,

V – the frictionless conditions between indenter and specimen ($\mu = 0$).

The developed, used in further computations FEM mesh has 9000 nodes, 18 000 elements and is presented in Figure 8 as the non-deformed mesh before loading, and in Figure 9 as the deformed mesh after loading.
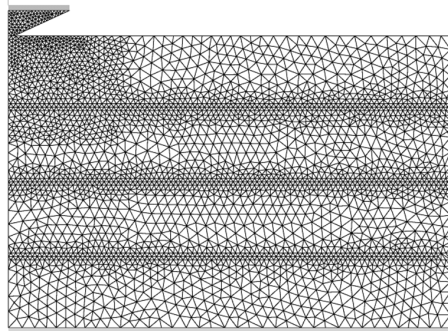

Fig. 8. The final FEM model of the nanoindentation test before loading

The described FEM model is developed in the FORGE 2 code. The results of FEM simulation are plotted in Figure 10 (distribution of equivalent strain) and Figure 11 (distribution of pressure). It shown, that the maximum of strain is located in the coating 2 and the maximum pressure is observed under the indenter.
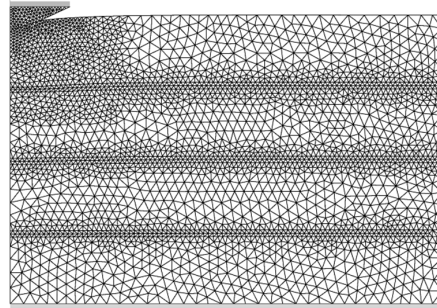
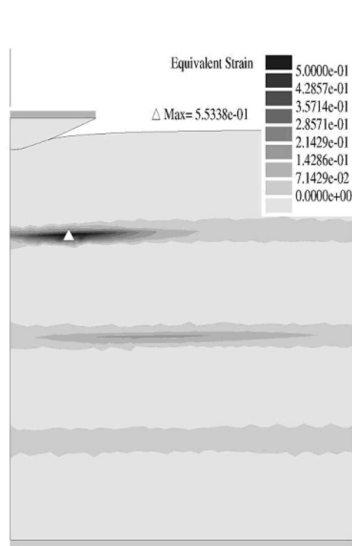Fig. 9. The final FEM model of the nanoindentation test after loading

Fig. 10. Distributions of the equivalent strain
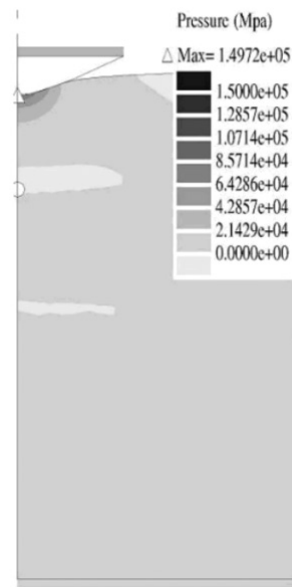in specimen of system of 7 nanocoatings

Fig. 11. Distributions of the pressure in specimen
of system of 7 nanocoatings

4. Inverse analysis

Generally, the main goal of the inverse analysis is evaluation of the real parameters of the model for the tested material. The purpose of the present work is evaluation of these parameters on the basis of the nanoindentation test for system of nanocoatings. The known and described widely in [1] analytical methods used in experimental nanoindentation test lead to evaluation of mechanical properties (Martens hardness and Young's modulus) and they produce desired results, but only for monolayer specimen. It is not possible to extrapolate these solutions to the system of nanocoatings.

The aim of the Authors' previous work [4] was to reach the conformity between the classical inverse analysis and the tension test for the steel, because the last experiment is impossible to be realized in laboratory practice for nanocoatings and gives much more consistent results than the nanoindentation test. The good capability of suggested inverse approach to predict the parameters for material model of C-Mn steel was observed and, therefore the developed classical inverse approach is used in the present paper to identification parameters of material model for the system of nanocoatings using the nanoindentation test results.

The objective of this research is to evaluate the properties of the inner coatings of the system. The inverse method is described in [19] and suggested by the Authors to solve this problem. The Martens hardness calculated for the system of coatings is the main output from the nanoindentation test, which is indirectly used in the goal function of the classical inverse analysis. Since the classical inverse analysis of system of coatings is quite time-consuming procedure, the modified inverse method is proposed. The load data (force) measured for the system of coatings is the main output from the nanoindentation test, which is indirectly used in the goal function of standard inverse analysis. The inverse approach is coupled with the artificial neural network (ANN). The ANN allows significant reduction of the computational costs.

4.1. Classical inverse approach and results

The identification of parameters for material model is done using the classical inverse approach. The objective of the inverse analysis presented in Figure 12 is to find, using the optimization procedure, the parameters of material model, which give the best matching between results of the FEM simulation and the experiment. The discrepancy between these values is defined by the goal function, which has to be minimized.
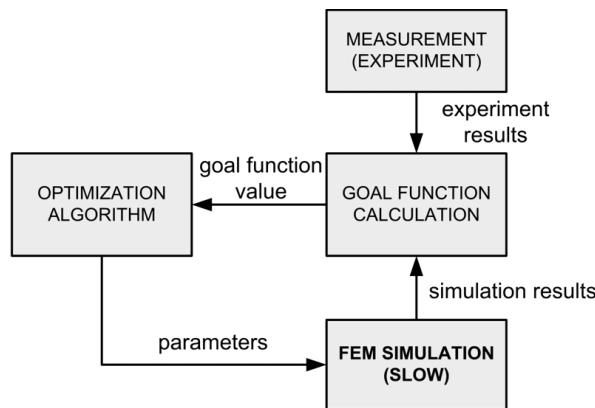

Fig. 12. The flow chart of the classical inverse approach

Unfortunately, in the case considered in the present subsection, the evaluation of goal function requires numerous time-consuming FEM simulations. In the analysed problem one simulation of nanoindentation test, in conditions introduced previously in the present work, is computed at least about four hours and the standard inverse analysis for one experiment lasts a few days.

The inverse algorithm is using the simplex optimization method, which is introduced in [3] and implemented by the Authors of present project into own code connected with commercial FEM program (Forge) in [4].

Elastic material model described by Equation (5) is set for directly deformed coating 1 and its properties are obtained from the experiment used in the present paper ($E = 368$ GPa and $\nu = 0.177$). Optimization variables E, K and n for the material model of coating 2 defined by Equation (6) are determined by searching for the minimum of the goal function defined for the Martens hardness of the coating 1.

The specified goal function is the mean square error between Martens hardness calculated experimentally and predicted in the simulation of nanoindentation test:

$$\Phi = \sqrt{\frac{1}{N} \sum_{i=1}^{N} \left(HM_{\mathrm{SIM}}^{i} - HM_{\mathrm{EXP}}^{i} \right)^2}, \tag{7}$$

where:

HM_{EXP} – experimental Martens hardness,

HM_{SIM} – simulated Martens hardness,

N – number of sampling points in experiment.

Minimum of function (7) is searched with respect to the parameters of the elastic-plastic material model for coating 2. This coating has no contact with the indenter, and its parameters of material model are reached in numerical test using optimization procedures. Stop criterion is achieved, if the predicted value of Martens hardness for the coating 1 is close enough to the experimental one. Hardness is determined from the calculated force/depth data using Equation (1). Proposed numerical procedure for the nanoindentation test is shown schematically in Figure 13.

Finally, the parameters of material model for coating 2 giving minimum of the goal function (7) are $K = 50$ MPa, $n = 0.1$, $E = 25$ GPa, computed Martens hardness of coating 1 $HM_{\mathrm{SIM}} = 31$ GPa and final goal function $\Phi = 310$ MPa.

This determined material model is used in the following simulations and Martens hardness of system of coatings calculated from Equation (2) is equal 26 GPa and the experimental value of specimen hardness is 23 GPa.

The proposed standard inverse method allow to obtain more information about examined specimen, especially regarding material models of coatings located in the lower parts of the system.
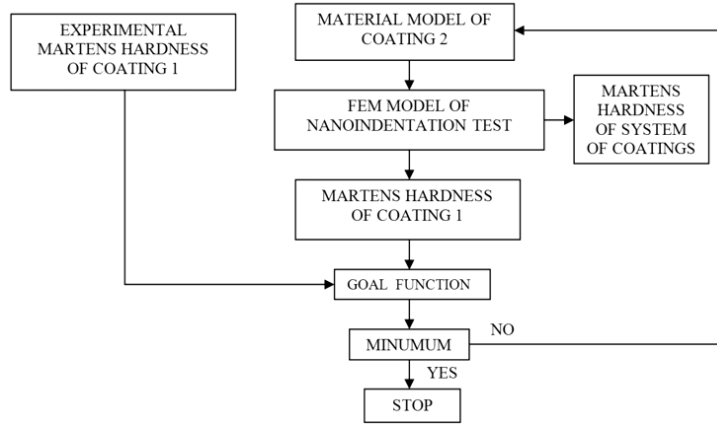
Fig. 13. The scheme of algorithm of inverse analysis for nanoindentation test
based on hardness for system of coatings

4.2. Metamodel and results

The inverse method can be speed up by using the fast metamodelling approach, instead of running thousands of FEM simulations. The idea of the metamodel approach can be briefly defined as modelling of the existing model. Usually, in the metamodelling procedure, various methods of approximation or artificial intelligence tools are used to modelling. The latter approach is applied in the present work.
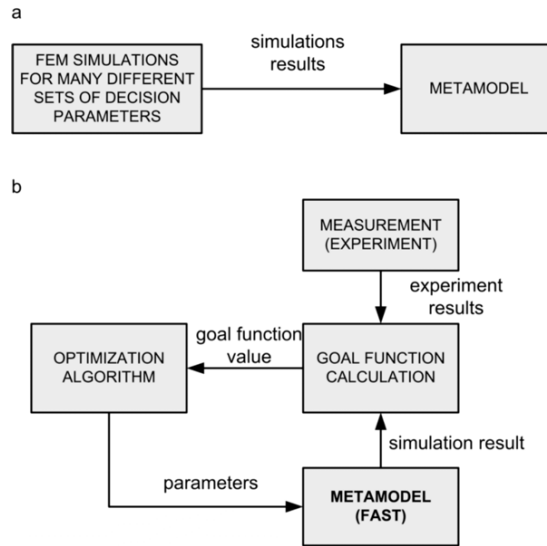

Fig. 14. The metamodel: a) creation and b) application in the inverse analysis

For the purpose of the inverse analysis of considered nanoindentation test the proposed metamodel is based on the artificial neural network models. Obviously, the ANN metamodel creation demands the number of time-consuming FEM simulations as the input data. But this is done once, and later on, the whole inverse procedure may be performed fast for many experiments. The idea of the metamodel creation and its application in the inverse analysis are shown in Figure 14.

As it was mentioned, the metamodel of the FEM output data of the nanoindentation test, obtained from the FORGE 2 simulations, is based on the artificial neural network approach. The MLP of the 4-2-1 architecture is used (logistic transfer functions in the first and second layers; linear activation function in the output layer – see Figure 15).
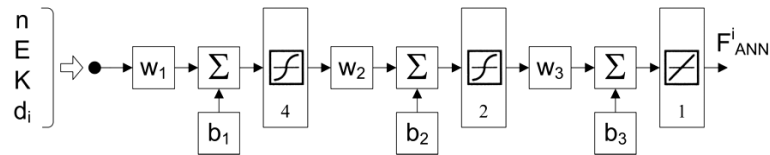

Fig. 15. The metamodel based on the ANN

The ANN input data are the parameters: n and K of material model (6) for coating 2, and E of material model (5) for coating 1, as well as the displacement d of indenter. The ANN output data corresponds to force F.

66 data sets for various n, K and E are used. The values of parameters n, K and E of material models for examined coatings are the same as those used for the sensitivity analysis performed for system of 7 coatings described in the subsection 3.1. Each set is composed of 8 values of force versus displacement data. 64 sets of data are training data, and two sets are used for ANN test. The network is trained using Levenberg-Marquardt algorithm in [5]. The network is tested for $n = 0.3$, $K = 350$ MPa, $E = 300$ GPa and the results are shown in Figure 16. Root mean square error for the two test sets is equal to 50 μN, which confirms good predictive capability of the network.
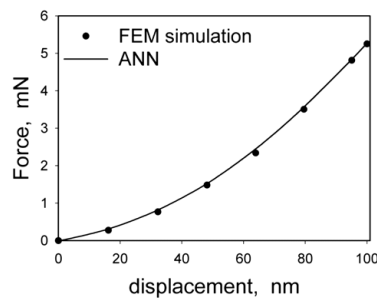

Fig. 16. Results of the artificial neural network test for work-hardening curves
of specimen composed of coatings

The trained network is used next as the metamodel in the inverse analysis. The analyzed goal function of the inverse problem is the root mean square error between experimental data and the output of the network:

$$\Phi = \sqrt{\frac{1}{N} \sum_{i=1}^{N} \left(F_{EXP}^{i} - F_{ANN}^{i} \right)^{2}}, \tag{8}$$

where:

F_{EXP} – simulated force vs. displacement,
F_{ANN} – predicted values of the force by ANN,
N – number of computing steps.

To find the minimum value of the goal function (8) the hybrid optimization procedure is applied. The genetic algorithm is used in the first phase to the localization of the minimum, while the Quasi-Newton algorithm is used in the final search. The whole algorithm of the inverse method with metamodel is shown in Figure 17.
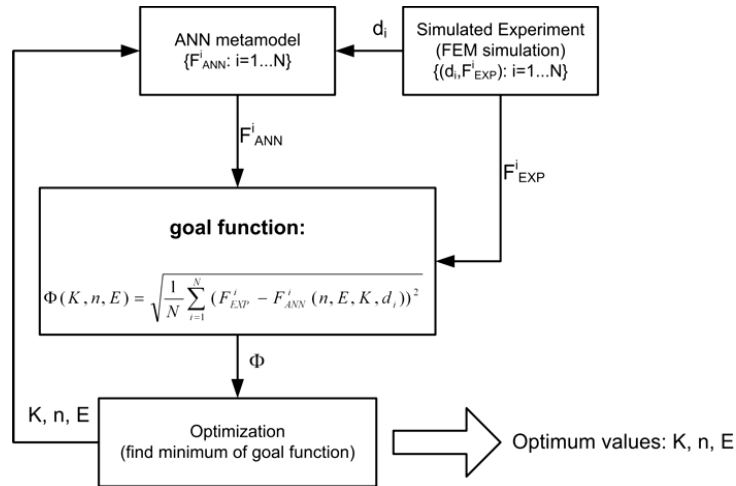

Fig. 17. Algorithm of the inverse analysis with metamodel

The experimental data is generated by FEM simulation for the set of parameters of material models: $n = 0.325$, $K = 455$ MPa and $E = 505$ GPa. The results for examined case are presented in Figure 18. Evaluated minimum of the goal function (8) is found at $n = 0.25$, $K = 457$ MPa and $E = 510$ GPa for analysed case. The goal function value is $\Phi = 80$ μN.

It is shown in Figure 18 that the experimental (simulated) points match very well the found solution. Unfortunately, the problem is irreversible. It means that for one set of force versus displacement can be found many different solutions. This statement is also confirmed by the second plot, which is shown in Figure 19.
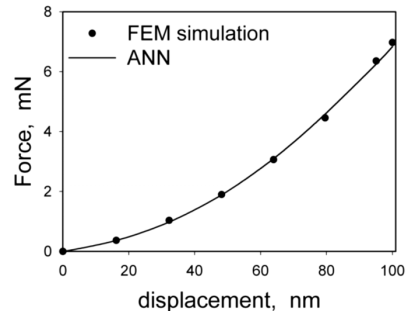
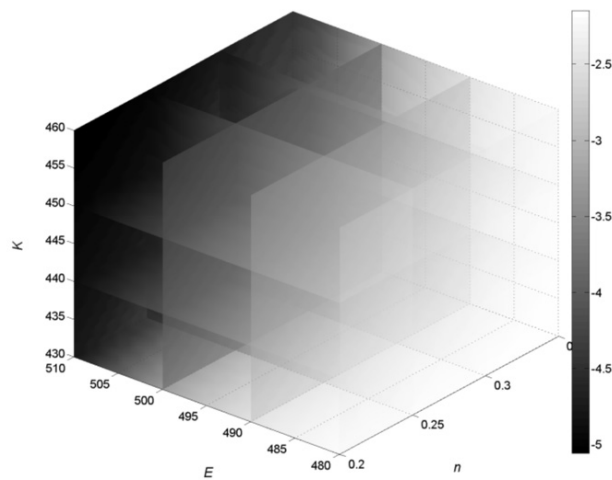Fig. 18. Results of the inverse analysis for the analysed case

Fig. 19. Plot of the logarithm of the goal function for the experimental data set

This plot presents logarithm of goal function (8) for the examined case. The chosen goal function for simulated experimental data set takes minimal values in some area located around experimental parameters. The minimum of goal function is shallow and therefore, the optimization result depends on the starting point. The ambiguity problem will be greater for the real experimental data (not simulated), because scatter in experimental results is usually observed. Thus, the future form of used material model (6) should be modified to other formula, for example to bilinear elastic-plastic material model.

5. Discussion and prospects

The development of FEM model of nanoindentation test for the system of coatings on the basis of experimental data is not sufficient enough, therefore is prepared an additional study, which is dedicated to calculation the sensitivity coefficients of the

model with respect to the crucial parameters of the examined deformation process. The achieved values of sensitivities related to parameters of shape of indenter and material models of coatings are big and none of them can be omitted in the model. The calculated sensitivity coefficient for the friction is very small and the friction is assumed 0 in the model, what corresponds to the experimental conditions of the test.

For the sensitivity approach the values of analysed parameters are considered in the range noticed in literature.

The elaborated FEM model of nanoindentation test for the system of coatings with mesh density enabling the achievement of correct solution is used to identification of parameters of coating 2 with the help of classical inverse analysis, for which the goal function is defined by Martens hardness. The program for standard inverse method with the implemented simplex algorithm was previously verified by the Authors in [4] for the monolayer specimen of steel in micro-indentation test. In that case the goal function was based on force and the results of analysis were additionally compared with the tension test data. Because the parameters of material model for steel determined on the basis of the classical inverse analysis and micro-indentation test data are compared to the tension test data mentioned in literature, the presented approach is used for the system of coatings. The searched parameters of material model of coating 2 are $K = 50$ MPa, $n = 0.1$, $E = 25$ GPa and the reached goal function is very small $\Phi = 310$ MPa. The identified small value of Young's modulus of coating 2 is difficult to be verified, because the tension test and the nanoindention test are not performed for such thin coating and are not presented in literature.

The application of standard inverse method needs the repeated calls of FEM program and it is very time-consuming procedure, therefore the approach based on the metamodel is proposed by the Authors. This solution requires performance of many simulations, which results are used for training the ANN, but next the fast identification of parameters of material model can be done using the experimental data. Both the training process of ANN and the quite complex procedure of identification of parameters with the help of metamodel lead to very small errors, which confirm the proper working of ANN and the possibilities of enriched inverse method (metamodel) to correct identification of the parameters for material models of coatings. The parameters of material models of coatings 1 and 2 are searched with the help of metamodel. The ranges of examined parameters for the material models are not compared with the results reached in the classical inverse analysis, because in the metamodel is used the data obtained in simulations, which are performed for the values of parameters observed in literature.

The purpose of the present project is development of the new numerical tool to identification of parameters of material models for system of coatings, which is capable to reach the results in a short time. The identification of parameters with the help of metamodel on the basis of real experimental results requires performance of many experiments and creation the data base, and then the identification of parameters for the added experimental results. The possibilities of elaborated tool offer mentioned

procedures, but it is not the purpose of present work and is planned to be done in future. It should be noticed that execution of the preprocessing stage of experimental data for the metamodel is considered to be a challenge for the Authors. The experimental results have big errors, which are described in [9].

6. Conclusions

The presented research and achieved results lead to the following conclusions:

• The developed classical inverse procedure based on the simplex optimization technique is capable to determine properly parameters in system of nanocoatings, for which the computing cost is big and the accuracy of experimental results is small.

• Presented metamodelling approach is useful in optimization problems when the evaluation of the goal function is time-consuming. The proposed algorithm allows radical decrease of the number of time-consuming FEM calculations. Despite of the initial computational efforts connected with the ANN training, the final use of the network as the metamodel in the evaluation of parameters of material model lasts only a few seconds. So, the reached time-profit is very high.

• The quality of results is very good. Trained ANN gives good compatibility with the test set.

• There is a certain disadvantage of presented approach – a weak ambiguity, because similar output curves can be obtained for different combination of chosen input parameters of material model. This observation is proved by the plot of the used goal function (8), which is shown in Figure 19. The goal function takes minimal values in some area located around chosen experimental parameters. The minimum of goal function is shallow and vast. Therefore, the analysed problem is irreversible. The disadvantage of such approach appears, because it is impossible to find out precisely, which combination of parameters in material model is the best solution of the inverse problem. Therefore, the future Authors' research will be focused on solving the uniqueness problem by modification of the form for material model, by adding more parameters.

• The ANN based metamodel can be used together with another optimization procedure, for example the one defined by heuristic algorithms.

• The key aspects of all the prospects and conclusions are important from Authors' point of view, because the examined system of nanocoatings is supposed to be used for demanding biomedical application. These coatings are planned to be deposited on polyurethane by PLD (Pulsed Laser Deposition) technique and to be used for artificial heart prosthesis as the constructional materials. Numerical model of such artificial organ needs the exact parameters of material model for all its material layers.

References

[1] Oliver C., Pharr G.M.: *An improved technique for determining hardness and elastic modulus using load and displacement sensing indentation experiment*, J. Mater. Res., Vol. 7, 1992, pp. 1564–1583.

[2] Kopernik M., Pietrzyk M.: *2D numerical simulation of elasto – plastic deformation of thin hard coating systems in deep nanoindentation test with sharp indenter*, Arch. Metall. Mater, Vol. 52, 2007, pp. 299–310.

[3] Nelder J.A., Mead R.A.: *A simplex method for function minimization*, Comput. J., Vol. 7, 1965, pp. 308–313.

[4] Kopernik M., Spychalski M., Kurzydłowski K.J., Pietrzyk M.: *Numerical identification of material model for C-Mn steel using micro-indentation test*, Mater. Sci. Technol., Vol. 24, No. 3, 2008, pp. 369–375.

[5] Koker R., Altincock N., Demir A.: *Neural network based prediction of mechanical properties of particulate reinforced metal matrix composites using various training algorithms*, Materials and Design, Vol. 28, 2007, pp. 616–627.

[6] Beake B.D., Smith J.F., Gray A., Fox-Rabinovich G.S., Veldhuis S.C., Endrino J.L.: *Investigating the correlation between nano-impact fracture resistance and hardness/modulus ratio from nanoindentation at 25–500 °C and the fracture resistance and lifetime of cutting tools with $Ti_{1-x}Al_xN$ (x = 0.5 and 0.67) PVD coatings in milling operations*, Surface and Coatings, Vol. 201, 2007, pp. 4585–4593.

[7] Beake B.D., Ranganathan N.: *An investigation of the nanoindentation and nano/micro-tribological behaviour of monolayer, bilayer and trilayer coatings on cemented carbide*, Mat. Sci. Eng., Vol. 23, 2006, pp. 46–51.

[8] Lackner J.M.: *Industrially – scaled hybrid Pulsed Laser Deposition at room temperature*, Orekop, Kraków, 2005.

[9] Fisher-Cripps A.: *Nanoindentation*, Springer-Verlag, New York, 2002.

[10] Albrecht H.-J., Hannach T., Häse A., Juritza A., Müller K., Müller W.H.: *Nanoindentation: a suitable tool to determine local mechanical properties in microelectronic packages and materials*, Arch. Appl. Mech., Vol. 74, 2005, pp. 728–738.

[11] Chollacoop N., Dao M., Suresh S.: *Depth-sensing instrumented indentation with dual sharp indenters*, Acta Mater., Vol. 51, 2003, pp. 3713–3729.

[12] Kopernik M., Szeliga D.: *Modelling of nanomaterials – sensitivity analysis to determine the nanoindentation test parameters*, Computer Methods in Materials Science, Vol. 7, No. 2, 2007, pp. 255–261.

[13] Cai X., Bangert H.: *Finite-element analysis of the interface influence on hardness measurements films*, Surf. Coat. Technol., Vol. 81, 1996, pp. 240–255.

[14] Franco A.R., Pintaúde G., Sinatora A., Pinedo C.E., Tschiptschin A.P.: *The use of a Vickers indenter in depth sensing indentation for measuring elastic modulus and Vickers hardness*, Materials Research, Vol. 7, 2004, pp. 483–491.

[15] Wang H.F., Bangert H.: *Three-dimensional finite element simulation of Vickers indentation on coated systems*, Mat. Sci. Eng., Vol. 163, 1993, pp. 43–50.

[16] Bouzakis K.D., Anastopoulos J., Asimakopoulos A., Michailidis N., Erkens G.: *Wear development of cemented carbide inserts coated with mono and multilayer PVD films, considering their strength properties, adhesion and the cutting loads*, Surf. Coat. Technol., Vol. 201, 2006, pp. 4395–4400.

[17] Jindal P.C., Santhanam A.T., Schleinkofer U., Shuster A.F.: *Performance of PVD TiN, TiCN, and TiAlN coated, cemented carbide tools in turning*, Int. J. Refract. Met. Hard Mater., Vol. 17, 1999, pp. 163–170.
[18] Su Y.L., Yao S.H., Wei C.S., Wu C.T.: *Tension and fatigue behaviour of a PVD TiN-coated material*, Thin Solid Films, Vol. 315, 1998, pp. 153–158.
[19] Szeliga D., Pietrzyk M.: *Testing of the inverse software for identification of rheological models of materials subjected to plastic deformation*, Archives of Civil and Mechanical Engineering, Vol. 7, No. 1, 2007, pp. 35–52.

**Zastosowanie klasycznej analizy odwrotnej i metamodelu
do identyfikacji własności nanomateriałów**

System powłok, które są napylane za pomocą fizycznego osadzania z fazy gazowej, zaplanowano zastosować w sztucznej protezie serca. Znajomość modeli materiału omawianych powłok jest niezbędna do projektowania numerycznego tego produktu i kluczowa dla przeprowadzenia dokładnych symulacji. Celem niniejszej pracy jest identyfikacja parametrów modeli materiałów nanopowłok opierając się na wynikach z próby wciskania wgłębnika i stosując dwie metody numeryczne: klasyczną analizę odwrotną i metamodel zbudowany z użyciem sztucznych sieci neuronowych.

Klasyczna analiza odwrotna została poprzedzona opracowaniem modelu elementów skończonych próby wciskania wgłębnika dla układu nanopowłok. Parametry modelu materiału każdej z powłok zostały określone. W drugim podejściu, aby obniżyć koszt obliczeniowy, zaproponowano wprowadzenie metamodelu. Tworzenie metamodelu polega na wprowadzeniu do rozwiązania sztucznych sieci neuronowych. Osiągnięte wyniki potwierdzają użyteczność zaprezentowanego rozwiązania do identyfikacji własności materiałów dla układu nanopowłok.

The influence of drawing speed on
fatigue strength TRIP steel wires

M. SULIGA, Z. MUSKALSKI, S. WIEWIÓROWSKA

Częstochowa University of Technology, Institute of Modelling and Automation of Plastic Working Processing, Armii Krajowej 19, 42-200 Częstochowa, Poland

The paper assesses the effect of drawing speed on the fatigue strength and roughness of the surface of TRIP steel wires. The drawing process was accomplished on a testing machine and on a block drawing machine, while applying three drawing speeds: 0.02, 0.75 and 1.6 m/s. The performed tests showed a positive effect of drawing speed on the fatigue strength of wires. It was found that the better fatigue strength of wires drawn at the speed of 1.6 m/s compared to wires drawn at the speeds of 0.02 and 0.75 m/s was associated with a better surface condition of these wires.

Keywords: *TRIP steel wires, fatigue strength, roughness*

1. Introduction

TRIP steels belong to the group of new steel grades that are characterized by very high strength and, at the same time, high plasticity properties. The advantageous plasticity properties of these steels are achieved as the result of martensite transformation induced by plastic deformation [1–3]. This phenomenon is referred to as the TRIP (Transformation-Induced Plasticity) effect [4].

TRIP steels have so far found application in the automotive industry for the production of car body elements. A number of publications dealing with the rolling and heat treatment of TRIP steel plates can be found in literature. However, there are few works on the subject of the processes of drawing wires of multiphase TRIP steels [5–8].

The analysis of the relevant literature shows that, with the same chemical composition, wires with the TRIP structure are distinguished by higher mechanical properties and fatigue strength compared to wires with e.g. a ferritic-pearlitic structure [9–10]. The much better fatigue strength, being an important factor defining the service values of wire products, may determine the areas of application of TRIP steel wires as a substitute for medium-carbon steels, for example in production of joint components like screws or rivets.

As the drawing speed is ranked among the basic parameters of the drawing process, the effect of this parameter on the fatigue strength and roughness of TRIP steel wires has been determined in the present work.

2. Research methodology

2.1. Material and drawing technology

The material for the tests was 6.3 mm diameter wire rod of low-carbon steel after TRIP-type heat treatment. Chemical composition of the steel is given in Table 1.

Table 1. Chemical composition of the TRIP steel

C	Mn	Si	P	S	Cu	Ni	Cr	Mo	Sn	Al	N
0.09	1.57	0.90	0.01	0.008	0.02	0.01	0.003	0.007	0.006	0.001	0.003

Two-stage heat treatment enabling a TRIP-type structure to be obtained in the wire rod was carried out under laboratory conditions in resistance heating furnaces at the Czestochowa University of Technology. The volumetric fraction of particular phases of the multiphase structure, as shown in Table 2, was determined using the program MET-ILO. The accuracy of the method of microstructural constituents' determination in Table 2 oscillated in range ±0.2 %.

Table 2. Volumetric fraction of phases [5]

Fraction of phases			
Ferrite %	Bainite, %	Retained austenite +~Martensite[1], %	Retained austenite[2], %
74.6	16.8	8.6	7.8

[1] Etched with the LePera reagent,
[2] Etched with Nital + sodium pyrosulfite.

After completion of heat treatment and metallographic examination confirming that the desired structure had been achieved, the TRIP steel wires were drawn in 11 draws from the diameter of 6.3 mm to the diameter of 1.9 mm using classical drawing dies of an angle of $2\alpha = 12°$. The process of wire drawing was conducted on the tensile test machine and drawing bench. Last of them has a 1.6 m/s speed limit of drawing. Table 3 summarizes single drafts (G_p) and total drafts (G_c). Table 4 provides the basic parameters of the drawing process, where: V_c is drawing speed, $G_{pśr}$ is medium single draft.

Table 3. A summary of single drafts and an total draft used for wire drawn from ∅ 6.3 mm to ∅ 1.9 mm according to Variants A, B, and C

Draft numbers	0	1	2	3	4	5	6	7	8	9	10	11
∅ wire, mm	6.3	5.6	5.0	4.5	4.0	3.6	3.23	2.93	2.53	2.3	2.1	1.9
G_p, %	–	21.0	20.3	19.0	21.0	19.0	19.5	17.7	25.4	17.4	16.6	18.1
G_c, %	–	21.0	37.0	49.0	59.7	67.4	73.7	78.4	83.9	86.7	88.9	90.9

Table 4. Parameters of the drawing process

Variant	Method of drawing	V_c, m/s	Number of draft	$G_{pśr}$, %	G_c, %
A	ZWICK/Z100	0.02	11	19.5	90.9
B	Drawing bench	0.75	11	19.5	90.9
C	Drawing bench	1.6	11	19.5	90.9

2.2. Fatigue strength tests

Fatigue strength tests on wires were carried out on a testing machine built in the Institute for the Modelling and Automation of Plastic Working Processes at the Czestochowa University of Technology, modelled after the design of the PUL DRABI SCHENCK fatigue testing machine. A diagram of the machine is shown in Figure 1.
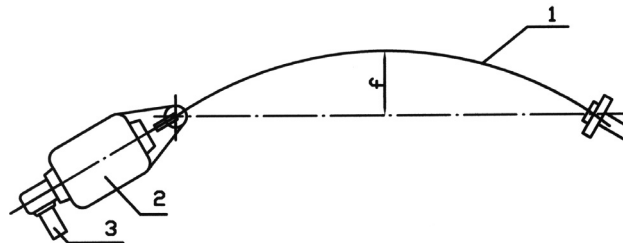

Fig. 1. Diagram of the testing machine used for testing the fatigue strength of wires in the wire under investigation; 1 – wire, 2 – motor, 3 – revolution counter, f – deflection

The fatigue tests of wires were conducted under the conditions of rotary bending; the maximum bending stress in the outer wire layers was calculated from Formula 1, while substituting in the formula the actual value of Young's modulus, as determined from the tensile tests performed on the testing machine. In these tests, the number of cycles (N) completed until the break of the wire was determined.

$$\sigma_{max} = \pm \frac{6 \cdot f \cdot d \cdot E}{l^2}, \ [MPa] \tag{1}$$

where:
   f – deflection,
   d – wire diameter,
   E – Young's modulus,
   l – specimen length.

The temporary (time-limited) fatigue strength, Z_g, allowing the determination of the Wöhler curves, was determined for wires' diameters of $\varnothing$ 2.93 mm, $\varnothing$ 2.53 mm and $\varnothing$ 1.9 mm, for drawing variants A, B, and C, while applying three different levels of bending stress, σ_{max}.

2.3. Examination of the surface geometrical structure of drawn wires

The examination of changes in the surface condition of the surface of TRIP steel wires was carried out on a Form Talysurf Series profilometer. To illustrate the effect of drawing speed on the roughness of surface, the following parameters were selected for analysis:

– profile height parameters: R_p, R_v, R_t, R_{vm},
– profile deviation parameter: R_a,
– horizontal profile parameter: S,
– Newman's ratio: S/R_{vm}.

The investigation reported in work [2] shows that there is also a relationship between the horizontal parameters and the profile height. It has been demonstrated that the temporary fatigue strength, Z_g, of wires is directly proportional to the converse of the surface condition ratio, as defined by Newman:

$$\alpha_k = 0.139\left(\frac{a}{c}\right)^2 - 0.314\left(\frac{a}{c}\right) + 1.12, \ [\text{-}] \tag{2}$$

where:

α_k – surface geometrical ratio,
a – surface defect depth (proportional to R_{vm}),
c – surface defect width (proportional to S), or:

$$Z_g \cong \frac{c}{a} \cong \frac{S}{R_{vm}}. \ [\text{-}] \tag{3}$$

In accordance with the surface condition ratio, the decline of the fatigue strength of wire is inversely proportionally influenced by the defect depth, R_{vm}, while the improvement of fatigue strength is achieved for wires with a higher value of the defect width parameter, S.

The measurement of the roughness of TRIP steel wires was made for 3 wire diameters: $\varnothing$ 4.0 mm, $\varnothing$ 2.53 mm, and $\varnothing$ 1.9 mm. Five samples from each variant were taken for examination. To remove the lubricant, the wires were washed in a NaOH solution, and then rinsed with acetone and left for drying.

In the examination of the surface condition of the wire surface, the measurement section length, L, was equal to 5 elementary sections, each of 0.8 mm ($L = 4.0$ mm).

3. Research results

Table 5 shows the results of the fatigue strength tests of TRIP wires. For a better analysis of the effect of drawing speed on the fatigue strength of wires, the percentage

differences in the number of fatigue cycles (N) between Variant A (taken as 100%) and Variant C were also calculated for different levels of bending stress.

Table 5. Average values of the number of fatigue cycles (N) completed until the break of wires drawn according to Variants A and B for different levels of bending stress, and the percentage differences between Variant A (taken as 100%) and Variant C

$\varnothing$ wire, mm	σ_{max}, MPa	Variants	Number of fatigue cycles, N	Difference, %
2.93	780.2	A7	12045	+11.2
		B7	12920	
		C7	13400	
	616.8	A7	19087	+37.2
		B7	20910	
		C7	26180	
	538.4	A7	45210	+27.6
		B7	48440	
		C7	57706	
2.53	801.4	A8	12874	+18.6
		B8	13027	
		C8	15269	
	661.7	A8	24468	+53.0
		B8	26150	
		C8	37446	
	617.8	A8	48065	+31.0
		B8	54804	
		C8	62980	
1.9	850.1	A11	13621	+48.6
		B11	14280	
		C11	20240	
	801.9	A11	17451	+46.3
		B11	18608	
		C11	25532	
	744.7	A11	44124	+42.1
		B11	49150	
		C11	62700	

Based on the results given in Table 5, fatigue strength graphs (Wöhler curves for the fatigue strength, Z_g) were plotted for wires from Variants A and B, by approximating the obtained results with a logarithmic function (Figures 2–4).

The investigation results presented above show that the drawing speed has a great effect on the fatigue strength of TRIP steel wires. The significant differences in fatigue strength between Variants A, B and C are confirmed by the large percentage differences (Table 4). With increasing drawing speed, the fatigue strength of wires increases. For example, increasing the drawing speed from 0.02 m/s (Variant A11) to 1.6 m/s (Variant C11), at a bending stress of 744.7 MPa, resulted in an increase in the fatigue strength of the wires from Variant C11 against the wires from Variant A11 by 42.1%.

It can be noticed that the differences in fatigue strength between Variants A, B and C increase with increasing total draft (Table 4).
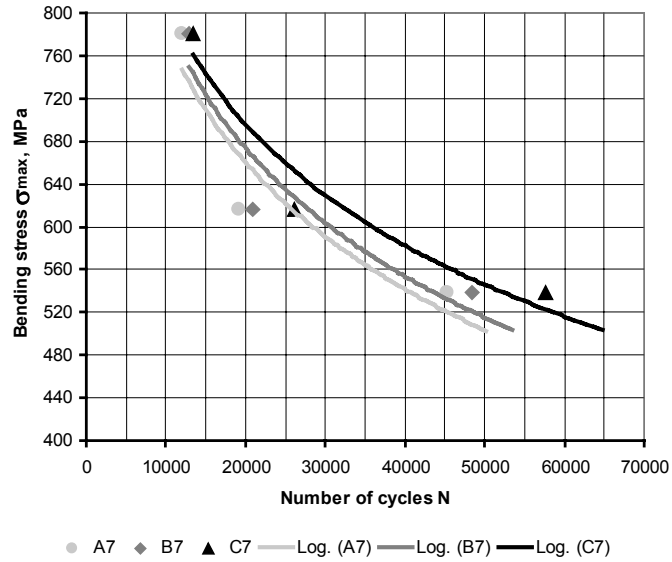

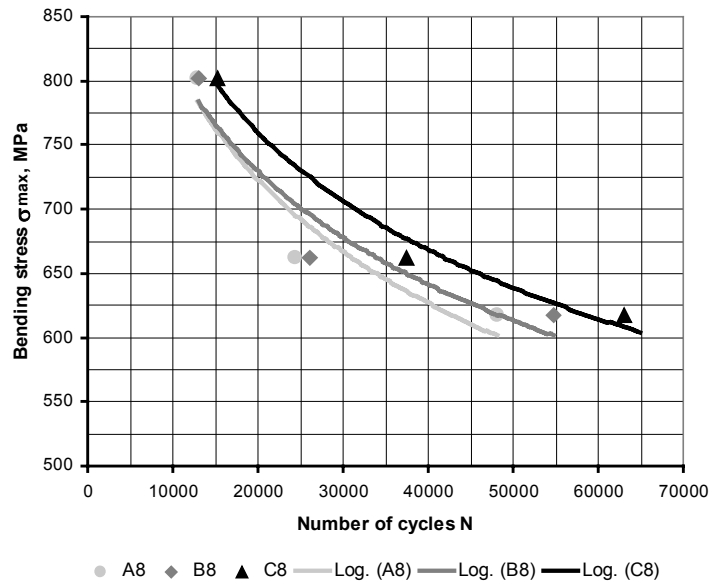Fig. 2. Diagrams of the temporary fatigue strength of ⌀ 2.93 mm wires drawn according to Variants A–C

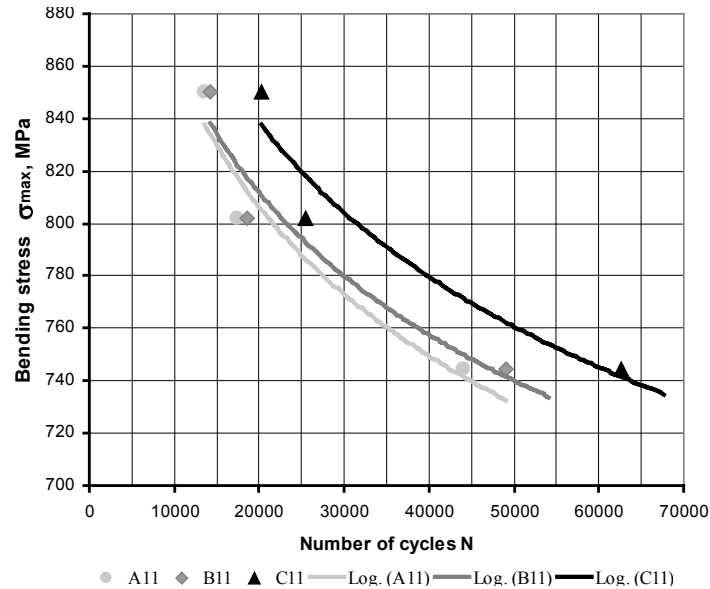Fig. 3. Diagrams of the temporary fatigue strength of ⌀ 2.53 mm wires drawn according to Variants A–C

Fig. 4. Diagrams of the temporary fatigue strength of $\varnothing$ 1.9 mm
wires drawn according to Variants A–C

The surface condition of drawn wire surface is ranked among the factors that substantially influence the achievable level of fatigue strength. The values of the geometrical parameters of the surfaces of wires drawn according to Variant A ($V_c = 0.02$ m/s), B ($V_c = 0.75$ m/s) and C ($V_c = 1.6$ m/s) are represented in Figures 5–8.

Based on the data presented in Figure 5 it can be stated that the drawing speed influences the profile height parameters. The wires from Variant A ($V_c = 0.02$ m/s), as compared to the wires from Variant B ($V_c = 0.75$ m/s), have definitely lower surface roughness, as evidenced by the small values of R_v, R_p and R_t. The differences between Variant A and Variant B range from 39.7% to 157.3%. Presumably, the lubrication conditions for Variant A were much worse than in the other variants due to the very low drawing speed, at which the lubricant is not "drawn in" to the drawing die in a sufficient amount, whereby the drawing die could better "smooth" the wire surface. Increasing the drawing speed from 0.75 m/s (Variant B) to 1.6 m/s (Variant C) resulted in a decrease in surface roughness. The wires from Variant C, as compared to the wires from Variant B, have the parameter R_t lower by 39.5 to 48.1%. It was found that, within the speed range of 0.02–1.6 m/s, with increasing drawing speed the mean defect depth, R_{vm}, decreased, which might have a favourable effect of improving the fatigue strength of wires.

With respect to the profile deviation parameter, R_a, the values of this parameter for the surfaces of wires drawn according to Variant A ($V_c = 0.02$ m/s) are from a dozen or so to several tens percent lower than for the surfaces of wires drawn according to

Variant B, which is confirmed by the results shown in Figure 6. This is indicative of the fact that the irregularity profile area is much smaller for the latter variant.
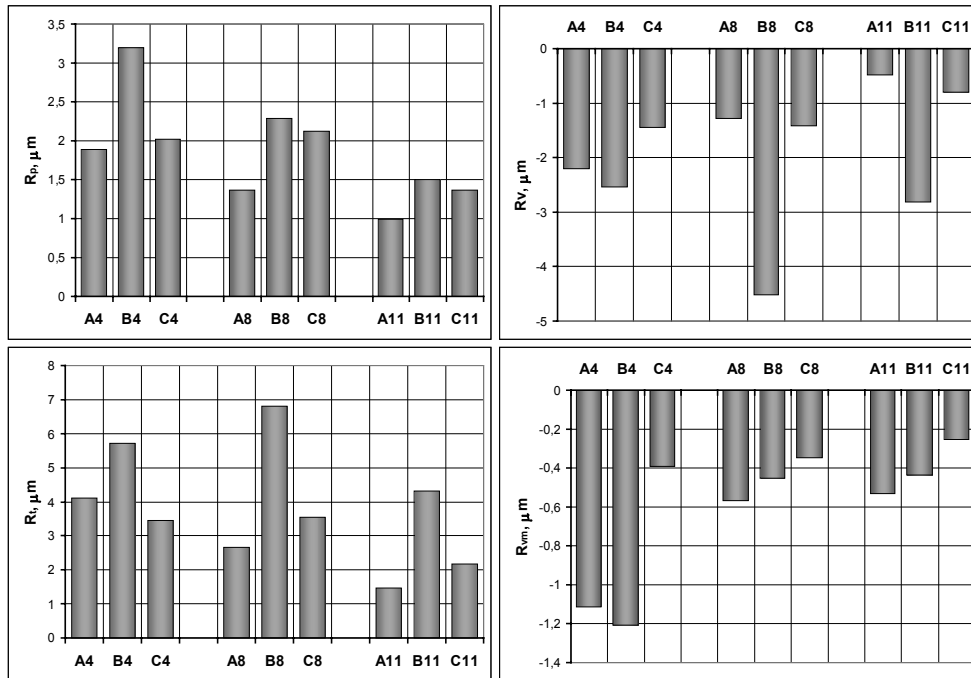

Fig. 5. Values of the profile height parameters of the surface condition of wires' diameters of ∅ 4.0 mm, ∅ 2.53 mm, and ∅ 1.9 mm drawn according to Variants A, B and C

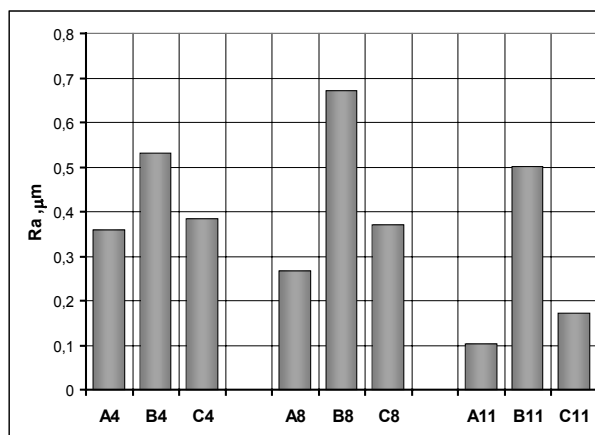Fig. 6. Values of the profile deviation parameter, R_a, of the surface condition of wires' diameters of ∅ 4.0 mm, ∅ 2.53 mm, and ∅ 1.9 mm drawn according to Variants A, B and C
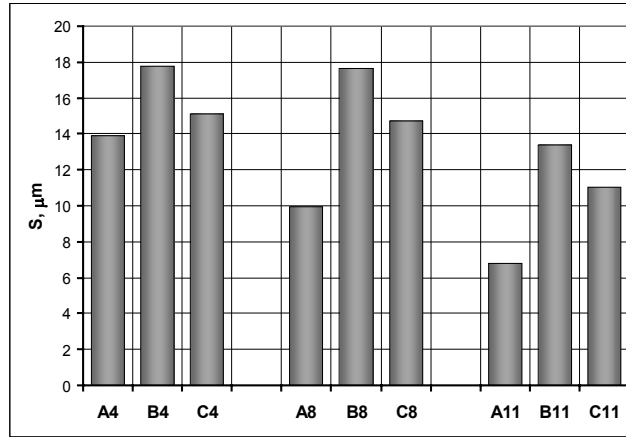
Fig. 7. Values of the horizontal profile parameter, *S*, of the surface condition of wires' diameters of ∅ 4.0 mm, ∅ 2.53 mm, and ∅ 1.9 mm drawn according to Variants A, B and C
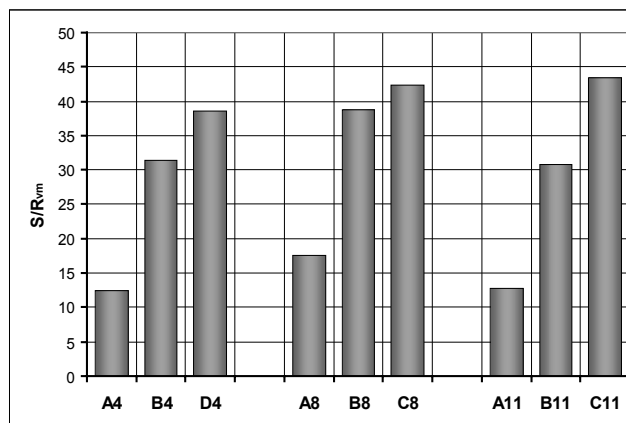
Fig. 8. Values of Newman's ratio, S/R_{vm}, of the surface condition of wires' diameters of ∅ 4.0 mm, ∅ 2.53 mm, and ∅ 1.9 mm drawn according to Variants A, B and C

Based on Figure 7 it is found that, within the horizontal parameters, the wires from Variant A have the smallest mean spacing between adjacent profile protrusions, compared to the wires from Variants B and C. Thus, these wires are more prone to the "notch phenomenon".

From the data shown in Figure 8 it can be found that with the increase of drawing speed Newman's ratio increases. The differences between Variants A and C range from 142 to 240%. This indicates a favourable effect of drawing speed increase on the parameters that have the influence on the fatigue strength of wires.

4. Conclusions

1. Increase in drawing speed positively influences the fatigue strength of TRIP steel wires. Wires drawn at the speed of 1.6 m/s exhibit fatigue strength higher on average by 25–45% that that of the wires drawn at $V_c = 0.02$ m/s, depending on the level of bending stress.

2. The tests carried out have shown that the effect of drawing speed on the fatigue strength of wires is the greater the higher their total draft is.

3. With increasing drawing speed Newman's ratio increases, which indicates a favourable influence of drawing speed on the fatigue strength. Increasing the drawing speed from 0.02 m/s to 1.6 m/s resulted in a significant increase in Newman's ratio, which amounted to over 200% for final $\varnothing$ 1.9 mm wires.

References

[1] Grosman F.: *Nowoczesne blachy stalowe na elementy karoserii w świetle projektu ULSAB-AVC*, Metallurgist-News Metallurgist, Jule, 2003, pp. 302–307.

[2] Grosman F.: *Nowoczesne stale na blachy tłoczne dla motoryzacji*, Obróbka Plastyczna Metali, No. 4, 2002, pp. 5–15.

[3] Dziedzic M., Turczyn S.: *Taśmy ze stali wielofazowych dla przemysłu samochodowego*, Metallurgist-News Metallurgist, April, 2003, pp. 153–158.

[4] Jacąues P.J., Petein A., Harlet P.: *Improvement of mechanical properties through concurrent deformation and transformation: new steels for the 21st century*, TRIP – International Conference on TRIP Aided High Strength Ferrous Alloys, GRIPS-Proceeding, Ghent, 2002, pp. 281–286.

[5] Suliga M.: *The theoretical-experimental analyses of the drawing process TRIP steel wires* (PhD thesis), Czestochowa University of Technology, Częstochowa, 2007.

[6] Suliga M., Muskalski Z.: *The influence of single draft on mechanical-technological properties of TRIP steel wires*, Metallurgist-News Metallurgist, 2007, pp. 353–356.

[7] Suliga M., Muskalski Z.: *The evaluation of structure and TRIP effect during wire drawing process of 0.09C–1.57Mn–0.9Si steel*, Ginger and non-ferrous metals, Vol. 11, 2007, pp. 850–854.

[8] Suliga M., Muskalski Z., Wiewiórowska S.: *The influence of drawing speed on properties of TRIP steel wires*, 16th International Scientific Conference on Achievements in Mechanical and Materials Engineering AMME 2008, 22–25 June, Gliwice–Ryn, 2008.

[9] Suliga M., Muskalski Z., Wiewiórowska S.: *The influence of TRIP type heat treatment on mechanical properties of 0.09C–1.5Mn–0.9Si steel wires*, Information technologies in plastic working, Kramatorsk, Ukraine, 21–24 April, 2008.

[10] Suliga M., Muskalski Z.: *The comparison of the mechanical properties and fatigue strength of the low carbon TRIP steel wires with D45 steel wires*, Metallurgist-News Metallurgist, January, 2008, pp. 6–10.

Wpływ prędkości ciągnienia na wytrzymałość zmęczeniową drutów ze stali TRIP

W pracy oceniono wpływ prędkości ciągnienia na wytrzymałość zmęczeniową i strukturę geometryczną powierzchni drutów ze stali TRIP. Proces ciągnienia zrealizowano na maszynie

wytrzymałościowej oraz na ciągarce jednobębnowej stosując trzy prędkości ciągnienia: 0,02, 0,75 i 1,6 m/s. Przeprowadzone badania wykazały pozytywny wpływ prędkości ciągnienia na wytrzymałość zmęczeniową drutów. Stwierdzono, że lepsza wytrzymałość zmęczeniowa drutów ciągnionych z prędkością 1,6 m/s, w stosunku do drutów ciągnionych z prędkościami 0,02 i 0,75 m/s, związana jest z ich lepszą strukturą geometryczną powierzchni.

Price 15 zł
(0% VAT)